High Resolution Modeling of Regional Phases

Thesis by

Xi Song

In Partial Fulfillment of the Requirements

for the Degree of

Doctor of Philosophy

Caltech

Pasadena, California

1997

(Submitted May 29, 1997)

Acknowledgements

I was fortunate to have the opportunity to study in the Seismological Laboratory. My stay here has been a very pleasant learning experience. I would like to thank the faculty, staff and students for fostering such a creative and friendly environment.

I am grateful to my advisor, Prof. Don Helmberger, for his patience, encouragement and support throughout my work. He has cared about me and my future as much as my work. Working with him is very enjoyable and this thesis would not have been possible without his help. I owe Prof. Thomas Ahrens my gratitude for his guidance in the first phase of my graduate study. I enjoyed the classes of Prof. Hiroo Kanamori, Prof. Don Anderson, Prof. Robert Clayton, Prof. Thomas Heaton, and Prof. David Stevenson. I thank Prof. Yuk Yung for his hospitality and advise, from which I greatly benefited. Special thanks go to the secretaries, especially Ann Freeman, Evelina Cui, Sue Yamada, and Donna Sackett, for their help and their effort to make the lab and the division run smoothly.

Just before I sat down and started writing this thesis, I enjoyed the Pahoehoe trip led by Prof. Leon Silver and Prof. Jason Saleeby. I thank these two gentlemen and my fellow campers for making this trip a great learning opportunity and an enjoyable experience. My sincere appreciation goes to Pele the Lady and Prof. Bob Sharp for making this exciting trip possible and I wish them both well.

I was also fortunate to have met many good people here. Craig Scrivner, my mentor and friend, who has had the patience to review every research manuscript I have written, is always ready for questions of any kind. To him, I salute. Dr. Lianshe Zhao, Dr. Laura Jones, Dr. Hong Kie Thio, Dr. Bradley Woods, Dr. Shingo Watada, Dr. Dapeng Zhao, Dr. Xiaodong Song, Dr. Weishi Huang, and Dr. Chandan Saikia are pleasant to work with and fun to talk to. I enjoyed their intuition and enthusiasm for science and I thank them for their precious advice at various stages of my study. Blair Zajac has put a lot of effort to minimize the adverse factors

during a computer system transition. Dr. Wenbo Yang, Miriam Jackson, Kathleen Holland, George Chen, Xiaoming Ding, Timothy Melbourne, Jascha Polet, Lupei Zhu, Lianxing Wen, Igor Sidorin, and Cangli Liu all contributed to my understanding of Geophysics and made my life easier by sharing with me their expertise in different areas. Dr. Bradley Woods, Craig Scrivner, Dr. Shingo Watada, Jascha Polet, Leo Eisner, and Javier Favela have been good office mates and are helpful in various ways. I consider myself lucky to have been part of an enthusiastic research group and to have had the opportunity to interact with all these brilliant and friendly people.

I have also benefited a great deal from people outside Caltech. Mr. Chenghsien Liu and Mr. Liankai Song and their friends made my first trip to Caltech possible. I am grateful to Prof. Huajun Wang, my advisor for undergraduate study in University of Science and Technology of China, for his guiding me into Earth science and for the freedom he gave me. My uncle Xiankui has been always supportive of me during the course of my education. My high school teacher, Mr. Yingming Peng, deserves my special thanks for every good thing I have today.

Heartfelt thanks goes to my wife, Yao, for her love, encouragement, and support. I dedicate this thesis to my parents, who have been working unbelievably hard to allow me to obtain the best education possible.

Abstract

It has been a long-time goal of seismologists to decouple source phenomena from propagation effects. This thesis elaborates on our effort towards this goal.

We start by representing earthquakes as point-sources in space and using 1-D synthetics to resolve point-source parameters. Our trial-and-error approach to obtain 1-D crustal models is summarized in a set of sensitivity tests, where regional seismograms are decomposed into segments, *i.e.*, the P_{nl} segment, the SV waves, the Love wave and the Rayleigh wave, so that the impact of model parameters on each segment is the most direct. In these tests, broadband waveform data is studied in a forward modeling approach, with synthetics computed using the reflectivity method and the generalized ray theory. Applying these tests to paths sampling the Basin and Range province, we find that a simple two-layer crustal model is effective in explaining regional seismograms. Our sensitivity tests also serve to help understand, and interpret, the many results of a source estimation method we use to obtain point-source parameters. This method desensitizes the source mechanism result from the crustal model used to generate the 1-D synthetics, by allowing relative time shifts between the various segments. With this method, we obtain source mechanisms and seismic moments for a selection of Northridge aftershocks using broadband and long-period waveform data recorded by the TERRAscope array. The source duration of these earthquakes is measured by comparing the short-period to long-period energy ratio in the data to that in the synthetics. The seismic moment and source-duration are used to estimate the relative stress drop. The depth distribution of the relative stress drop indicates that the largest stress drops are in the depth range of 5-15 km for the 24 Northridge aftershocks in our study.

To obtain more detailed information about large earthquakes, such as fault dimension and rupture directivity, we develop a new method of using empirical Green's functions (eGf). As an example, the January 17, 1994 Northridge mainshock is stud-

ied with one of its aftershocks as an eGf. The source duration of the mainshock, as seen from the regional surface waves observed at various stations, is obtained by searching for the trapezoidal far-field source-time function for each station which, when convolved with the aftershock data, best simulates the mainshock data. Stations to the north see shorter source durations than those to the south. Modeling these with theoretical predictions of rupture on a square fault, we constrain the effective fault dimension to be 14 km with rupture along the direction of the average rake vector. A moment of $(1.4 \pm 0.9) \times 10^{26}$ dyne·cm with a stress drop of $\sim$120 bars is obtained for the mainshock from our eGf study.

When empirical Green's functions are not available due to a difference in the source mechanisms or in the source locations, theoretical modeling plays an important role. Our approach to develop high resolution Green's functions is to convert eGfs to pseudo Green's functions (pGf). This is done by modeling the eGfs with the generalized ray theory and consists of two major steps.

The first step is to shift individual ray responses to account for a difference in source location. This ray-shifting technique has its own use in fast generation of synthetic seismograms for finite sources. To study the directivity for a finite source, we discretize the fault region into a set of elements represented as point-sources. We then generate the generalized ray responses for the best-fitting point-source location, and derive for each separate ray the response for neighboring point-sources using power series expansions. The response for a finite fault is then a summation over rays and fault elements. If we sum over the elements first, we obtain an effective far-field source-time function for each ray, which is sensitive to the direction of rupture. These far-field source-time functions are convolved with the corresponding rays and the results summed to form the total response. A simple application of the above method is demonstrated with the tangential motions observed from the 1991 Sierra Madre earthquake. For this event, we constrain the fault dimension to be about 3 km with rupture towards the west, which is compatible with other more detailed studies.

The second step in the modeling of the eGfs and the development of pseudo Green's functions is to account for variations in model structure by perturbing individual gen-

eralized ray responses calculated from a 1-D model. The model is divided into blocks and velocities in the blocks are allowed to vary, which shifts the arrival time of the individual rays. The amplitudes of the rays are perturbed independently to accommodate local velocity variations in the structure. For eGfs that are moderate-sized earthquakes with known source mechanism and time history, the velocity variation in each block and the amplification factor for individual rays can be optimized using a simulated annealing algorithm. The usefulness of the pGfs is demonstrated with the 1991 Sierra Madre earthquakes as examples. The pGf technique is also useful in retrieving 2-D structure, which is essentially waveform tomography. This is demonstrated with a study of a Tibetan profile.

Contents

List of Figures

List of Tables

Chapter 1 Introduction

A seismogram is a complex recording that contains information about the earthquake source and the media through which the seismic energy propagates. In order to decouple these two types of information, seismic recording has advanced from isolated stations to arrays and from narrow-band instruments to broadband stations. As a result, seismic studies have progressed from simple travel time analysis to spectral and waveform modeling. Whether it is to resolve point source parameters, to investigate complex crustal structures, or to determine source characteristics, the ability to model regional phases with high resolution is important. This thesis presents a series of recently developed techniques for solving this problem.

Seismic source discrimination is one of the major concerns in today's seismic studies. Since most of the earth's surface is covered by sparse networks, many seismic discrimination techniques rely heavily on the use of regional records [*e.g. Helmberger and Woods*, 1996]. This in turn depends on our ability to model broadband regional records. Often the approach is to use simple crustal models to characterize the regional propagation effects and then develop discriminants that are transportable from region to region. Because of the portability requirement, it is important that simple crustal models are used instead of complex ones.

Many techniques exist to find crustal models to fit regional records. These often require non-linear inversion of travel times or long-period waveforms. The most frequently used technique, however, is probably the straight forward trial-and-error approach. In this approach, parameters in some starting model are adjusted and synthetics waveform computed and compared to data. The process is repeated until a model that provides a satisfactory waveform fit is found. Since these techniques use complete seismograms, the resulting model is almost always complicated, consisting of many layers of different velocities. Moreover, the comparison between data and synthetics can be easily dominated by surface waves since they are the largest features

on a seismogram. An alternative approach would be to fit the waveforms of different segments on a seismogram with a simple model and allow minimal relative time shifts among these segments. Such a simple model would be useful in characterizing regional propagation and the time shifts would be indicative of lateral variation in the crustal structure. In fact, many discrimination techniques utilize this approach on regional seismograms. For example, *Helmberger and Woods* [1996] use the energy level of different segments and the ratios between them as their major discriminants. Thus, it is important to establish the relationship between model parameters and seismogram segments, and to develop simple models that correctly predict the waveform features along particular paths in a region.

Such an approach using simple crustal model with relative time shifts allowed between different segments is also useful in determining point source parameters for earthquakes. Since different segments can shift in time relative to the rest of the seismogram, the source parameters so determined are less sensitive to the crustal model used to generate the synthetics. *Zhao and Helmberger* [1994] utilized this feature in their "cut and paste" method of source estimation. With this method, source mechanism, seismic moment, and source-time function can be estimated from relatively simple crustal models. For an aftershock sequence, these parameters allow further studies of the source region, such as the stress drop distribution and seismic energy propagation in the source region.

The body of this thesis consists of five chapters, each of which is self-contained, with its own abstract, introduction, method and application, and conclusion or discussion sections. These chapters are unified under a single theme of decoupling the source complexity from propagational effects. This general problem requires modeling regional phases to high resolution, but the approach to this goal always starts with simple 1-D models and point source parameters. Chapter 2 details our trial and error approach to 1-D synthetics. In this chapter, the effect of various model parameters on different segments of a regional seismogram is tested. These tests help the modeler adjust the relevant model parameters in a forward approach to find the best fitting 1-D model that matches the data in shape, allowing minimal time shifts among different

seismogram segments. These tests also help to understand, and to interpret the many results of the "cut and paste" source estimation method, which is detailed and used in later chapters. Besides this source estimation method, a few other techniques are reviewed and employed in Chapter 3 to study the source mechanism, seismic moment and relative stress drop of a selection of Northridge aftershocks. The source-time history of the aftershock sequence is studied by comparing the short- to long-period energy ratio between data and synthetics [*Zhao and Helmberger*, 1996]. Then, the relative stress-drop of these earthquakes is calculated from the seismic moment and source duration using the formula of *Cohn et al.* [1982]. The effects of the San Fernando basin on the propagation of the seismic energy along particular paths crossing the basin are discussed in this chapter.

When the best fitting 1-D model is found and the optimal point source parameters determined, more sophisticated Green's functions are required to resolve more details about the source process. Features such as the fault dimension and rupture direction of a large earthquake are important in post-earthquake damage estimates and in understanding the physics of earthquakes. Empirical Green's functions provide a handy tool for studying these features [*Hartzell*, 1978], and this method has been used extensively in recent years [*e.g. Dreger*, 1994]. With this technique, a small earthquake in the neighborhood of a large one is modeled with a point source and the seismograms recorded for this small event is used to account for the impulse response along the common path. Often a record of the small event is deconvolved in frequency domain from a record of the large earthquake along the same path. This method can produce rupture details for the large earthquake under investigation, but the results depend heavily on the quality of the empirical Green's functions. So, before solving for the details of the rupture process, it is important to identify the most important parameters that are resolvable from broadband records, given a set of empirical Green's functions. A forward approach of using empirical Green's functions is introduced in Chapter 4, where time-domain convolution is used instead of frequency-domain deconvolution. It is found that, for the Northridge mainshock, the fault dimension and rupture direction are the most important parameters that control

the fit between data and the simulations using empirical Green's functions from a nearby aftershock. The potential to provide a better fit to the data, and therefore to better resolve the source process, is limited by the quality of the empirical Green's functions, that is, the difference in source location and source mechanism between the main event and the aftershock used as the empirical Green's function. These two problems must be solved before we can use empirical Green's functions effectively to separate source complexity from propagation phenomena.

Our approach to produce highly accurate Green's functions, or pseudo Green's functions (pGf) as we call them, is to model empirical Green's functions to high resolution using the generalized ray theory. The modeling serves two purposes. One is to separate the effect of the source mechanism from the empirical Green's functions and to decompose the eGfs to Green's functions for the basic fault orientations. The other is to decompose the empirical Green's functions into individual ray responses, so that their arrival times can be adjusted individually. This allows for adjustment of source location. Chapter 5 elaborates on the ray-shifting technique that handles this adjustment. The ray-shifting technique has its own use in studying fault dimension and source directivity of large earthquakes, and, in Chapter 5, the 1991 Sierra Madre mainshock is studied with this method.

The detailed modeling process that converts an eGf to a pGf is presented in Chapter 6. This forward modeling process, characterized by a simulated annealing process, is capable of producing practical, high-resolution Green's functions that are transportable to neighboring events. In Chapter 6, the pGf method is applied to study a small event using pGfs derived from a neighboring moderate-sized event. The pGf technique is also useful in fine-tuning a 1-D model per path and generating 2-D tomographic models. This is also demonstrated in Chapter 6 for a Southern California path and for a Tibetan profile.

Chapter 2 Broadband modeling of regional seismograms; the Basin and Range crustal structure

2.1 Abstract

Three-component broadband displacement seismograms with paths sampling the Basin and Range Province are studied to constrain the crustal structure. To find an average model that fits the data in both absolute time and waveform, we generate broadband reflectivity synthetics and conduct sensitivity tests on different parts of a layered crustal model, where only a few layers are involved. Generalized rays are used to help identify the various phases. It proves useful to decompose a regional seismogram into segments so that the impact of model parameters on each segment is the most direct. Thus, for mid-crustal earthquakes, it is established that the top crustal layer controls the Rayleigh wave, the Airy phase, in shape over the range from 300 to 600 km, and the crustal layer just above the source depth controls its timing. The P_{nl} waves, the P_n and P_L portion, are controlled in broadband character by the mid-crust while the top layer contributes to its long period motion. These crustal parameters control the tangential motion similarly. The SV wave, the segment between the P_{nl} wave and the Rayleigh wave, is mostly controlled by the shear velocity of the lower crust. In judging the goodness of fit between the array observations and synthetic waveforms, we allow individual data segments to shift relative to the 1-D synthetics a few seconds to account for some lateral variation. The amount of time shift is found by the cross-correlation in displacement between the data segment and the synthetics. Applying these tests in a forward modeling approach, we find that a simple two-layer crustal model is effective in explaining this data set. In this model, the main crustal

layer has P and S velocities of 6.1 km/sec and 3.6 km/sec, similar to those found by *Langston and Helmberger* [1974]. A surface layer of thickness 2.5 to 3.5 km is required to fit the Rayleigh waves. The refined model can be used as a reference model for further studies in this region.

2.2 Introduction

Recent advances in high-dynamic range digital instrumentation are allowing dramatic improvement in our ability to estimate seismic characteristics from regional seismograms. This is demonstrated by the introduction of a number of new analytical tools used in estimating source parameters from such data. For example, it is possible to invert regional surface waves at periods greater than 50 sec for events with $M_s > 5$ throughout the western United States with one simple model [*Ritsema and Lay*, 1993]. For smaller events, the long period excitation becomes noisy and the body waves become more prominent. Methods that are more sensitive to body waves have been introduced by *Dreger and Helmberger* [1993] and *Zhao and Helmberger* [1994]. Many times one station is sufficient to estimate those parameters with a proper crustal model [*e.g. Dreger and Helmberger*, 1993].

The method used by *Zhao and Helmberger* [1994] involves a direct grid search over the source parameter space (strike, dip, rake), in which observed and synthetic broadband seismograms are decomposed into segments and the corresponding data and synthetic segments are compared. In their method, the P-wave windows and the S-wave windows are allowed to have relative time shift between them, which desensitizes the solution to the crustal model used in generating the synthetics. A demonstration of the usefulness of this approach in the estimation of the source mechanism of the April 29, 1993 Arizona event [*Zhao and Helmberger*, 1996] is displayed in Figure 2.1. The TERRAscope stations and the event location are shown in Figure 2.2, along with other events investigated in this study. The cross-correlation between data and synthetics requires that the synthetic P_{nl} waves be shifted ahead by an average less than 1 sec, the Rayleigh waves by about 5 sec and the Love waves by about 3 sec.

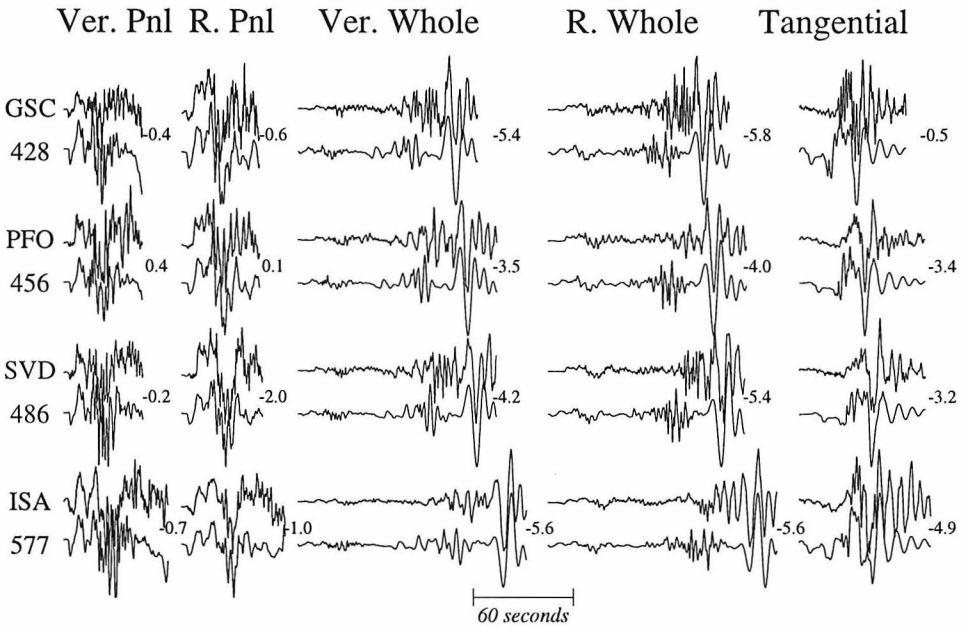

Figure 2.1: Comparison between the broadband displacement data (top traces) and the corresponding best-fitting synthetic waveforms (bottom traces) for the Arizona earthquake. Station names and the distance from the event are shown. The small numbers indicate, in seconds, the time shift of the synthetic waveforms relative to the data. A positive number indicates that the synthetic is early. After *Zhao and Helmberger* [1996].

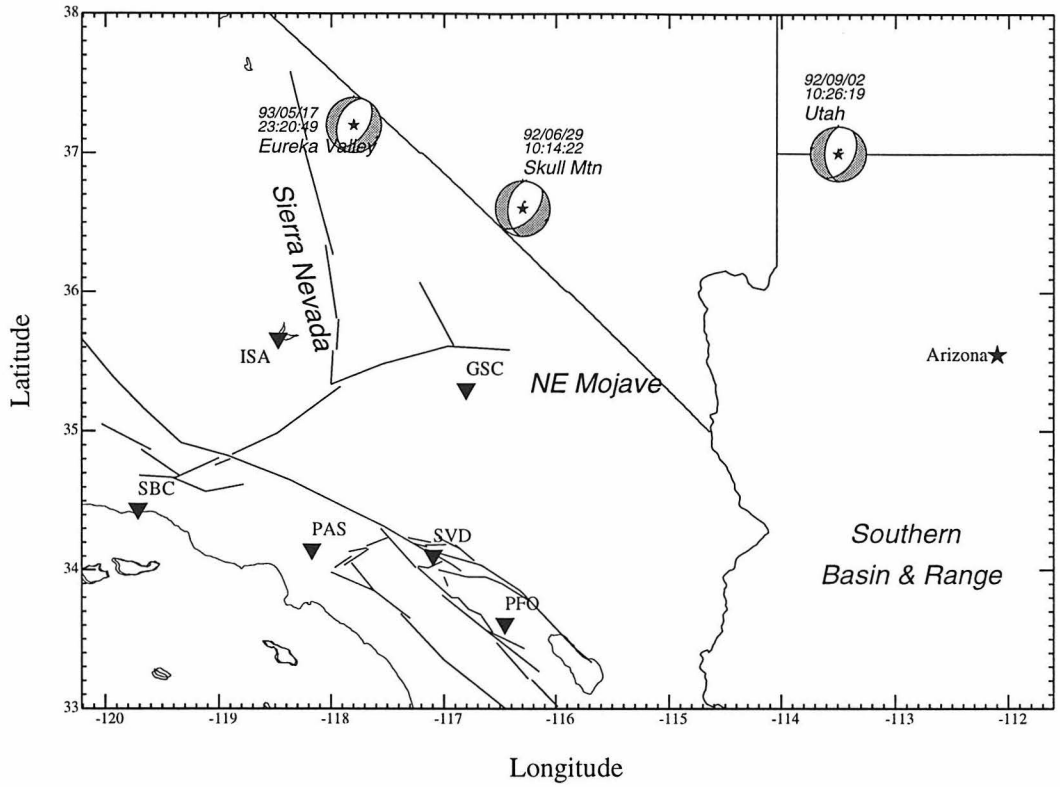

Figure 2.2: Map of the Southwestern United States showing the locations of the events (stars) and some TERRAscope stations (triangles) used in this study. The station Tucson (TUC, 110.78W, 32.31N) is out of the map. Origin time and source mechanism for the events used in this study are also shown.

In this sense, the model they used (Table 2.1, model *PB* [*Priestley and Brune*, 1978]) is edequate for the P_{nl} waves but is too slow to match the surface waves along these paths. Also, the separations between the synthetic *P*-wave train and the Rayleigh waves are larger than those observed. However, by applying the segmentation technique, they were able to use these synthetics effectively in their source estimation, as discussed by *Zhao and Helmberger* [1996].

While the above technique appears to be effective in source estimation, it would also be useful in establishing creditable crustal models. Present strategies in model determination typically use trial-and-error search procedures or perhaps waveform inversion techniques. The latter methods compare whole seismograms against synthetics in a least square sense and determine the best set of 1-D model parameters.

Since the surface waves are the strongest in a seismogram, they dominate the solution. However, the surface waves, especially their timing, are particularly influenced by lateral variation in the shallow crust, as demonstrated by *Stead* [1990]. Perhaps a useful alternative approach would be to search for a 1-D model that fits the segmented wave shapes and minimizes the absolute travel time shift between data and synthetics for individual segments. We will investigate such an approach in this chapter where we find that simple crustal models prove effective in modeling the Basin and Range crustal structure.

2.3 Model sensitivities

The usual situation facing waveform modelers is similar to that in the Arizona example discussed in the last section. That is, to determine the nature of the seismic source with inadequate crustal models. Thus, we would like to learn from the time shifts and the shape mismatch in Figure 2.1 how to infer a better model. For example, what model parameter is the most effective in moving the Rayleigh waves or in fixing the SV mismatch. To address such issues, we will conduct a set of sensitivity tests on some simple models. For these tests, a double couple source with strike 180^0, dip 50^0 and rake 250^0, which is typical for events studied in this chapter, is used. We use a seismic moment of 1.0×10^{27} dyne·cm and a far-field source-time function described by a triangle (0.5 sec, 0.5 sec). The source depth is 11 km, and the receiver is located at a distance of 460 km away from the source, with a source-receiver azimuth of 226^0. The waveform complexities in regional seismograms produced by shallow events can be very difficult to model [*e.g. Zhao and Helmberger*, 1996] and will be avoided in this study.

2.3.1 The making of a regional seismogram

One way to appreciate how a 1-D seismogram is constructed is to use the Generalized Ray Theory (GRT) [*Helmberger*, 1983] to compute synthetic waveforms for individual arrivals and observe the interplay between different rays. Another way is to compute

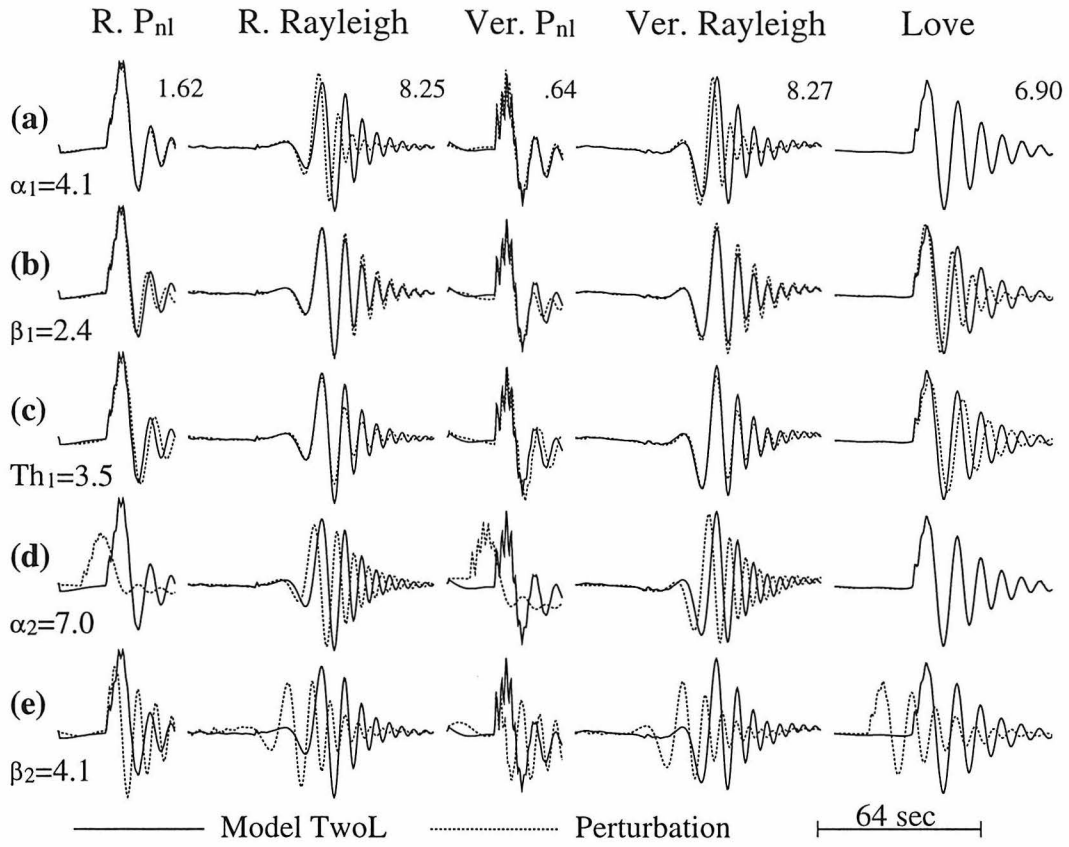

Figure 2.3: Comparison of synthetic displacement waveforms between model *TwoL* and a series of perturbed models. Only one parameter is perturbed in each test (*a–e*) with the perturbed parameter shown for the perturbed model. Each section of seismograms is scaled according to the solid trace with peak amplitude shown in cm.

complete synthetic seismograms, say with the reflectivity method, starting from models of one layer over a half space and introducing more complexity by adding deeper discontinuities. In the tests presented here, we use a modified Frequency-Wavenumber Algorithm [*Saikia*, 1994a] to compute complete seismograms and use generalized rays to analyze phase information.

For two-layer models (Model *TwoL*, Table 2.1), surface waves are very simple (Figure 2.3) , but body waves already show some complexity. Our GRT analysis reveals that the first 30 seconds of the body wave is mainly direct P, P to S converted at the interface, and multiples that bounce between the free surface and the layer interface. Among these, rays ending up with a P motion are high-frequency and tend

Model	V_p km/sec	V_s km/sec	ρ g/cm^3	Thickness km
TwoL	3.6	2.05	2.2	2.5
	6.1	3.57	2.8	
TriL	3.6	2.05	2.2	2.5
	6.1	3.57	2.8	22.5
	6.6	3.87	2.9	
PB	3.6	2.05	2.2	2.5
	6.1	3.57	2.8	22.5
	6.6	3.87	2.9	10.0
	7.85	4.53	3.3	
tbPB	3.6	2.05	2.2	2.5
	6.1	3.57	2.8	32.5
	7.85	4.53	3.3	
t58PB	3.6	2.05	2.2	2.5
	5.8	3.57	2.8	32.5
	7.85	4.53	3.3	
tn1PB	3.6	2.05	2.2	2.5
	6.1	3.57	2.8	32.5
	7.85	4.53	3.3	10.0
	7.70	4.53	3.3	10.0
	7.55	4.53	3.3	10.0
	7.4	4.53	3.3	

Table 2.1: Model parameters

to contribute mostly on the vertical component due to the large velocity contrast at the interface. Those ending up with an SV motion are usually stronger and have relatively longer duration and contribute more on the radial component. Thus, the vertical component of the broadband body waves for this simple model at regional distance shows more high-frequency content but weaker motion compared to the radial component.

The SV wave, or the segment between the P_{nl} wave and the surface wave on these seismograms, is barely seen and the body wave energy is dominated by the up-going P-waves. It is clear, in Figures 2.3a and 2.3b, that the change of the compressional wave velocity, V_p, of the top soft layer changes the shape, or the frequency content, of the Rayleigh waves in a very simple fashion such that the seismograms are compressed with the beginning portion somewhat fixed. The shear wave velocity, V_s, of the top layer controls the Love waves in a similar manner. It has relatively smaller effect on the Rayleigh waves than V_p. On the P_L part that is guided by the top layer, V_s of the top layer has stronger effect than V_p. The thickness of the top layer affects both the surface wave part and the body wave part (Figure 2.3c), and the Love waves are more sensitive to this shallow perturbation than the Rayleigh waves, which is what we would expect from the basic construction of these two types of waves. The trade-off between the velocity and the layer thickness can be seen by comparing Figure 2.3b with 2.3c.

In Figures 2.3d and 2.3e, the V_p and V_s of the half space are increased by 14% each. Although these perturbations are no more than those in Figures 2.3a and 2.3b, the seismograms change dramatically. In the surface wave part, unlike the top cases, change is more in terms of timing rather than in wave shape. If the surface waves of the seismograms were allowed to shift a little, they would fit quite well with their counterparts. Change in the P_{nl} wave part is more complicated and is both in timing and in shape. However, one can still see that V_p alone controls the earliest part of the body wave and V_s contributes to the later segment, P_L. This provides the basis that the V_p structure can be modeled with the earliest part of data without much information on the V_s structure.

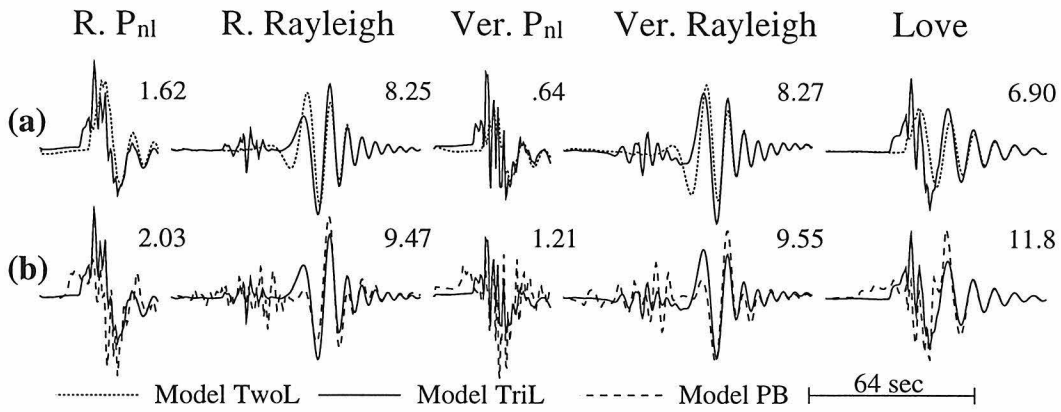

Figure 2.4: Comparison of synthetic displacement waveforms between models *TwoL*, *TriL* and *PB* (Table 2.1). Each pair of seismograms is plotted on the same scale. The peak amplitude (cm) of seismograms for model *TwoL* is shown in (*a*) and that for model *TriL* is shown in (*b*).

The effect of adding a deeper discontinuity to a simple model is shown in Figure 2.4. As discussed in detail in *Helmberger et al.* [1993] SV waves at this range are dominated by the down-going SV energy that is reflected back by the deeper crustal structure. This feature is clearly seen in these seismograms as the SV waves are much stronger compared to those in Figure 2.3. Head waves are produced by the lower interface, along with more high-frequency signals that complicate the P_{nl} portion of the seismograms. Although reflections and multiples from the deep interface overwhelm the up-going P energy, the long period feature of the P_{nl} wave does not change much. As for surface waves, the slow groups with shorter periods are not very sensitive to the appearance of this deeper discontinuity but the fast groups with longer periods change a lot. This is because that longer-period surface waves sample deeper. The introduction of still another deeper discontinuity (Figure 2.4*b*) change the seismograms in a similar manner. It again adds another head wave group to the seismograms and complicate them even more.

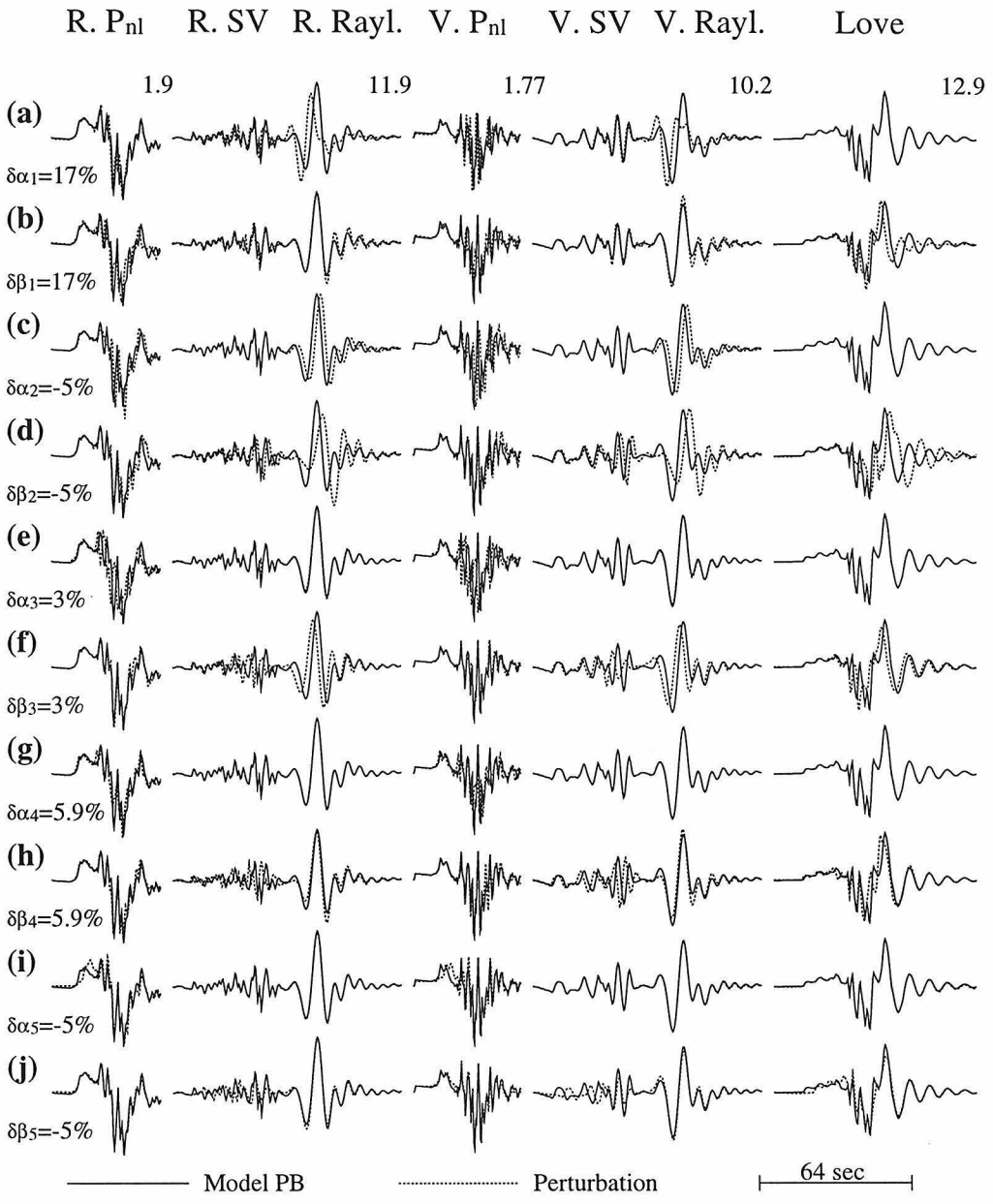

Figure 2.5: Comparison of synthetic displacement waveforms between model *PB* and a series of perturbed models. Only one parameter is perturbed in each test (*a–j*) with the perturbed parameter shown for the perturbed model. Each section of seismograms is scaled according to the solid trace with peak amplitude shown in cm.

2.3.2 Systematic perturbation to a crustal model

To build a more direct relationship between model parameters and the seismogram segments, we conduct, in this section, a systematic perturbation to a typical crustal model (model *PB*, Table 2.1). This model was derived by *Priestley and Brune* [1978] in their surface wave studies of the Basin and Range province and was proven effective in more recent waveform studies of this region [*e.g. Zhao and Helmberger*, 1996]. Since a small change in velocity of a thick layer produces a large change in travel time, we attempt to minimize this effect by conserving vertical travel time differentials. Thus we perturb the crustal velocities of this model in such a way that, for each layer, the product of the thickness and the percentage change of the velocity is the same, with the exception that changes to the mantle velocities are fixed at 5%. Seismograms computed from the original model and those from the perturbed models are compared in Figure 2.5. To quantify the comparison, we cut the radial and the vertical components into three segments: the P_{nl} wave, the SV wave, and the Rayleigh wave. The tangential component is compared as a whole and is referred to as the Love wave for simplicity. In comparison, each pair of seismogram segments is cross-correlated in order to determine the relative time shift between them. This shift, compared to the beginning time of the corresponding segment, is referred to as the time effect of the perturbed velocity on the same segment. After the two segments are shifted properly relative to each other, an error value, defined as an average of the L_1 and the L_2 norm [*Zhao and Helmberger*, 1994], is calculated. This is referred to as the shape effect of the perturbed velocity on the corresponding segment. Figure 2.6 summarizes the quantitative results of these comparisons.

While the results in Figure 2.6 are consistent with those qualitative ones we discussed before, there are a few details that are of interest. As seen in Figure 2.6, the P_{nl} wave contains information about most of the crust, but the overall timing of this phase group is mostly controlled by the middle part of the crust. The SV wave, on the other hand, is not sensitive to the crustal P velocity; its timing and shape are controlled by the shear velocity of the lower crust. While the surface layer has great

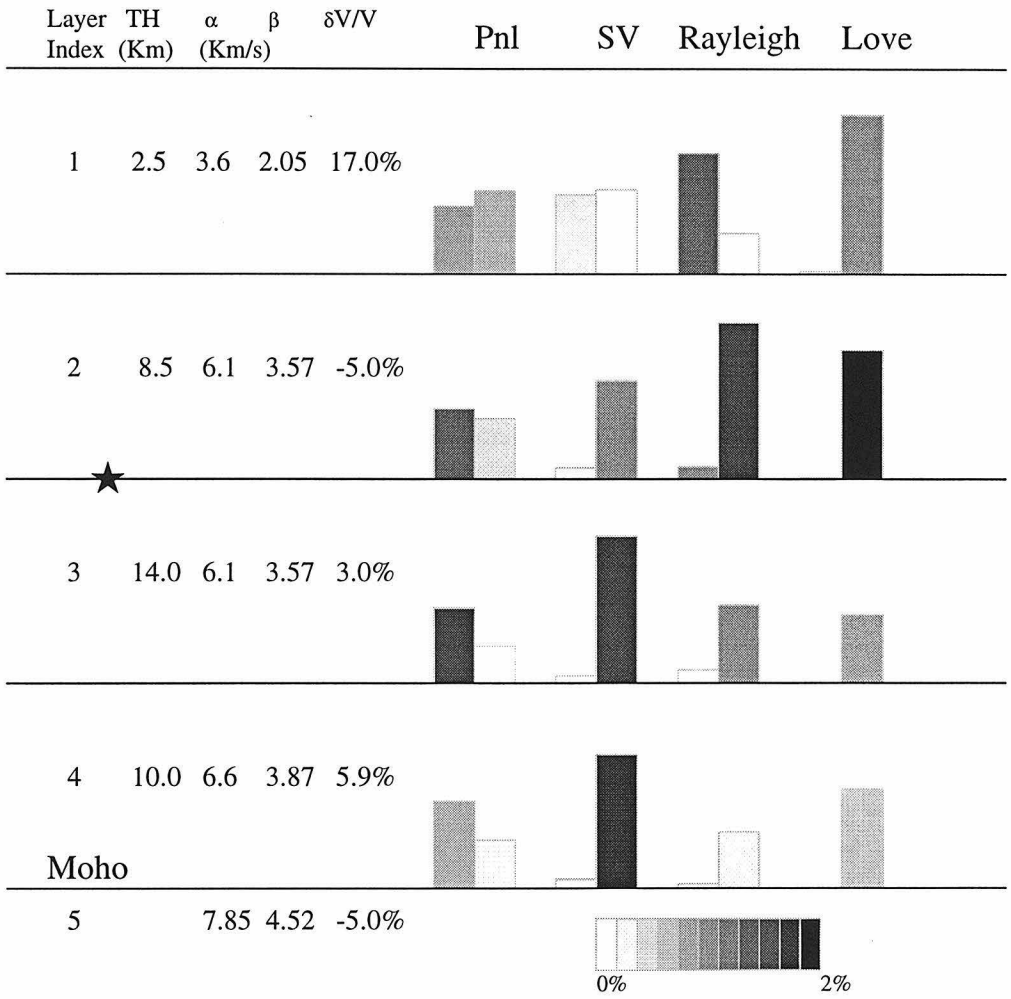

Figure 2.6: Summary of the effects of different parts of a layered model on a regional seismogram. The parameters of the original model and the amount of velocity perturbation are shown to the left. Each pair of boxes corresponds to the V_p and V_s of that layer, respectively. The height of the boxes represents the shape effect (see text) and the shade of the boxes represents the time shift in travel time percentage. In the Love wave column, the boxes corresponding to V_p have zero height. The star indicates the source location.

influence on all segments of a seismogram, it has the greatest impact on the surface waves. In contrast to the SV waves, surface waves are less sensitive to the structure below the source depth. Their shape is mostly controlled by the crust above the source depth and their timing is most sensitive to the shear velocities of these layers. Note, though, it is the P velocity of the top layer and the S velocity of the layer just above the source depth that control the Rayleigh waves. Perturbation to the mantle velocities (Figures 2.5i and 2.5j) reveals that the P velocity of the upper mantle only slightly affects the beginning part of the P_{nl} waves but the S velocity has substantial impact on the SV segments.

We get similar results with a corresponding set of perturbations to thicknesses, holding the velocities constant. Note that this is a range dependent effect and does not apply at less than 150 km, since the critical angle for the Moho reflection strongly depends on both the crustal velocity and the Moho depth. Well-known dispersion relationships suggest that, at distances beyond the critical angle, the thickness and velocity of each layer trade off considerably. For this reason, we will neglect these sensitivity tests in the interest of brevity.

2.3.3 Sensitivity tests on the Moho transition and the top mantle structure

To examine the effect of the crust-mantle transition on regional seismograms, or the resolution of regional seismograms to this transitional structure, seismograms from two crustal models are generated and compared (Figure 2.7). The difference between model *tbPB* (Table 2.1) and model *mohoPB* in the transitional structure results in slight changes in the high-frequency signals but not in the long period signals (Figure 2.7). At this distance, earthquakes have to have significant magnitude to be observed well, usually with longer source duration and producing longer-period signals at receivers, therefore, this test suggests that regional seismograms for crustal events are not well suited for modeling the Moho transition to high resolution.

The effect of a velocity gradient in the top mantle is displayed in Figure 2.8.

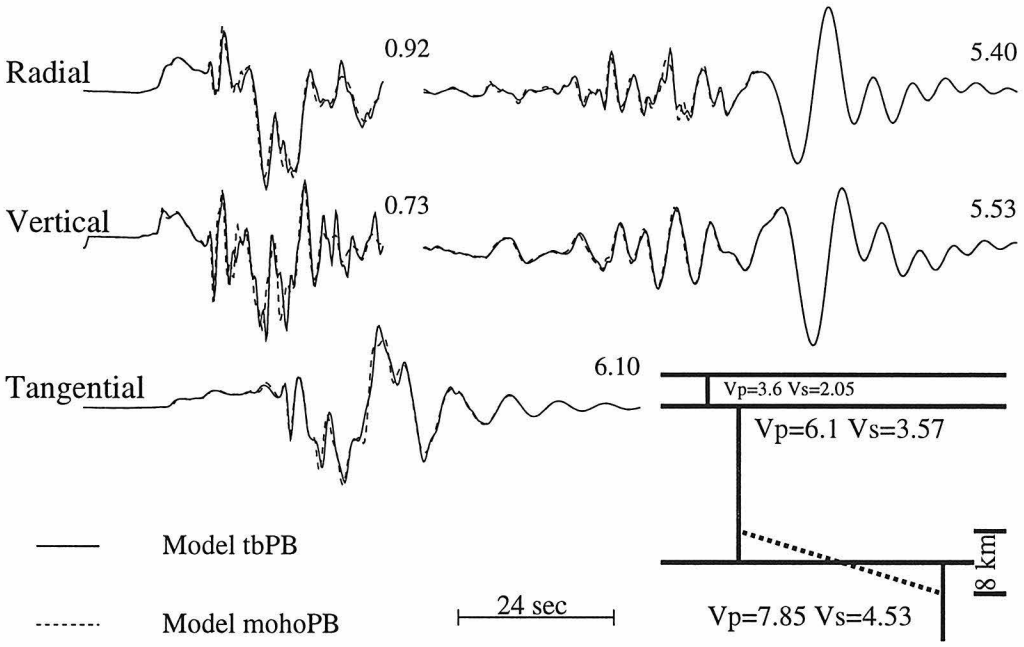

Figure 2.7: Comparison of synthetic displacement waveforms between models *tbPB* and *mohoPB*. The two models (lower right) differ by the fact that model *tbPB* has a sharp Moho while model *mohoPB* has an 8 km thick transition zone between the crust and the mantle. Each pair of seismograms is plotted on the same scale with the peak amplitude of the solid trace shown.

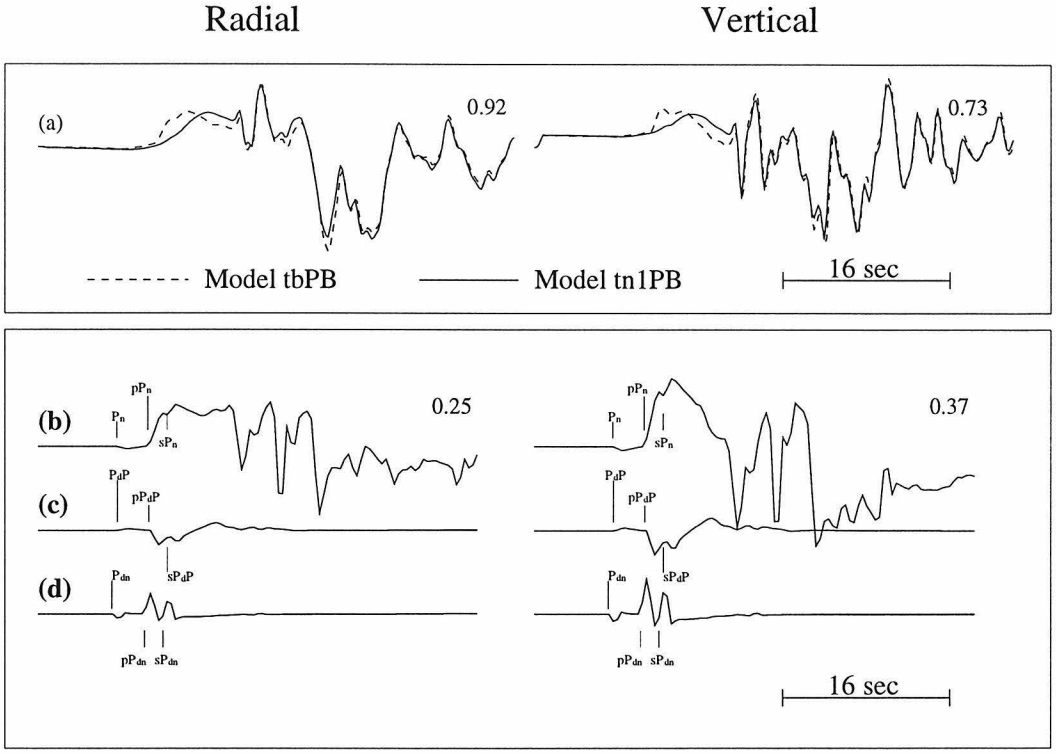

Figure 2.8: *(a)–(c)*Effects of a negative velocity gradient in the top mantle. **(a)** Comparison of the P_{nl} portion of the synthetic displacement waveforms between model *tbPB* and model *tn1PB*. Each pair of seismograms is scaled according to the solid trace with the peak amplitude shown. **(b)** A set of Moho-reflected rays calculated for model *tbPB* with GRT. **(c)** A set of rays reflected from a deeper discontinuity 10 km below the Moho, where the P velocity drops from 7.85 to 7.7 km/sec. **(d)** Effects of a positive velocity gradient in the top mantle. Shown here is a set of rays reflected from a deeper discontinuity 10 km below the Moho, where the P velocity jumps from 7.85 to 8.0 km/sec. Seismograms in *(b)–(d)* are scaled according to the ones in *(b)* with the peak amplitude shown. The subscript $_d$ donates reflected wave from the deeper discontinuity and the subscript $_{dn}$ donates head wave associated with this discontinuity.

As shown in Figure 2.8*b* and 2.8*c*, when there is a negative velocity gradient, rays reflected from the Moho are weakened by rays that are reflected from the deeper discontinuities below the Moho and have the opposite polarity. The net effect is that the beginning of the P_{nl} waves is reduced (Figure 2.8*a*). When the velocity gradient is positive, the effect is the opposite as displayed in Figure 2.8*d*.

In the above exercises, we fixed all other earthquake parameters and conducted our sensitivity tests on model parameters. Further studies also suggest that our results are qualitatively correct for a source-receiver distance range of 300 to 600 km, where the critical angle for the Moho reflection is passed and the surface wave dispersion is not very significant. Although crustal velocities are very important parameters in modeling regional seismograms, we have to keep in mind that other parameters such as crustal thickness, source depth, and source finiteness all contribute to the complexity of the regional broadband waveforms as addressed in some recent studies [*e.g. Dreger and Helmberger*, 1991b; *Saikia and Helmberger*, 1997; *Song and Helmberger*, 1996].

2.4 1-D modeling of the Basin and Range crustal structure

In this section, we model seismograms from three earthquakes with paths sampling the Basin and Range province (Figure 2.2) using 1-D models. The data used in this study are broadband displacement recordings of these earthquakes at seven TERRAscope stations. Event locations and origin times (Figure 2.2) are extracted from the TERRAscope network with the source parameters predetermined by other authors (Table 2.2). In the modeling process, the same criteria discussed in the last section are used for the time shift and the shape misfit, except that the SV wave and the Rayleigh wave are combined together to avoid instability in the cross-correlation procedure. To begin with, we select the *Priestley and Brune* [1978] model (model *PB*, Table 2.1), as a reference model. Generally, this is a good average structure in

Event	(strike, dip, rake)	Source time function (*sec*)	Depth (*km*)	Reference
Utah	(180^0, 50^0, 250^0)	(0.5, 0.5)	11	*Zhao and Helmberger* [1996]
Eureka	(37^0, 51^0, 282^0)	(1.0, 1.0)	11	Dreger(personal comm.)
Skull	(185^0, 45^0, 240^0)	(1.0, 1.0)	11	*Zhao and Helmberger* [1996]

Table 2.2: Source parameters of the three events studied.

modeling propagation paths in the Basin and Range province [*Zhao and Helmberger*, 1994]. Wave shape, especially that of the surface waves, produced by this model fits the data well when the proper shift is applied (e.g. Figure 2.1). However, the timing predicted by this model is not very satisfactory. While this model is too slow for the paths in the southern Basin and Range province, it is too fast for paths in the central Basin and Range province. Also the relative timing between the P_{nl} waves and the Rayleigh waves in the synthetics are often misaligned by a few seconds when compared to the data (Figure 2.1). In our exercise to model the paths in the central Basin and Range province, we seek to decrease the crust velocity in order to improve the timing prediction as well as to improve the waveform fits.

We begin by perturbing the top layer of the model. In our grid search approach, we find that the top layer thickness can range from 2.5 km to 3.5 km with appropriate velocity trade-off. More significant change to the top layer would result in too much change in the surface wave shape and timing, especially for the Rayleigh waves. This feature is consistent with the conclusion we derived earlier. We also find that the synthetic waveform fits to the data get worse for a larger velocity jump from the upper crust to the lower crust when it is produced by decreasing the upper crustal velocity alone. Next, we decrease the velocities in the lower crust to delay the synthetic waveforms and to adjust the relative timing between the P_{nl} wave and the Rayleigh wave. We find that when the lower crustal velocities are decreased to be the same as those of the upper crust, the resulting simple crust model is efficient in achieving both goals. Parameters of our preferred model, the tbPB model, are given in table 2.1 and the time shifts required for the best-fitting synthetics is given for each segment in Figures 2.9–2.11, 2.13–2.14, and 2.16–2.17.

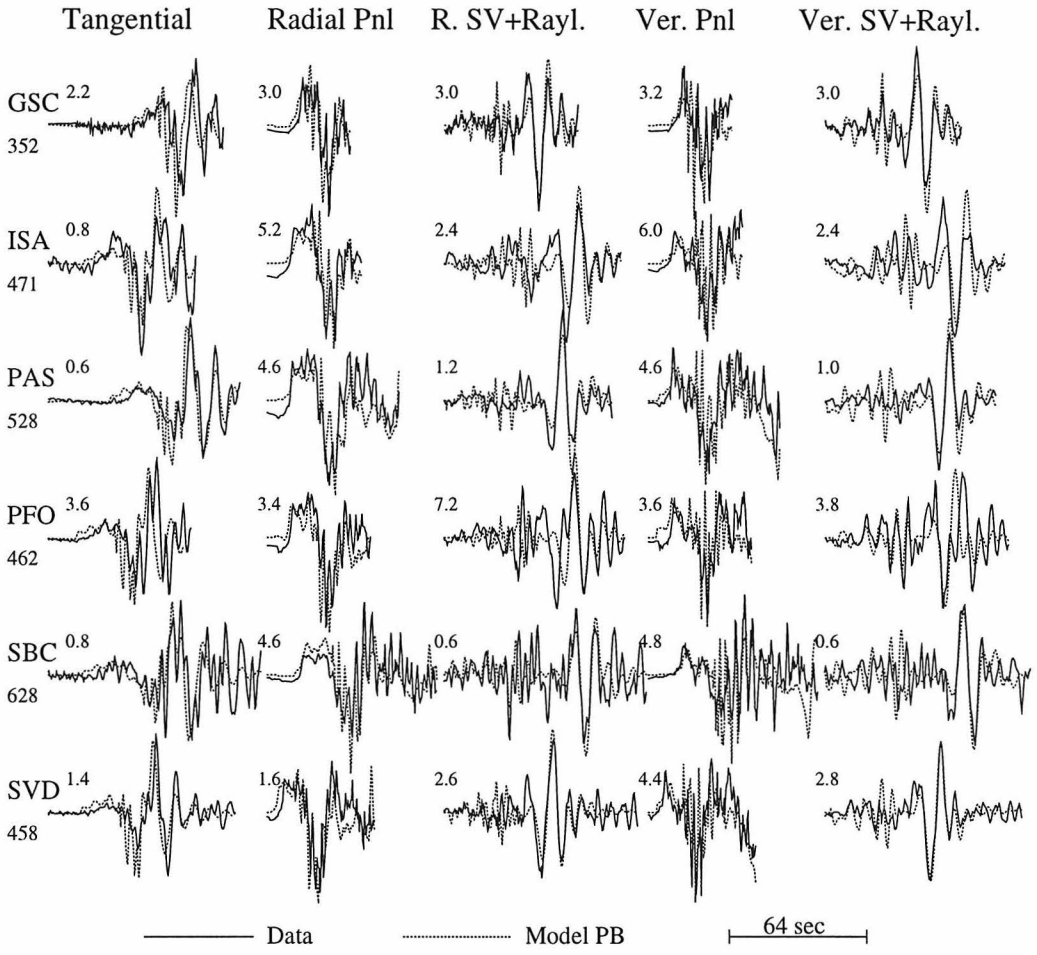

Figure 2.9: Comparison between displacement data and synthetic waveforms (Model *PB*) for the Utah event. The small number in the beginning of each pair indicates the time shift (in seconds) required for the synthetic waveform to fit the data. Station names and distance from the event are also shown.

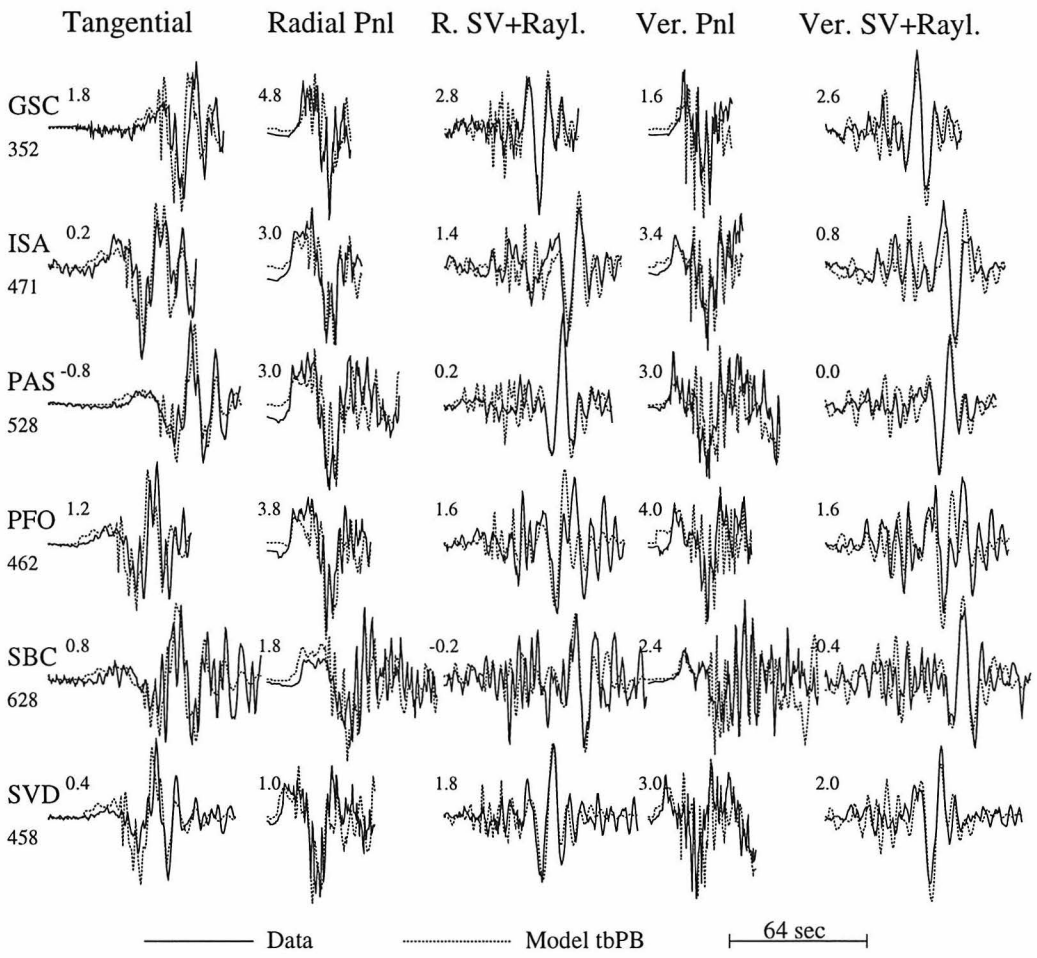

Figure 2.10: Comparison between displacement data and synthetic waveforms (Model *tbPB*) for the Utah event.

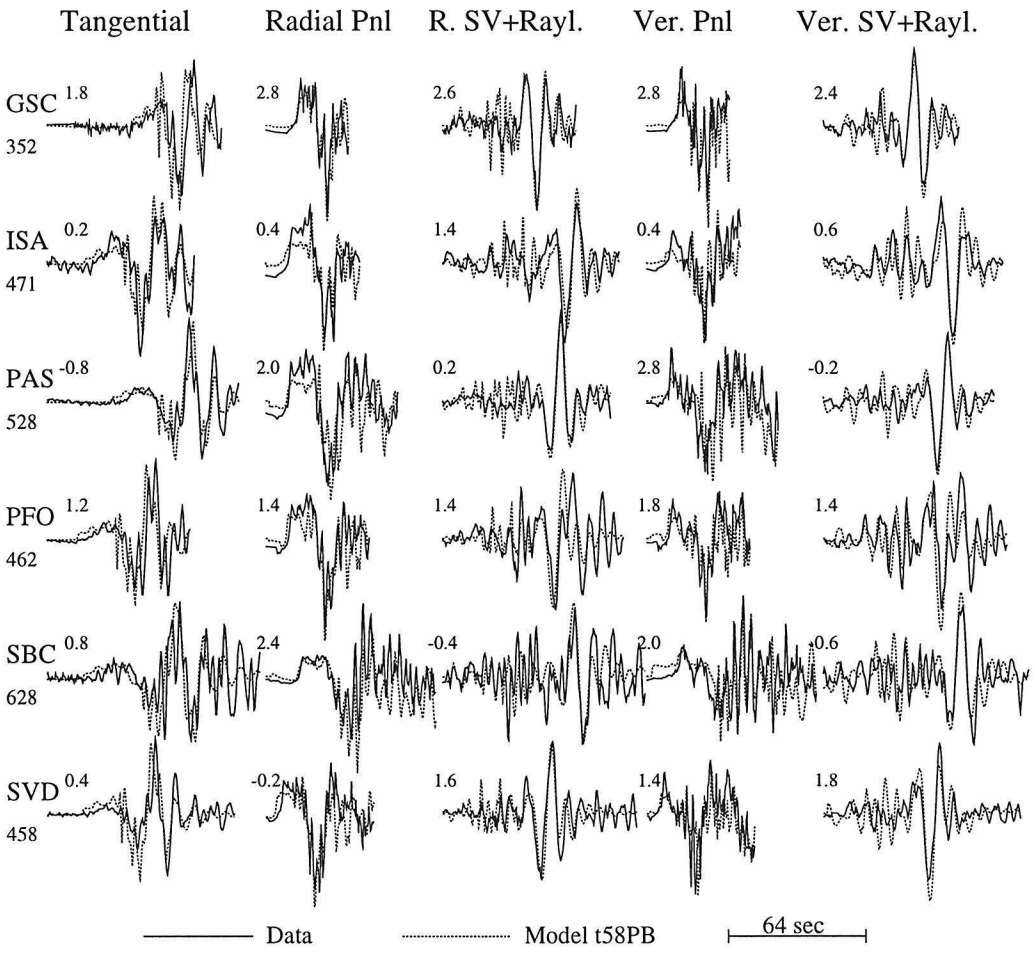

Figure 2.11: Comparison between displacement data and synthetic waveforms (Model *t58PB*) for the Utah event.

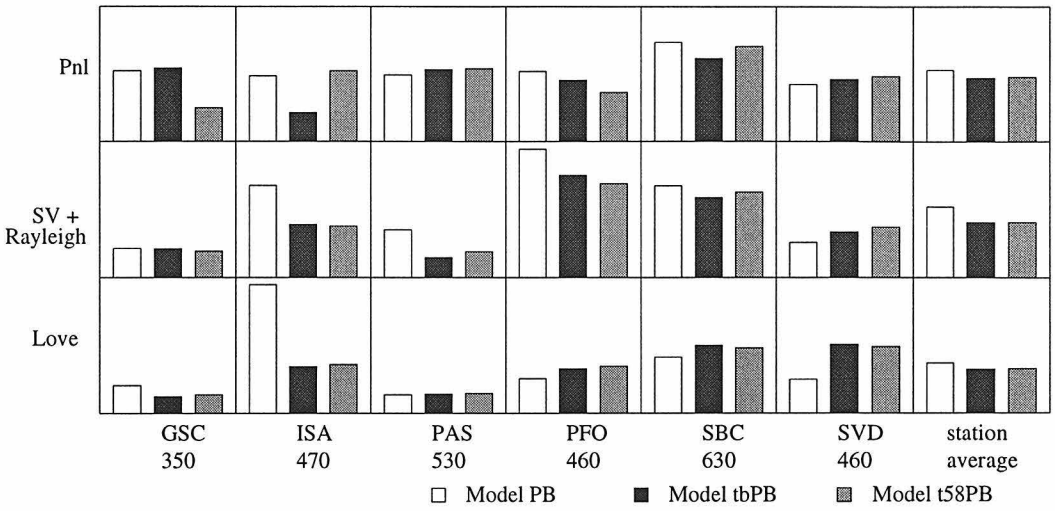

Figure 2.12: Shape misfit, represented by the height of the boxes, between data and synthetic waveforms for models *PB*, *tbPB*, and *t58PB* for the Utah event. Station names and distance from the event are also shown.

2.4.1 The Utah event

Zhao and Helmberger [1996] found that the *PB* model did better than the standard Southern California model in modeling this earthquake. In our study, we find that model *PB* is not slow enough, especially for the P_{nl} waves. When the Conrad discontinuity is removed, the timing for the P_{nl} waves and the separation between the P_{nl} wave and the Rayleigh wave are both improved substantially. The average shape misfit to the data is also reduced (Figure 2.12) with the most improvement at station ISA for all three segments. Note that the improvement in the wave shape of the Airy phase at station PFO eliminates the instability factor and reduces the time shift. For model *tbPB*, the timing between different segments on the synthetics is reasonably compatible, but the synthetics themselves are still too fast. As we further slow down the main crust V_p as in model *t58PB*, the predicted timing is even better with the wave shape fits being equally good (Figure 2.12).

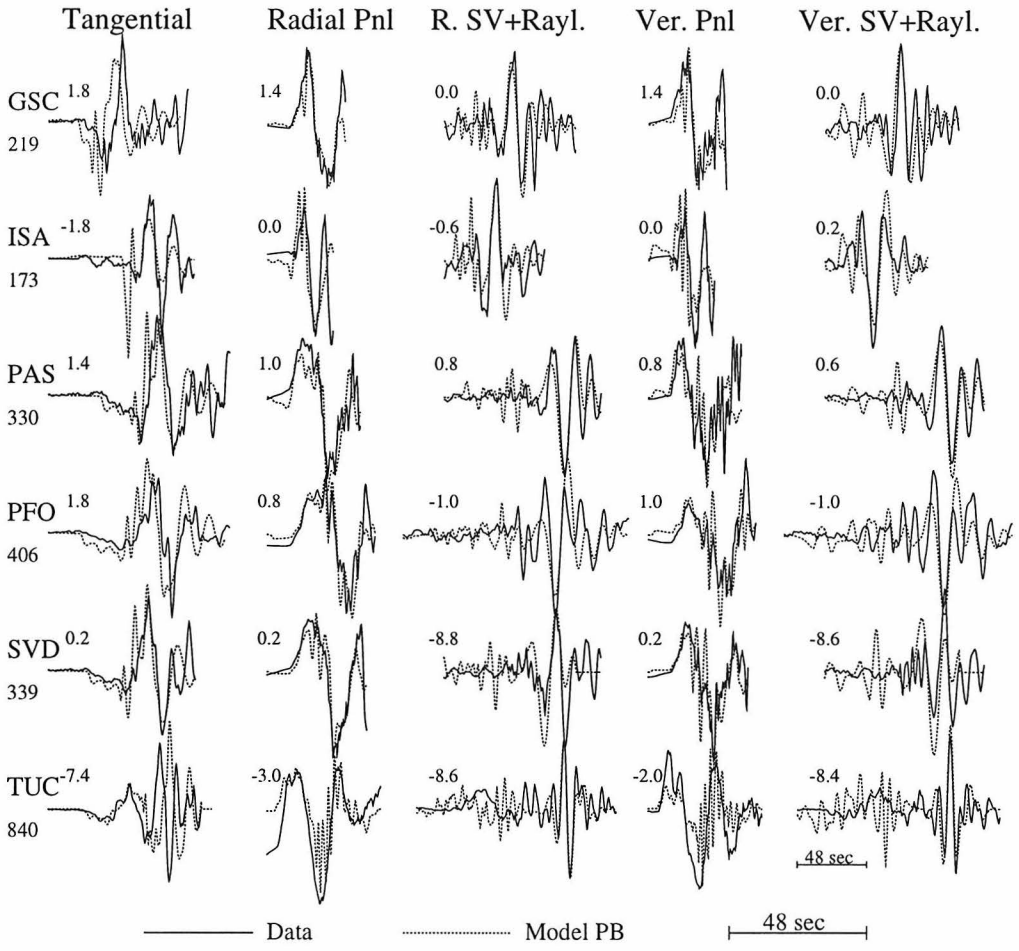

Figure 2.13: Comparison between displacement data and synthetic waveforms (Model *PB*) for the Eureka Valley event. Note a different time scale is used for station TUC.

2.4.2 The Eureka Valley event

For this event, model *PB* predicts good timing but model *tbPB* does even better (Figures 2.13and 2.14). The slower lower crust in model *tbPB* also improves the waveform fits, especially for station ISA (Figure 2.15). For station SVD, the Rayleigh wave timing problem of model *PB* is fixed as the relative strength of the two picks on the Rayleigh wave train is adjusted by model *tbPB*. This is also true for the Rayleigh waves at station TUC.

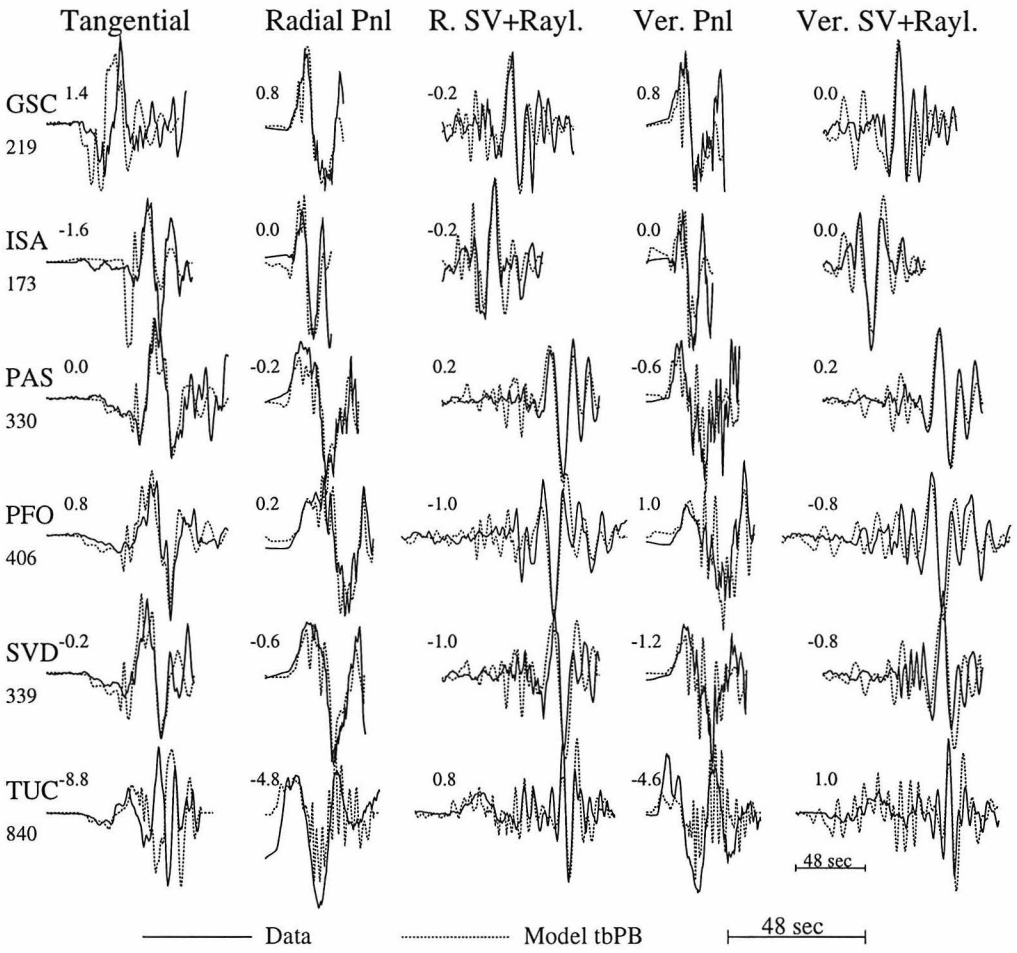

Figure 2.14: Comparison between displacement data and synthetic waveforms (Model *tbPB*) for the Eureka Valley event.

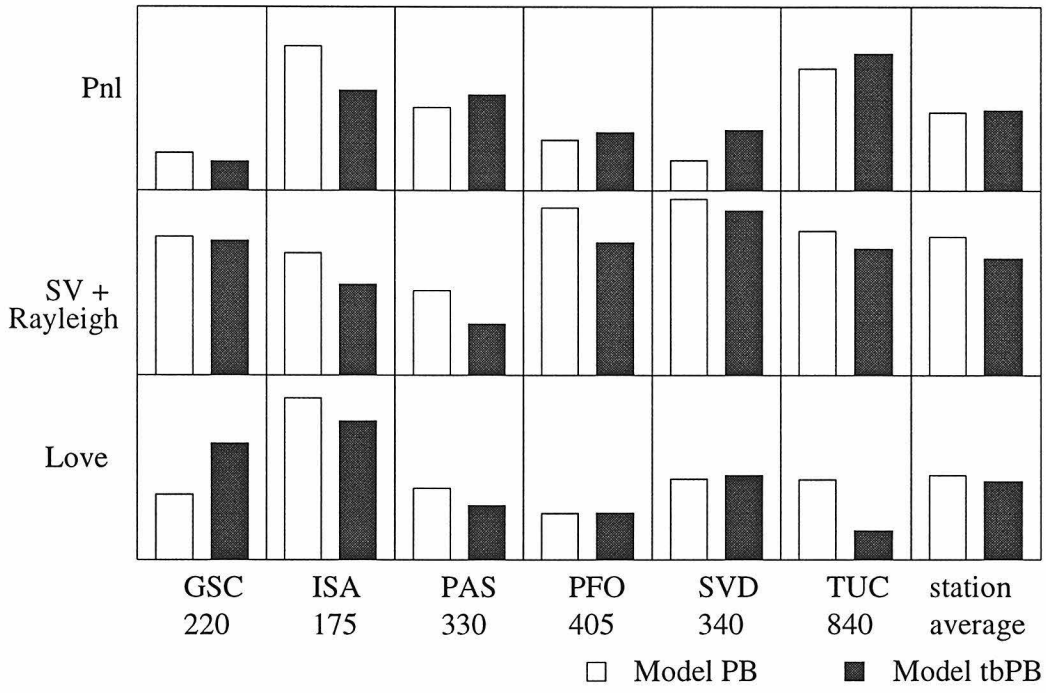

Figure 2.15: Shape misfit between data and synthetic waveforms for models *PB* and *tbPB* for the Eureka Valley event.

2.4.3 The Skull Mountain event

Among the three events studied, paths from this event to the various stations are the most difficult to model with a 1-D model. Although the *tbPB* model does a little better than the *PB* model, it is still too fast, especially for the Rayleigh waves (Figures 2.16–2.17). The Love waves are better modelled in timing than the Rayleigh waves, but the wave shape is not satisfactory. The positive time shift would suggest a slower model than *tbPB*, but our tests show that further slowing down the main crust as in model *t58PB* would make the wave shape even worse while only slightly improving the timing prediction. This is probably a case where lateral variation has a great effect. At this stage, we prefer model *tbPB* as an average 1-D model for these paths. Detailed 2-D modeling would be informative.

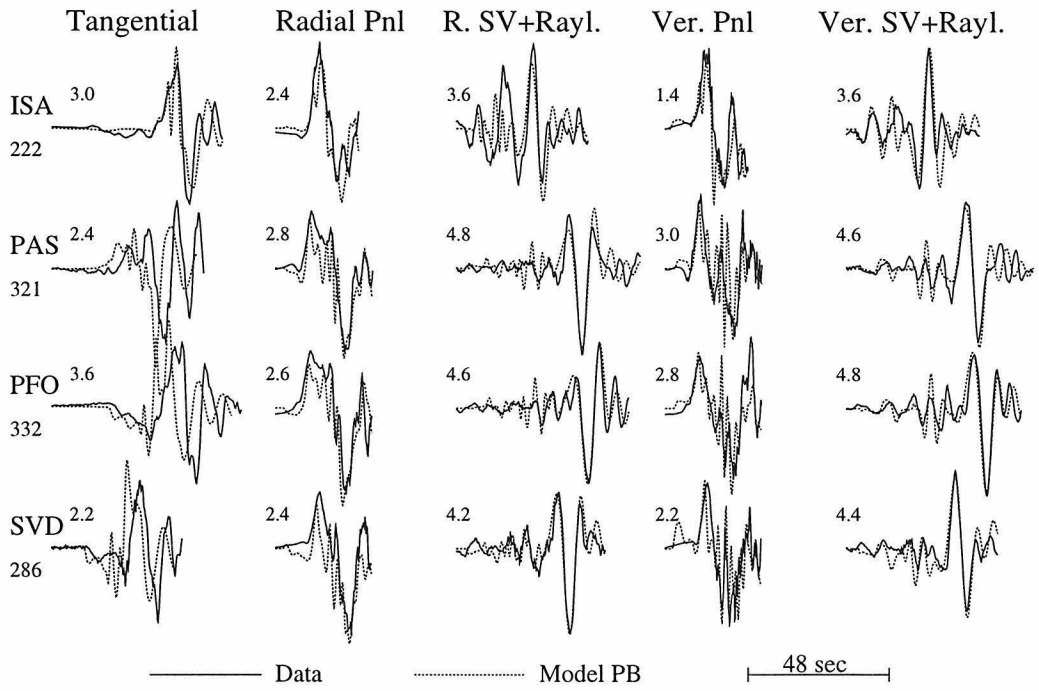

Figure 2.16: Comparison between displacement data and synthetic waveforms (Model *PB*) for the Skull Mountain event.

2.5 Discussion

Throughout the modeling in this study, we focused on 1-D models. Simple two-layer models worked well and we do not see any advantage in adding a Conrad discontinuity for paths from the three events to the various stations. Detailed studies by *Mori and Helmberger* [1996], who analyzed direct S and SmS energy from the 1992 Landers aftershocks recorded at stations GSC and PFO, reported compatible results. They found that SmS phases at station GSC are much stronger than the direct S phases but the reverse is true at station PFO. They attribute these observations to the more homogeneous crustal structure in the Mojave desert north of the Landers aftershocks, which allows large reflections from the Moho. From our modeling, we conclude that the Conrad is not a regional feature in the crust of this area.

However, that does not mean the whole crust in the Basin and Range is as simple as our 1-D models. Actually, the time shift between the different portions of the

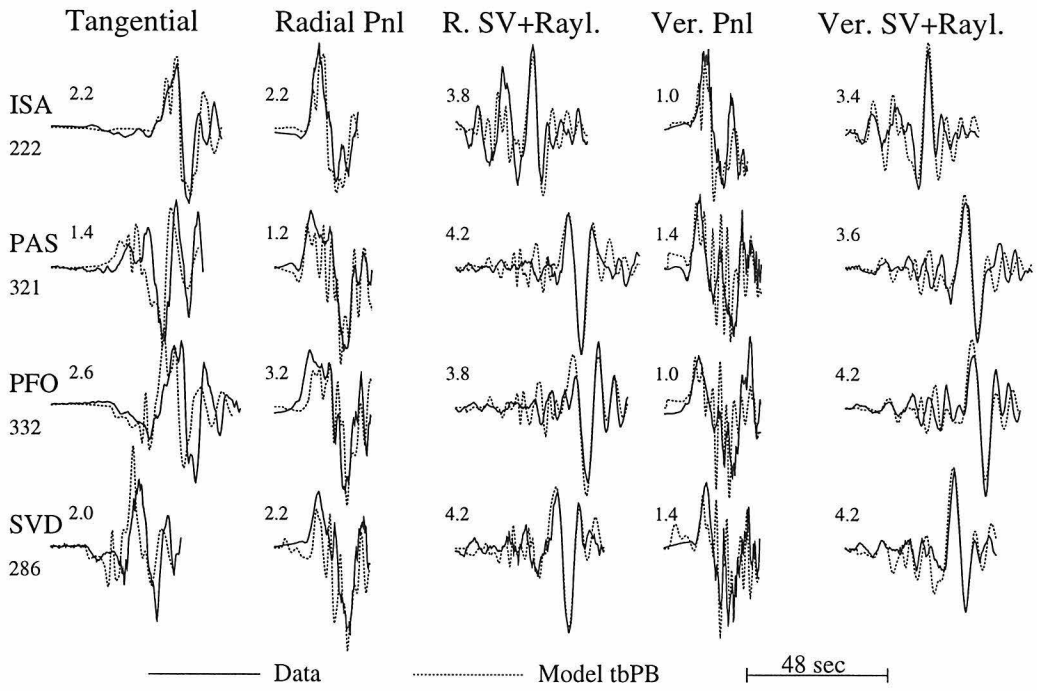

Figure 2.17: Comparison between displacement data and synthetic waveforms (Model *tbPB*) for the Skull Mountain event.

data and the synthetic waveforms for individual paths in Figures 2.19*a–c* indicate complicated lateral variations in the crustal velocity and crustal thickness. As seen in Figure 2.19*a*, the P_{nl} timing, which is controlled by the velocity in the mid-crust, reveals that the crust under the Sierra Nevada is faster than that under the northern Mojave desert. This feature is well resolved in the tomographic study of *Zhao and Kanamori* [1992] as displayed in Figure 2.19*d*.

The Love wave timing shown in Figure 2.19*b* is similar to that of the P_{nl} portion. This is partially due to the fact that, in our analysis, the timing of the tangential component as a whole, along some paths, is controlled by the down-going long-period S energy (Figures 2.13 and 2.16) which is controlled by the lower crust. The Rayleigh wave timing, however, show a quite different pattern (Figure 2.19*c*). Rayleigh waves from the Skull Mountain event to the various stations arrive substantially late, unlike the P_{nl} waves or the Love wave. This could have resulted from a slower upper crustal S velocity or from a slower P velocity in the top layer, as indicated in Figure 2.6.

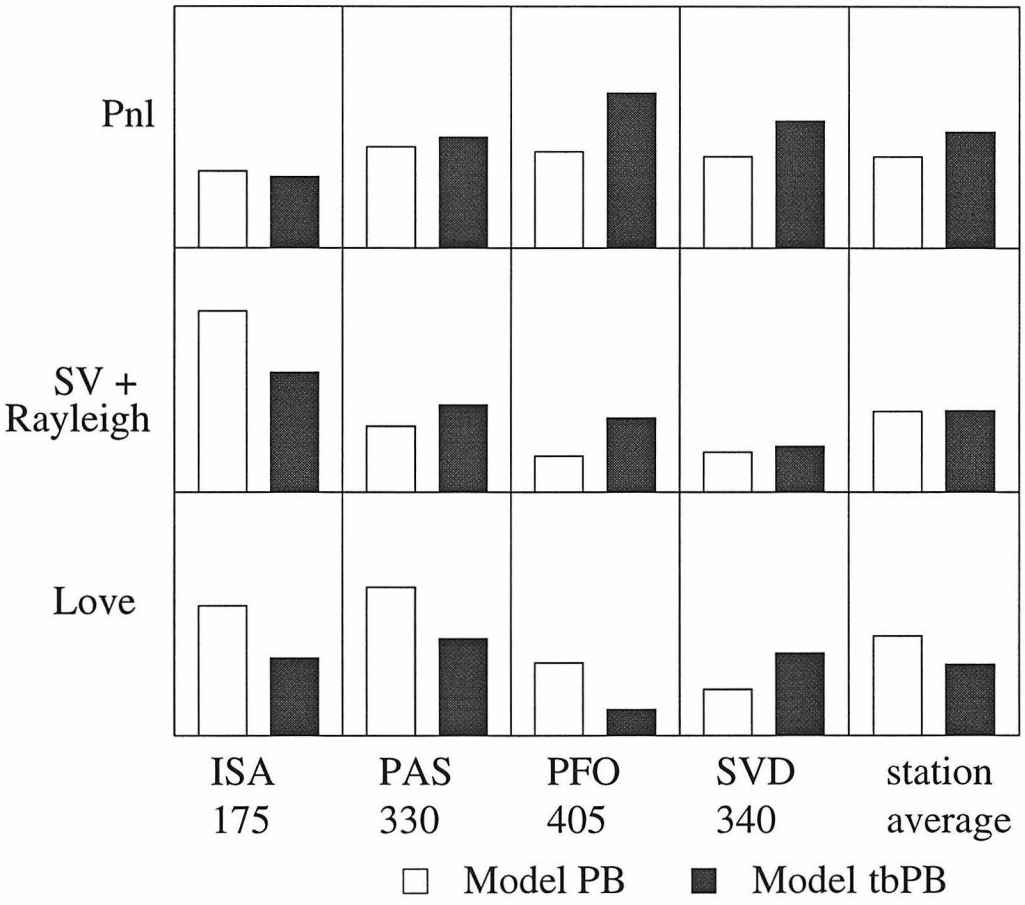

Figure 2.18: Shape misfit between data and synthetic waveforms for models *PB* and *tbPB* for the Skull Mountain event.

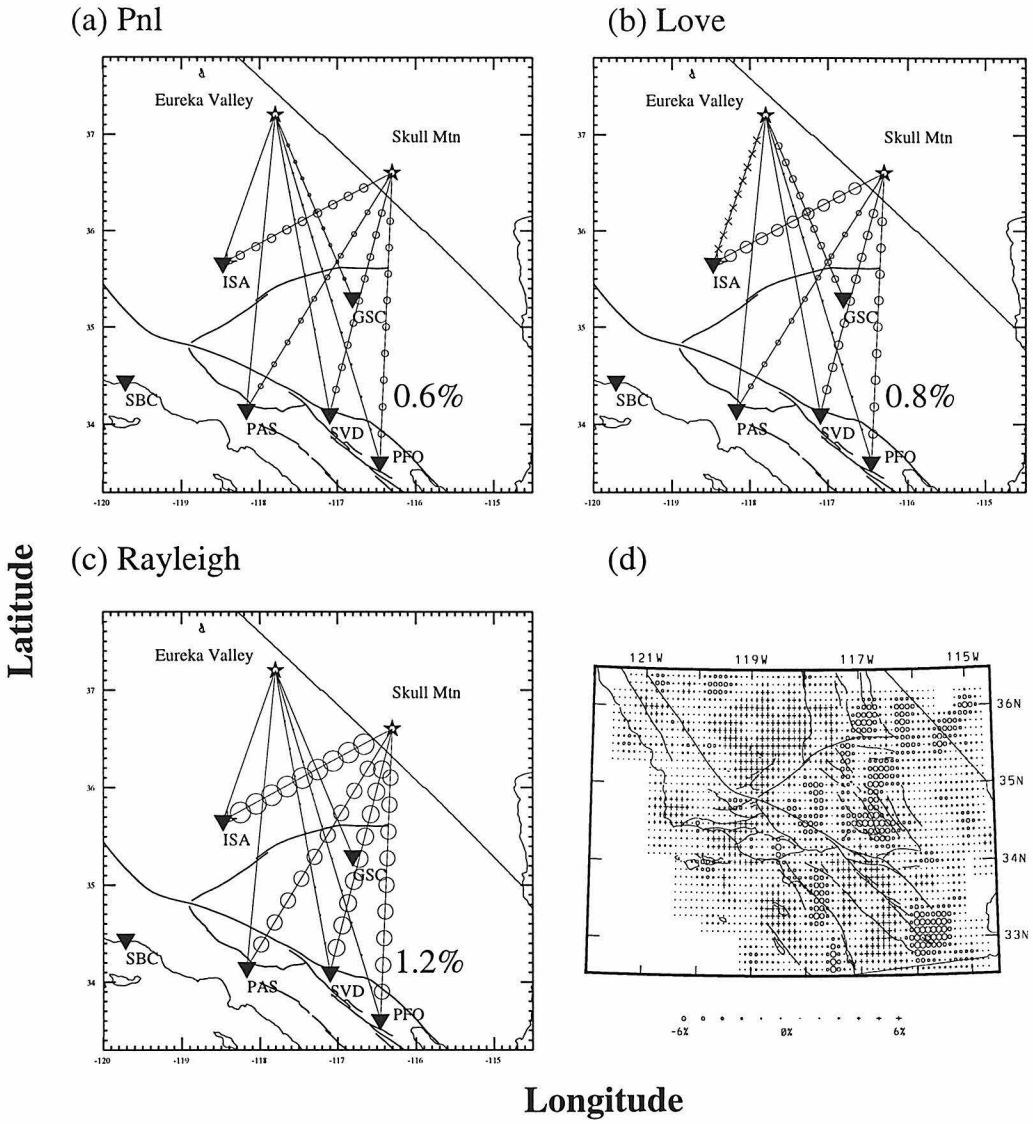

Figure 2.19: **(a)–(c)** Integral slowness of individual paths (relative to model tbPB), defined as the average time shift (shown in Figures 2.10, 2.14 and 2.17) scaled by the source-receiver distance, for each portion of the data. Circles and crosses denote slow and fast paths, respectively. Symbol size corresponds to the integral slowness of the path. For the path from the Skull Mountain event to the station PFO, this value is shown for each portion of the data. **(d)** A tomographic model for the Southern California crust, showing fractional *P*-wave velocity perturbations (in %) at 22 km depth. After Zhao and Kanamori [1992].

However, the first reason is unlikely since the Love wave timing is reasonably good. Notice that the waveforms from the Skull Mountain event are the least well modeled in this study; it is possible that the velocity variation in the top layer along these paths is quite substantial. As we mentioned earlier, data from the Utah event are fit the best by model *t58PB* while model *tbPB* works the best for paths from the Eureka event. This suggests that the crust under the northeastern Mojave has a smaller Poisson's ratio than the crust under the Sierra Nevada. If this is true, it would partially explain the fact that the Skull Mountain event was the most difficult to model with a 1-D model. The path from the Eureka Valley to the station Tucson (TUC), which runs from near the Sierra Nevada to the northeast Mojave desert and further to the southern Basin and Range, has this same problem. Detailed modeling for individual paths is necessary to retrieve more detailed information about the crustal structure.

2.6 Conclusions

In conclusion, we have conducted a set of sensitivity tests on the parameters of 1-D models to compare their impact on different segments of regional seismograms. We found that, for mid-crustal earthquakes, P_{nl} waves are controlled in broadband character by the mid-crust while the top layer contributes to the long period motions. The SV wave is mostly controlled by the shear wave velocity of the lower crust, especially the crustal layer just below the source depth. The top crustal layer controls the shape of the surface waves at ranges from 300 to 600 km, and the upper crust, especially the crustal layer just above the source depth, controls their timing. Applying these tests in modeling three earthquakes in the Basin and Range province, we found that a simple two-layer crustal model could effectively explain the data both in timing and in shape. The main crustal layer has P and S velocities of 6.1 km/sec and 3.6 km/sec, similar to those found by *Langston and Helmberger* [1974]. A surface layer of thickness 2.5 to 3.5 km is required to fit the Rayleigh waves. Modeling results also indicate that the crust under the northeast Mojave desert has slower P-velocity (5%)

than that under the Sierra Nevada.

Acknowledgements

We thank Lianshe Zhao for his help throughout this study. Chandan Saikia wrote the Modified Frequency-Wavenumber Algorithm. Craig Scrivner, Bradley Woods, Lupei Zhu, David Harkrider, Chandan Saikia, John Cassidy and one anonymous reviewer reviewed the manuscript. This research was supported by the Air Force through Grant Number F49620-93-1-0221. Contribution No. 5548, Division of Geological and Planetary Sciences, California Institute of Technology, Pasadena, California.

Chapter 3 Northridge aftershocks, a source study with TERRAscope data

3.1 Abstract

Broadband and long period displacement waveforms from a selection of Northridge aftershocks recorded by the TERRAscope array are modeled to study source characteristics. Source mechanisms and moments are determined with long-period data using an algorithm developed by *Zhao and Helmberger* [1994]. These results are compared with those by *Hauksson et al.* [1995] and *Thio and Kanamori* [1996]. The width of the direct pulses at the nearest stations PAS and CALB are measured as indications of the source duration. Another measurement of the source-time functions of these earthquakes is obtained by comparing the short-period to long-period energy ratio in the data to that in the synthetics. These measurements are used to estimate the relative stress drop using a formula given by *Cohn et al.* [1982]. The depth distribution of the relative stress drops indicates that the largest stress drops are in the depth range of 5-15 km for an aftershock population of 24 events. A correlation of extended surface wave-train with source depth is demonstrated for paths crossing the San Fernando Basin.

3.2 Introduction

The stress field and faulting in the Northridge area is of great importance to the understanding of the tectonics associated with the Transverse Ranges (Figure 3.1). Since most of the recorded earthquakes in this area occurred with no surface rupture, their source mechanisms provide essential information for the association of these earthquakes with certain known faults and to the identification of unknown faults

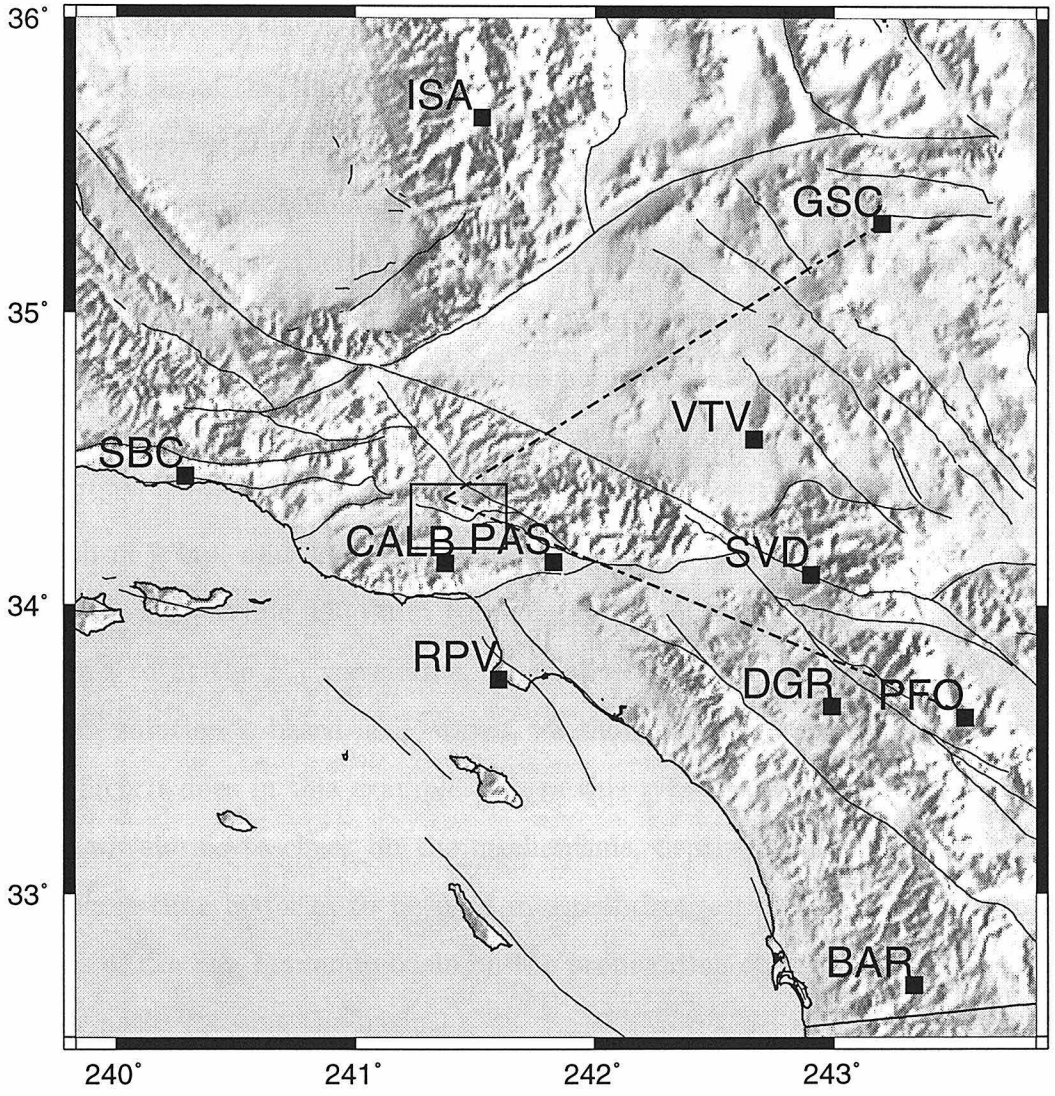

Figure 3.1: Map of Southern California showing TERRAscope stations (solid squares) used in this study and topographic features. The box indicates the Northridge area.

[*Hauksson et al.*, 1995]. Several studies have been carried out on the Northridge event and its aftershocks. For example, *Thio and Kanamori* [1996] used surface waves (period 10-40 sec) to study the source mechanism, depth and seismic moment of these earthquakes with a moment-tensor inversion technique [*Thio and Kanamori*, 1996]. With first-motion data from the Southern California Seismic Network, *Hauksson et al.* [1995] compiled a complete report of the source mechanisms, depths and local magnitudes of the Northridge sequence. Thio and Kanamori's [1996] solutions include many strike-slip and normal faulting while, in contrast, Hauksson *et al.*'s [1995] results show predominant thrust faulting. When the source mechanism results of the two studies agree, their depth estimates are similar. This is true for about half of the population. For the other half, the depth estimates by the two studies differ by an average of ± 5 km and the source mechanism results are distinctive from each other. One such example is shown in Figure 3.2. For this event (#0415), Hauksson *et al.*'s [1995] source mechanism solution is a thrust (strike 110, dip 55, rake 110) at a depth of 9 km, and Thio and Kanamori's [1996] is a strike-slip (231, 31, 1) at a depth of 5 km. While Thio and Kanamori's [1996] result predicts the amplitude well, it fails to fit the P_{nl} waveforms, especially at station GSC. Since Hauksson *et al.*'s [1995] solution is based on P-waves, we should expect the P_{nl} wave-train to fit better, which it does in this example. Given this type of discrepancy, we model the complete waveforms to check on the mechanisms, depths, and to determine the effective source-time histories to be used in stress-drop estimations. We also discuss the effects of the San Fernando basin on the propagation of the seismic energy along particular paths crossing the basin.

3.3 Data and methods

We choose to use Zhao and Helmberger's [1994] grid-search approach to estimate source mechanism and seismic moment. This method matches observed seismograms against synthetics over discrete wave-trains and allows relative time shifts between individual wave-trains, *e.g.*, the P_{nl} wave-train and the Rayleigh wave. This allows a

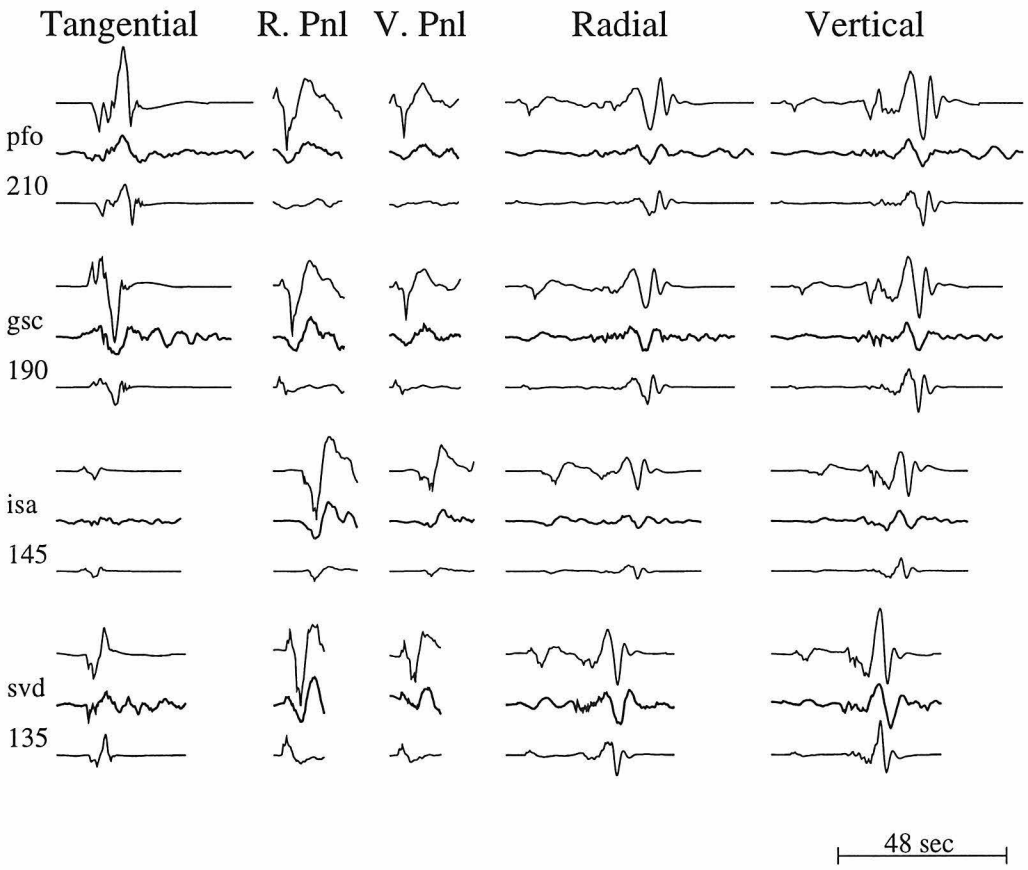

Figure 3.2: Comparison of data (heavy traces) and synthetics (light traces) for event #0415, after convolving with a long-period Press-Ewing instrument response. The top traces are synthetics with Hauksson *et al.*'s [1995] mechanism and depth. A moment of $1.0 \times 10^{23} dyne \cdot cm$ (corresponding to a local magnitude of M_L=4.6) is used for this solution. Seismograms at the bottom of each group are synthetics with Thio and Kanamori's [1996] source mechanism, depth and moment. Station name and epicentral distances are given. All seismograms for a same station are scaled by amplitude, with the P_{nl} waves blown up and shown separately. A triangular far-field source-time function with a duration of 0.4 sec is used. A small time shift is used to align synthetics with data.

better correlation between data and synthetic waveforms and desensitizes the source-mechanism result to the crustal model used to generate the synthetics [*Zhao and Helmberger*, 1994; *Zhu and Helmberger*, 1996a]. Source depth is determined by cycling through different values (5, 8, 11, 14, 17, and 20 km).

With this method, we studied 24 aftershocks with M_L in the range of 4.0 to 5.6. These events are large enough to be recorded at the regional stations with high signal-to-noise ratio. For some of the small events, broadband data is noisy but long-period data is reliable. In our source estimation process, we apply a long-period Press-Ewing (LP3090) instrument response on both data and synthetics for all events studied to obtain stable long-period estimates of M_0. We use Green's functions generated by *Dreger* [1992] for the standard Southern California model, using a reflectivity method [*Fuchs and Müller*, 1971; *Bouchon*, 1981; *Saikia*, 1994a]. An example of the fit between data and synthetics determined by this procedure is shown in Figure 3.3. The P_{nl} waves and Rayleigh waves are fit well, but the Love wave data are more complicated than corresponding synthetics.

It is usually difficult to retrieve the source-time history by matching a set of synthetics to broadband seismograms, since many stations have some high frequency ringing, such as station SVD (Figure 3.4). A relatively simple procedure is to equalize the energy content in different frequency band between data and synthetics [*Zhao and Helmberger*, 1996; *Jones and Helmberger*, 1996]. We apply the Wood-Anderson short-period instrument response (WASP) to both data and synthetics in order to compute the short-period energy. To obtain an estimate of the source time history, we match the short-period (WASP) to long-period (LP3090) energy ratio in the observed P_{nl} wave-train to synthetics. Symmetric trapezoidal source-time functions are assumed. Figure 3.4 displays the broadband data and the synthetics with this far-field source-time function, and the source mechanism determined with the long-period data (Figure 3.3). In this example, a (0.2, 0.2 sec) triangle fits the best, that is, a source duration of 0.4 sec. Note the match of the frequency content in the data and synthetics, especially for the P_{nl} wave-train.

A more traditional and straight forward estimate of the source duration can be

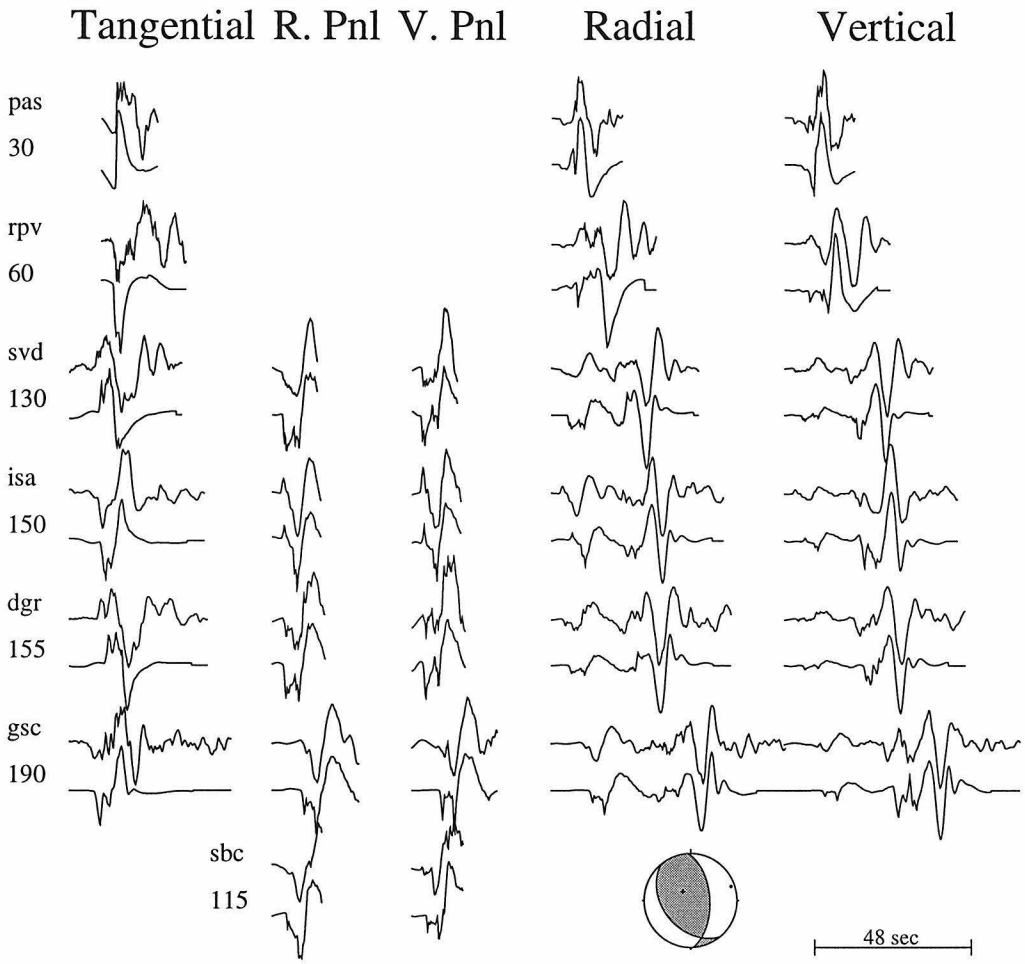

Figure 3.3: Comparison of long-period displacement data (event #1839) and corresponding synthetics for the mechanism displayed, as determined with the grid-search method ($M_0 = 8.5 \times 10^{22} dyne \cdot cm$). A source depth of 14 km and a triangular far-field source-time function with a duration of 0.48 sec are used. All seismograms are scaled to unit height. There is a 25% standard variation for the seismic moment.

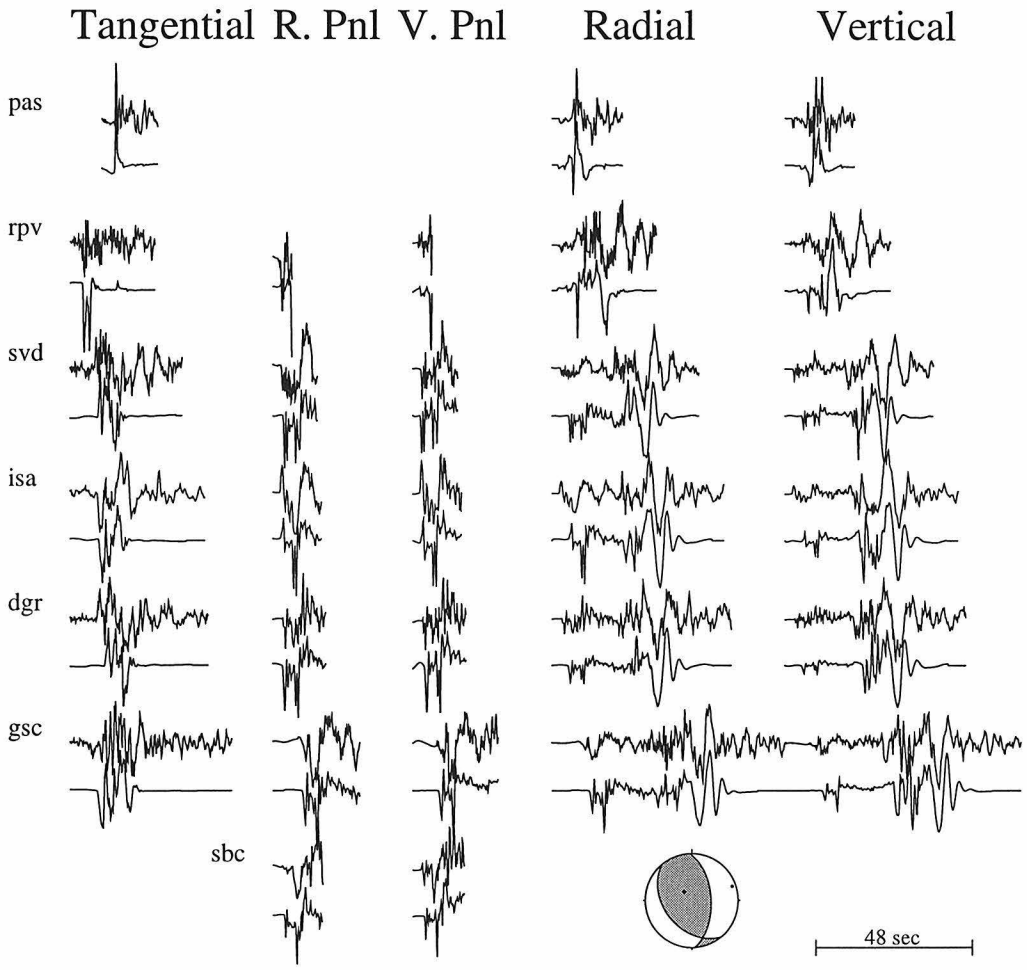

Figure 3.4: Comparison of broadband displacement data (event #1839) and corresponding synthetics for the mechanism displayed in Figure 3.3.

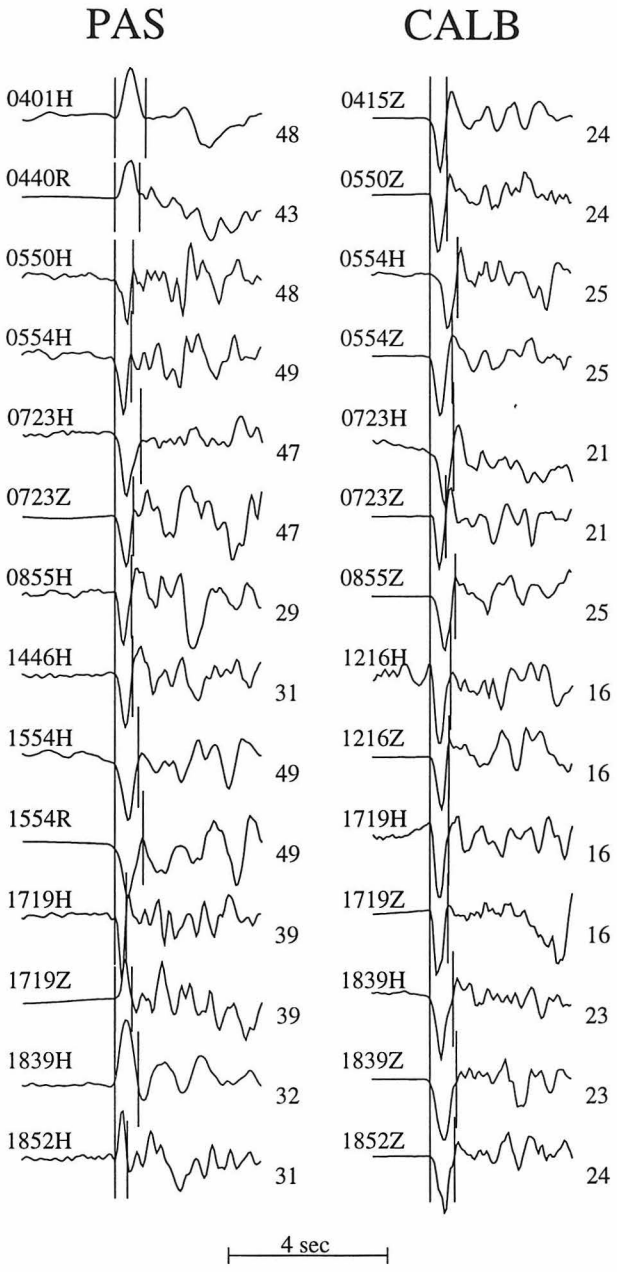

Figure 3.5: Some of the direct pulses recorded at stations PAS and CALB from which we are able to measure the source duration. Vertical lines indicate the measured duration. Small numbers show source-receiver distances in km. "H", "R", and "Z" following event numbers indicate tangential, radial and vertical components, respectively.

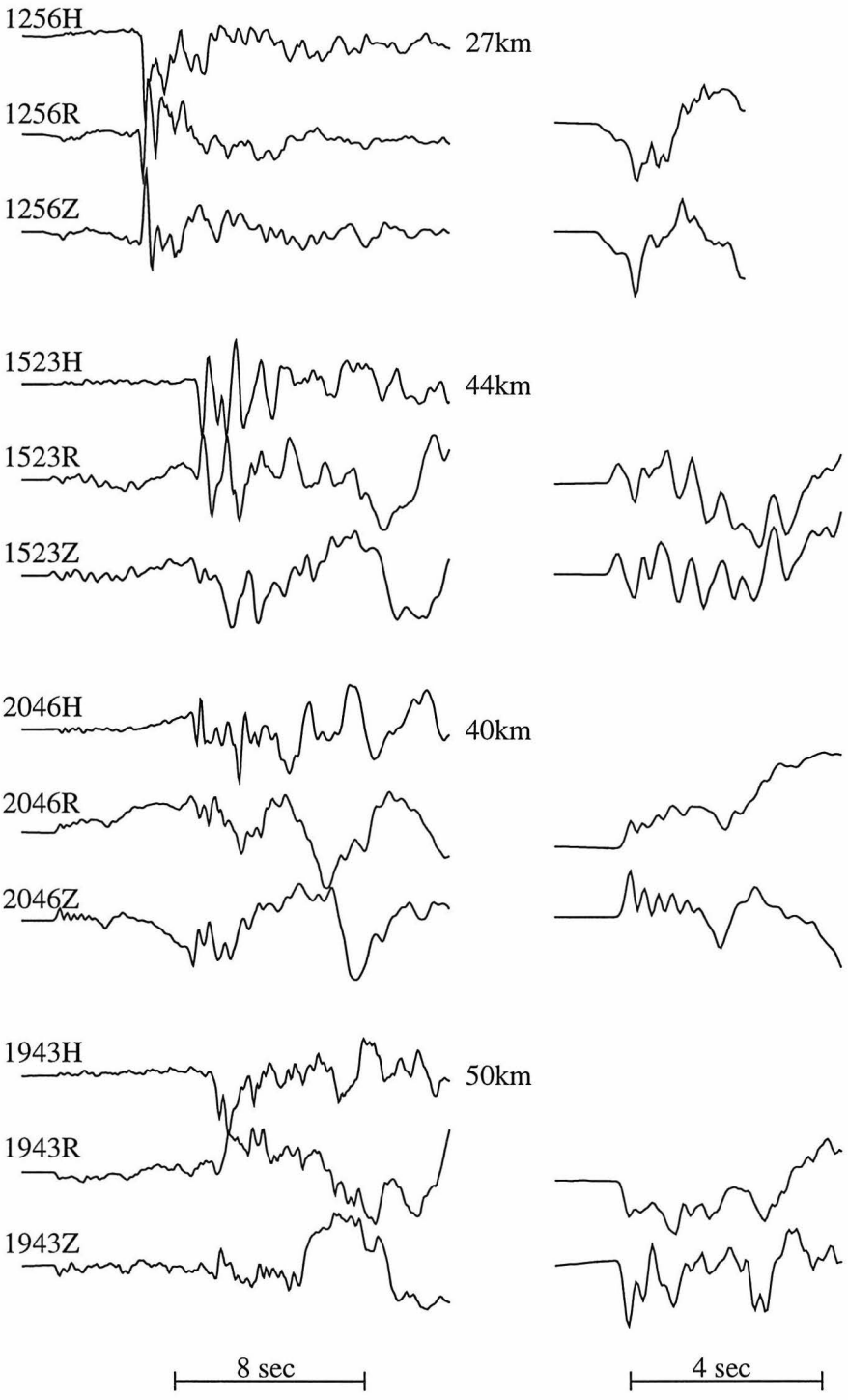

Figure 3.6: Some of the more complicated records at station PAS, for which direct measurement of the pulse width is difficult. The P_{nl} segment is blown up to the right. Epicentral distances are given.

obtained by measuring the width of the direct pulse at local stations [*e.g. Hardebeck and Hauksson*, 1997]. Many of the aftershocks were recorded at stations PAS and CALB, with source-receiver distances less than 50 km. Figure 3.5 displays some of the direct P-wave pulses recorded at these two stations from which we were able to measure the source durations. For events shown in this figure, we get similar results at PAS and CALB, although there is some variation of the pulse width between these two stations. For other events in the data set, especially large events and those with complex sources (Figure 3.6), we were not able to apply this kind of measurement. However, for those events to which both Zhao and Helmberger's [1996] energy ratio method and the direct measurement can be applied, a good correlation exists between the two measurements (Figure 3.7), except for an offset. The offset is expected because the synthetics in Figure 3.4 do not contain scattering as the data does. Because of this correlation, Zhao and Helmberger's [1996] method appears to be a good alternative to the direct measurement. It is a rough measurement of the asperity content in the source process and should be useful for the purpose of obtaining relative source duration from event to event in the same region, since path scattering properties should be nearly constant.

To measure the stress drop of an earthquake, many researchers [*e.g. Cohn et al.*, 1982; *Jones*, 1995] have used the empirical formula

$$\Delta\sigma(bar) = \frac{1.84 \times 10^{-22} M_o(dyn \cdot cm)}{\tau^3(sec)}. \tag{3.1}$$

M_0 is the long-period seismic moment and τ is the source duration. This formula assumes that the stress drop due to faulting is equal to the effective stress accelerating the fault as it ruptures [*Cohn et al.*, 1982]. It is a rough measurement of the stress drop of an earthquake. For the seismic moment, M_0, the moment-magnitude scale $M_0 = 10^{16.1+1.5M_L}$ [*Thatcher and Hanks*, 1973; *Hanks and Kanamori*, 1979] has been widely used [*e.g. Cohn et al.*, 1982; *Hardebeck and Hauksson*, 1997]. In this study, we use the seismic moment obtained by grid-search, discussed above, and the source duration estimated with Zhao and Helmberger's [1996] method to calculate the relative stress

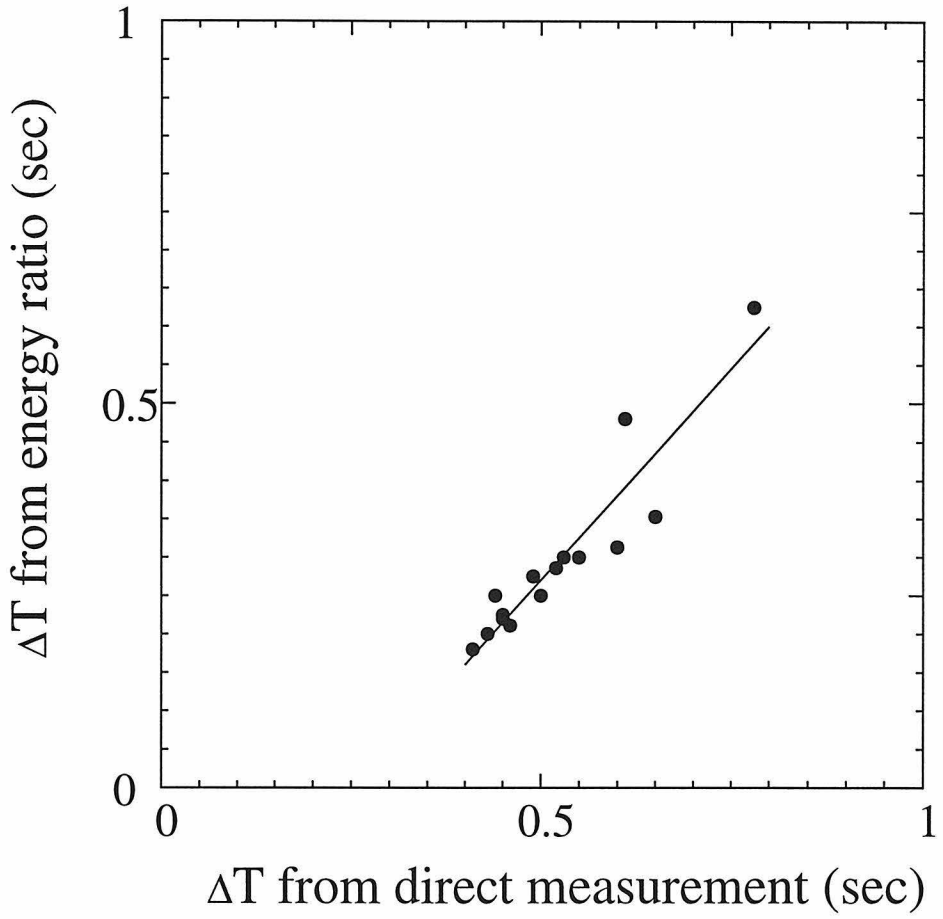

Figure 3.7: Comparison of two source duration measurements of the Northridge aftershocks.

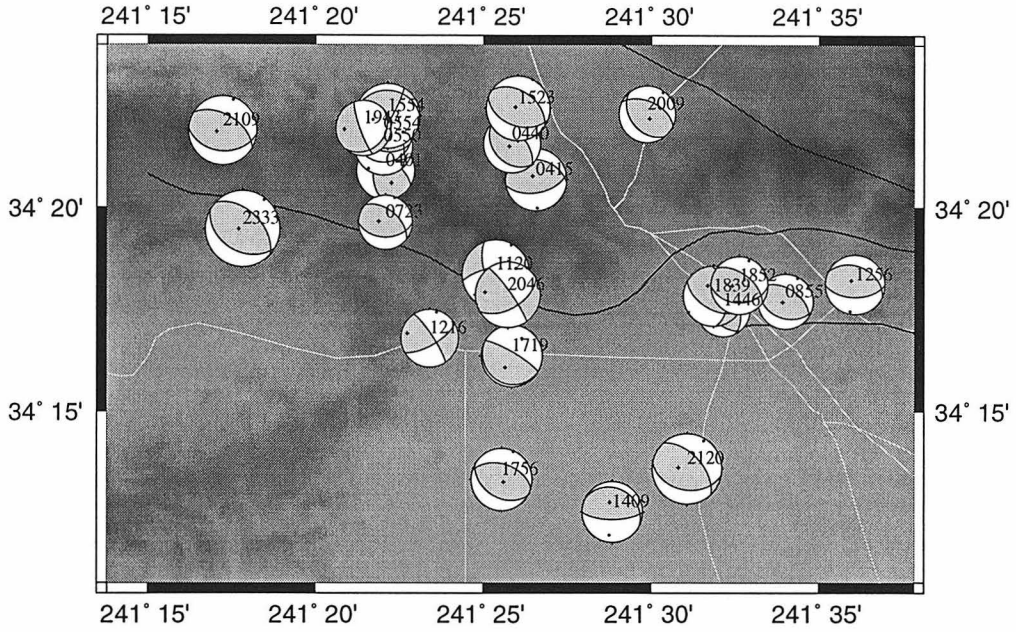

Figure 3.8: Source mechanisms of the Northridge aftershocks as determined in this study with the grid-search method of *Zhao and Helmberger* [1994].

drop with equation (1). Because of the nature of the relative source duration measured with the energy ratio method, the absolute value of this stress drop calculation is not comparable between events from different regions. But for a group of events in the same region, comparing this value is parallel to the comparison of the stress drop. In this sense, we call it relative stress drop.

3.4 Results

Estimates of the source mechanism, long-period seismic moment, depth, and source duration were obtained for 24 of the best recorded aftershocks. These results are summarized in Table 3.1. Our depth results are compatible with Hauksson *et al.*'s [1995] and are not shown in this table. The source mechanisms are also shown in Figure 3.8 at the corresponding source locations. In comparison to the two studies mentioned above, our results are closest to those of *Hauksson et al.* [1995]. The

adjustments are mainly necessary to produce better fit to the Rayleigh waves and to predict better amplitude ratios between the components.

In Figure 3.9, the seismic moments from this study and those given by *Thio and Kanamori* [1996] are compared with respect the local magnitude M_L, given by *Hauksson et al.* [1995]. A straight-line moment-magnitude scale ($M_0 = 10^{15.0+1.7M_L}$) for this group of events is also plotted in the same figure. Although these data points follow this scale closer than the well known *Thatcher and Hanks* [1973] scale, they fall well in the scatter of the data points for Thatcher and Hanks's [1973] much larger population of Southern California earthquakes. In fact, the much larger Northridge mainshock, with $M_o = (1.4 \pm 0.9) \times 10^{26} dyne \cdot cm$ [*Song et al.*, 1995a] and $M_L = 6.7$ [*Hauksson et al.*, 1995], falls closer to the *Thatcher and Hanks* [1973] scale.

Figure 3.10 shows the distribution of the relative stress drop with respect to the focal depth. Figure 3.10*a* uses source depth determined by *Hauksson et al.* [1995]. Larger events tend to have higher stress drop compared to small ones. High stress drop events appear at a depth range of 8 to 15 km. For comparison, in Figure 3.10*b*, the same relative stress drop is plotted against the focal depth determined by Mori (personal communication), who conducted the relocation of these events with a 3-D crustal model for the Northridge area. The same features are seen but the high stress-drop zone appears shallower (5 to 13 km).

3.5 Discussion and summary

Throughout this study, we found the Northridge data set to be more complicated than data sets examined in previous TERRAscope studies [*e.g. Dreger and Helmberger*, 1991a; *Jones*, 1995; *Song et al.*, 1996]. The long period waveform data proved relatively easy to work with, but modeling the broadband data often required special treatment, both in source descriptions and in propagation operators. Figures 3.11 and 3.12 show an example (event #1120) of the more complicated events, modeled as a simple source and as a double event. In Figure 3.11, we compare the broadband displacement data and the corresponding synthetics determined by the grid-search

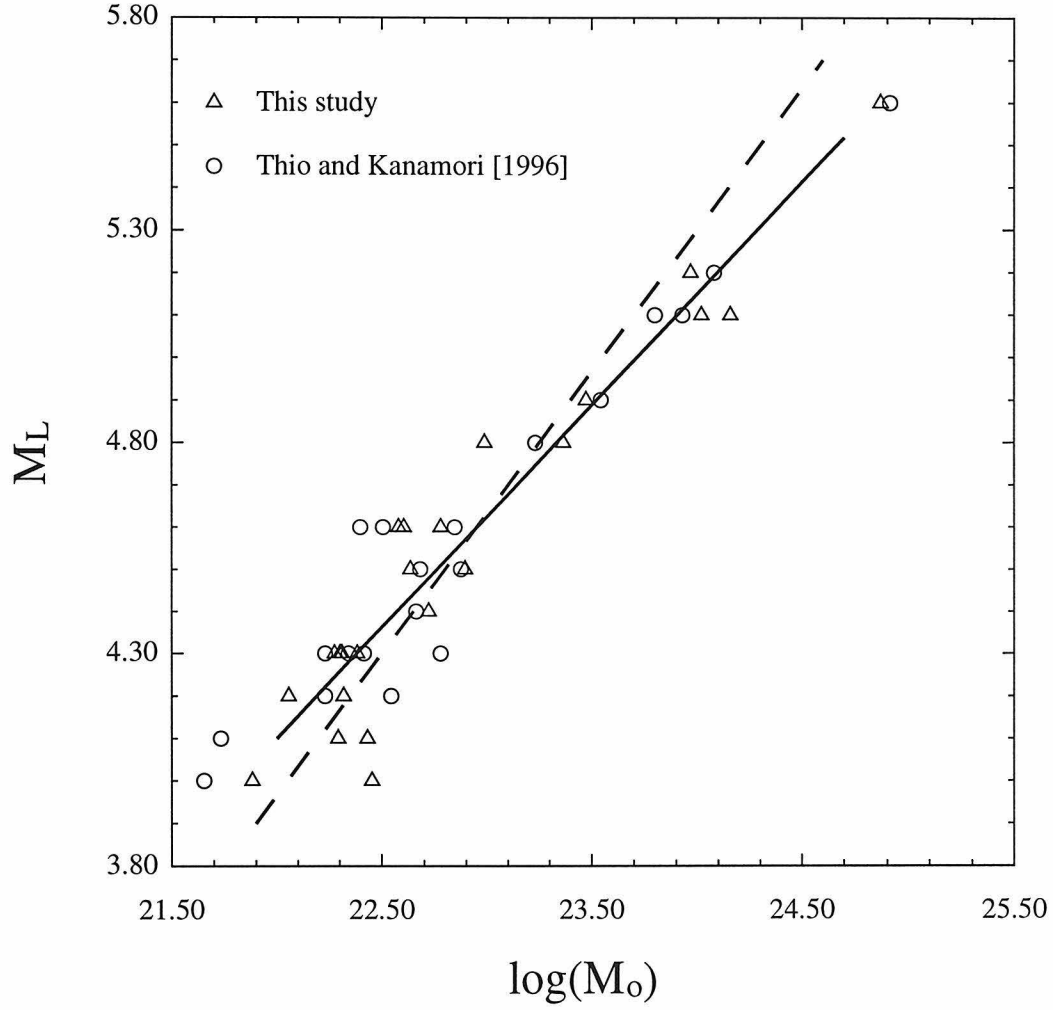

Figure 3.9: Comparison of long-period seismic moment given in this study and those by *Thio and Kanamori* [1996], with respect to M_L *Hauksson et al.* [1995]. The dashed line corresponds to the moment-magnitude scale given by *Thatcher and Hanks* [1973] for most California events.

$Date^1$	$hh:mm^1$	sec^1	$Depth^1$ (km)	M_L^1	θ^2 (^{0})	δ^2 (^{0})	λ^2 (^{0})	M_0^2 (dyn-cm)	ΔT_P^3 (sec)	ΔT_E^4 (sec)
940117	1554	10.54	13.3	4.8	30	80	70	1.4e23	0.7	0.35
940117	1756	07.96	19.7	4.6	130	35	100	6.0e22	0.5	0.25
940117	1943	53.17	13.8	4.1	160	80	250	2.4e22		0.35
940117	2046	02.12	10.1	4.9	60	55	10	3.8e23		0.45
940117	2333	30.47	11.1	5.6	120	40	80	9.3e24		1.01
940118	0401	26.03	0.3	4.3	185	55	140	3.1e22	0.8	0.62
940118	0723	55.77	15.9	4.0	90	45	60	2.7e22	0.5	0.30
940118	1523	46.60	9.2	4.8	110	45	80	2.5e23		0.28
940119	0440	47.67	3.1	4.3	315	55	90	3.3e22	0.6	0.31
940119	1409	14.51	18.9	4.5	90	70	80	4.8e22	0.4	0.25
940119	1446	34.96	7.3	4.0	140	50	80	8.4e21	0.5	0.23
940119	2109	28.33	14.3	5.1	95	40	70	1.1e24		0.56
940121	1839	15.05	10.6	4.5	140	40	60	8.5e22	0.6	0.48
940121	1852	44.00	8.9	4.3	90	40	60	2.4e22	0.5	0.21
940123	0855	08.42	9.7	4.1	110	40	80	2.1e22	0.5	0.29
940124	0415	18.55	8.9	4.6	80	55	80	4.8e22	0.4	0.20
940124	0550	24.13	12.1	4.3	110	55	70	2.9e22	0.5	0.22
940124	0554	20.82	10.9	4.2	110	40	70	2.3e22	0.6	0.30
940127	1719	58.58	16.3	4.6	120	10	90	4.3e22	0.4	0.18
940128	2009	53.39	4.0	4.2	140	40	110	1.9e22		0.55
940129	1120	35.60	1.6	5.1	160	65	160	1.5e24		0.81
940129	1216	56.08	3.6	4.3	60	70	10	2.3e22	0.5	0.28
940320	2120	12.03	14.7	5.2	100	40	60	9.9e23		0.41
940525	1256	56.84	11.6	4.4	90	55	75	6.7e22		0.35

Table 3.1: Source parameters for selected Northridge aftershocks. Note:
1. After *Hauksson et al.* [1995];
2. θ – strike, δ – dip angle, λ – rake angle, M_0 – long period moment;
3. ΔT_P – Source duration measured on TERRAscope stations PAS and CALB;
4. ΔT_E – Source duration determined by comparing short-period to long-period energy ratio in the data to that in the synthetic.

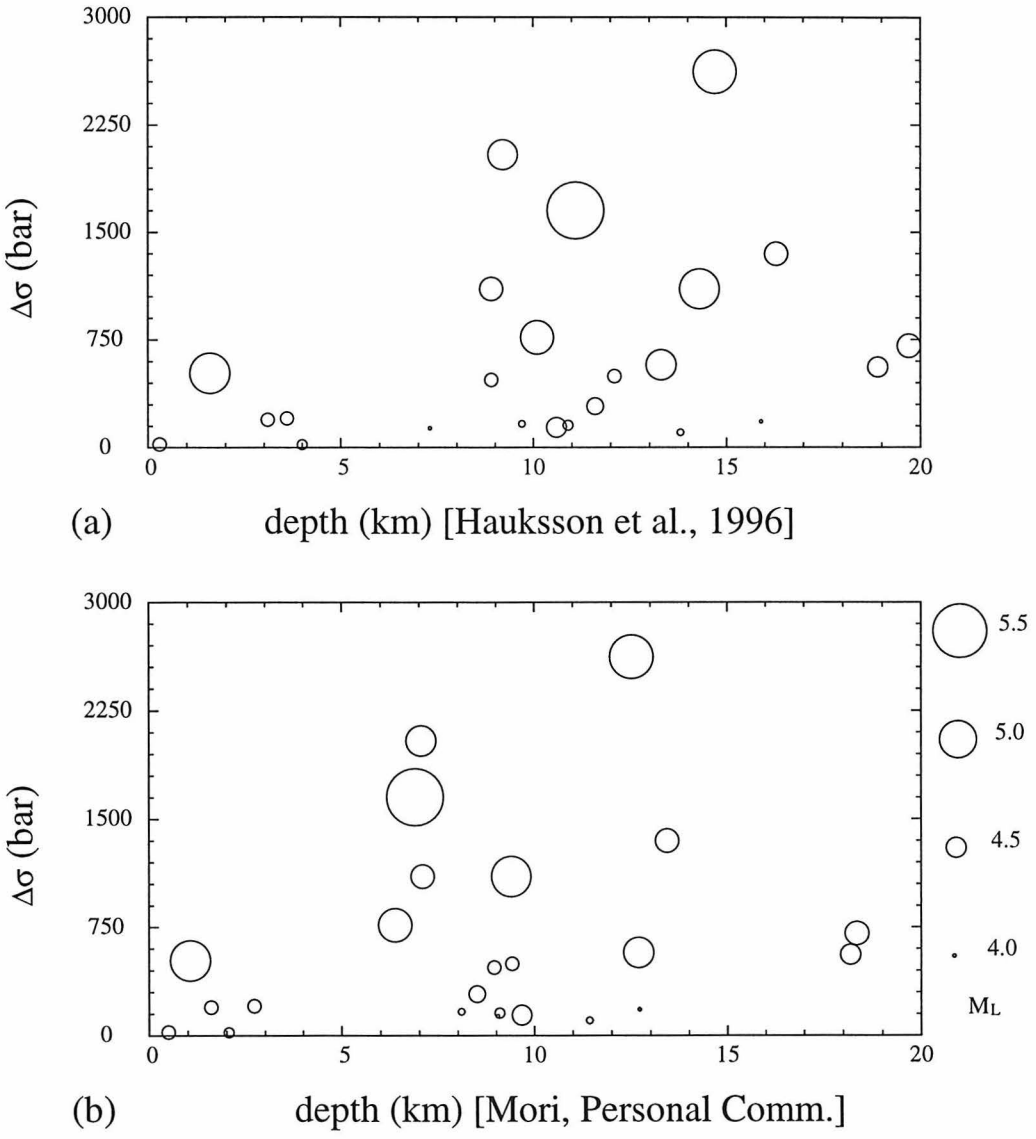

Figure 3.10: Depth distribution of the relative stress drop for the Northridge aftershocks. Symbol size corresponds to M_L.

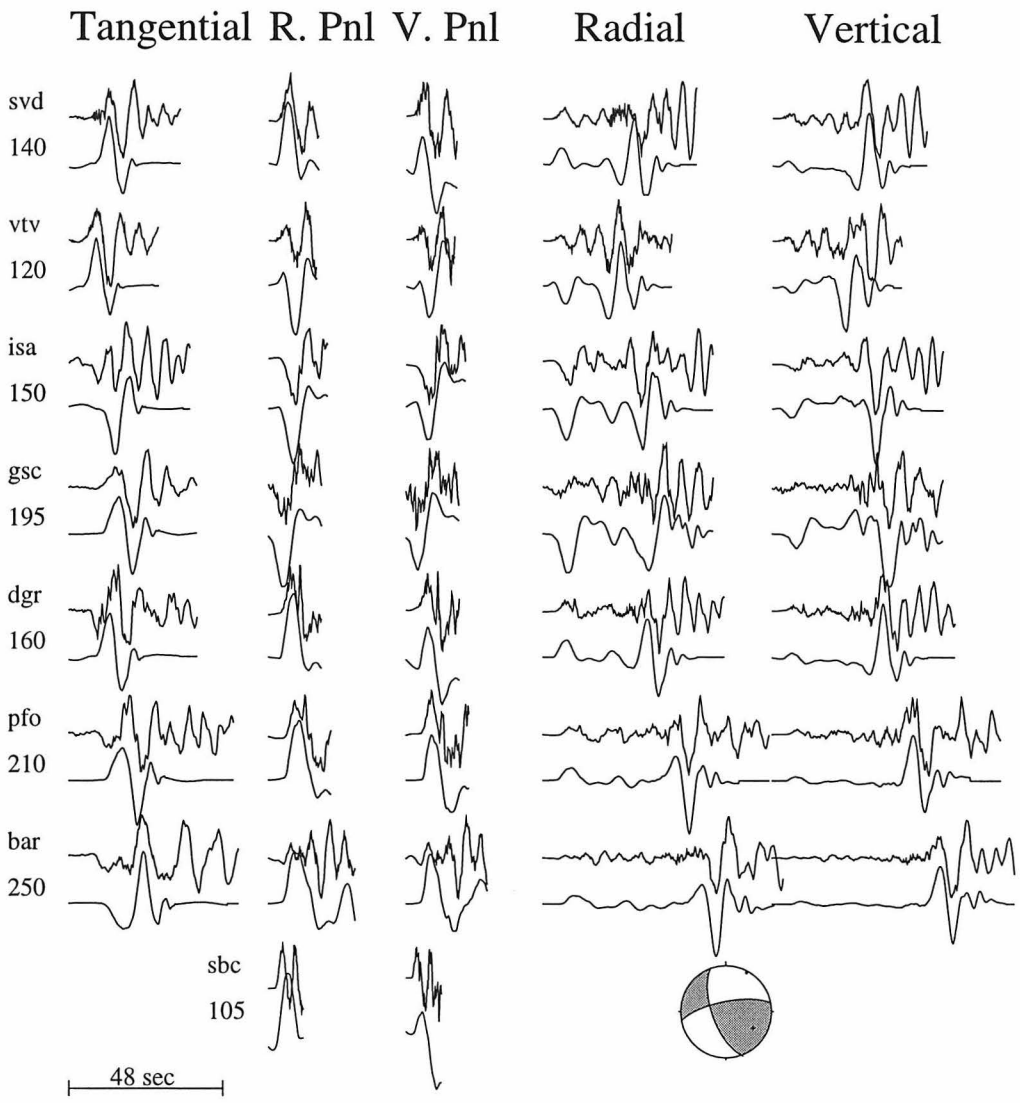

Figure 3.11: Comparison of broadband displacement data (event #1120) and corresponding synthetics for the mechanism displayed with a trapezoidal far-field source-time function (2.5, 1.8, 2.5 sec) and a source depth of 5 km. All seismograms are scaled to unit height. There is a 40% standard variation for the seismic moment.

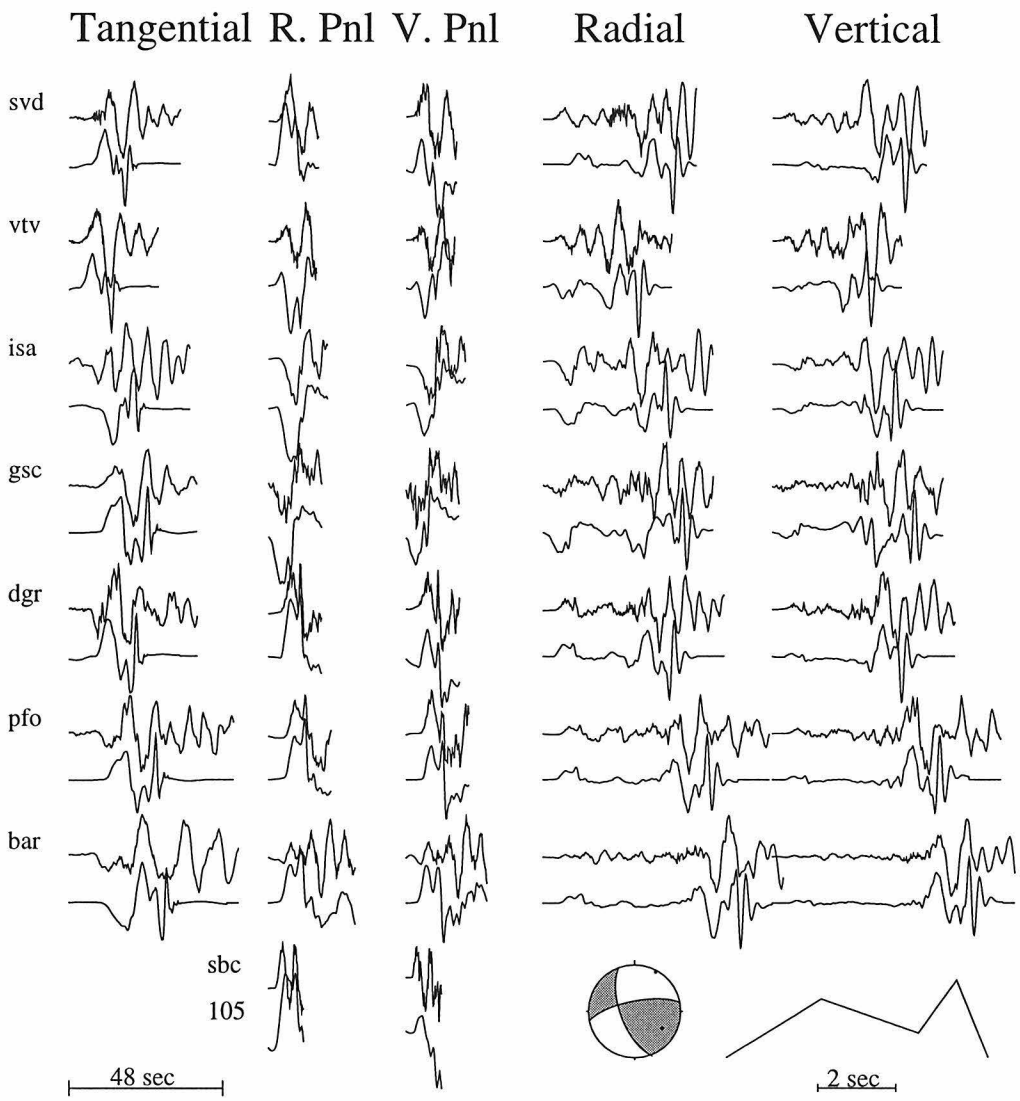

Figure 3.12: Comparison of broadband displacement data (event #1120) and corresponding synthetics for the mechanism displayed with the far-field source-time function as shown in the lower-right corner and with a source depth of 5 km. Note the improvement in the P_{nl} waveform fit (DGR and PFO) after introducing asperity.

procedure discussed earlier. Fundamental Rayleigh waves are fit well, but the P_{nl} wave data are more complicated than the corresponding synthetics. For example, there are obvious secondary pulses in the P_{nl} segment at stations DGR and PFO that do not show up in the synthetics. Note the separation between these two pulses are approximately the same at stations DGR and PFO although the distance to these two stations differ by about 50 km. This suggests a secondary source for this event. In Figure 3.12, we attempt to model this complexity as a double source, with the far-field source-time function shown at the bottom of the figure. Synthetic waveform fits to the P_{nl} data are improved with this complex source model, but fits to the Rayleigh waves are slightly deteriorated, suggesting that the actual rupture process is more complicated than the simple model we have been assuming.

Severe path effects, such as the San Fernando and the Los Angeles basins, also contribute to the complexity of the Northridge data. As an example, we compare the vertical broadband and short-period displacement data and cumulative energy curves for stations GSC and PFO, for 3 earthquakes at different depths (Figure 3.13). These three events occurred under the Santa Susana Mountains within 10 km of each other [*Hauksson et al.*, 1995]. Note the difference in the Rayleigh wave-train between the records at GSC and PFO for the various events. Seismic signal arrives at station GSC in a time window narrower than at station PFO. This difference is also evident on the short-period records (Figure 3.13), but becomes less significant for deeper sources. Scattering due to the more heterogeneous structure from Northridge to PFO could cause this difference. Note that the path from Northridge to station GSC is relatively uniform. The path to PFO traverses the San Fernando basin and part of the Los Angeles basin (Figures 3.1 and 3.8). For a shallow earthquake, part of the surface wave energy is trapped in the basin and propagates through the slow top layer, producing the extended Rayleigh wave-train at station PFO. This could explain the fact that GSC yields a consistently larger seismic moment than does PFO (Figure 3.14), since energy, arriving at PFO along different paths, spread out in a wider time window. Our M_0 estimate is controlled by the amplitude of the first packet of surface wave energy because the synthetics we used do not include the more

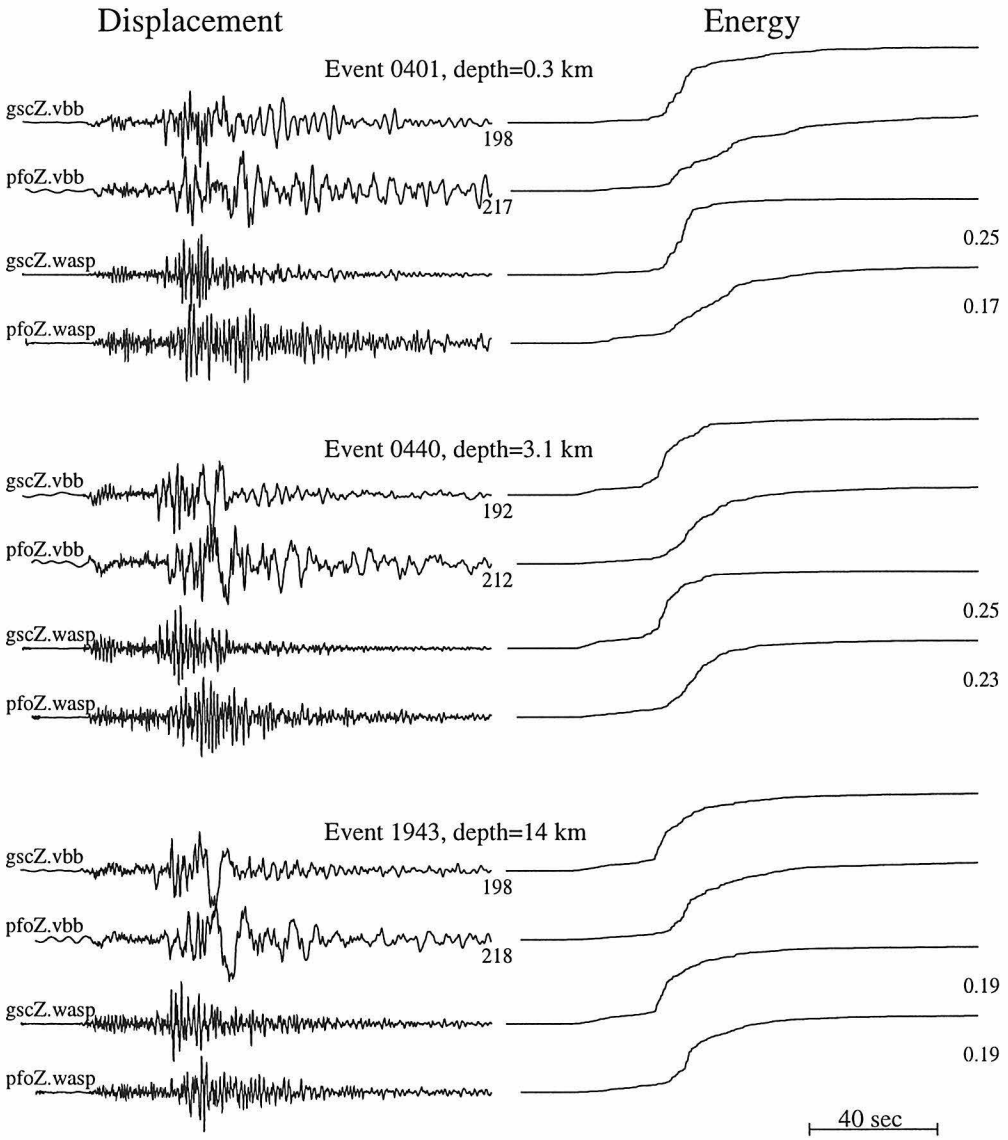

Figure 3.13: Comparison of the broadband and short-period (WASP) vertical displacement data and cumulative energy curves for stations GSC and PFO for 3 Northridge aftershocks at different depths. In the displacement columns, numbers indicate epicentral distances. In the energy column, the short-period to broadband energy ratios are shown for each record. Note the degree of complexity as a function of source depth and station.

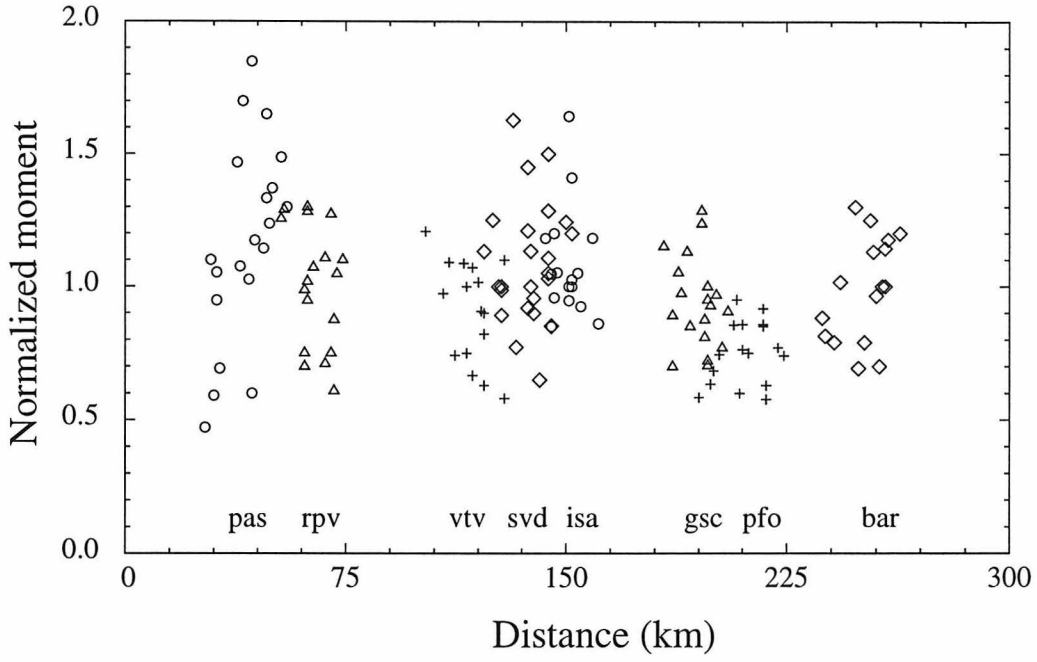

Figure 3.14: Display of single-station moment estimates normalized by the average value over TERRAscope, for the Northridge aftershocks. Note that stations PAS and SVD display the largest scatter. Station GSC yields consistently larger moment than PFO.

dispersed surface wave train. For deep earthquakes, the basin effect is less. However, for the entire group of events, there lacks a clear trend of this complexity with source depth, possibly because of the complex basin structure. To better understand the wave propagation associated with the shallow basins, 2-D finite difference modeling would be helpful, as reported by *Song et al.* [1995b].

Basin effects can also be examined by comparing the ratio of M_e to M_0 for various source depths, averaged over all the network (Figure 3.15). M_e is defined as the square root of the ratio of the total accumulative energy between data and the synthetics computed for unit moment [*Zhao and Helmberger*, 1996]. M_0 is the seismic moment. The M_e/M_0 ratio indicates how much energy is modeled by our 1-D synthetics and how much is not, presumably due to the scattering of energy in certain frequency bands by the basin. If the 1-D synthetics are efficient in modeling the energy radiation from the source, this ratio should be close to 1. Figure 3.15*a* shows the M_e/M_0 ratio

in the low-frequency band (LP3090) with respect to source depth for two groups of events: those that are located under the mountains and those under the basin. Note the average value for the M_e/M_0 ratio is about 1.25, a bias possibly due to the fact that our 1-D model is not soft enough at the top. The event with exceptionally high M_e/M_0 ratio is the complex event (#1120) we discussed above. It occurred near the northwestern edge of the San Fernando basin. Other than this event, there is no obvious depth dependence of the M_e/M_0 ratio. Events under the basin (squares) and those under the mountains (dots) show the same scatter. At short-period, some of the shallow events display high M_e/M_0 ratios (*e.g.*, events #1216, #0401, #1446; Figure 3.15*b*). The scatter is also large, which makes it hard to establish, from this sparse data set, any trend of the M_e/M_0 ratio with respect to the source depth. However, Figure 3.15*b* suggests that, among the squares, this ratio can differ by as much as a factor of 3. If scattering at the basin edge is causing this, we would expect, assuming reciprocity, a similar factor from incoming waves, in the event of a regional earthquake occurring outside the basin.

In summary, we studied the TERRAscope waveform data for a set of Northridge aftershocks. Our source mechanisms agree well with focal plots determined from first-motion P-waves picks from the Southern California Seismic Network (SCSN) [*Hauksson et al.*, 1995]. This result indicates that the longer period motions associated with surface waves are compatible with the initial rupture motions and that the fault plane does not change appreciably over the rupture history. The same conclusion was also reached in our study of the Northridge mainshock [*Song et al.*, 1995a]. Our source depth estimates were determined by the ratio of Rayleigh waves to P_{nl} strengths and generally agree well with *Hauksson et al.* [1995]. Since the SCSN array had temporary near-in data for depth control (S-P times), we conclude that our independent depth estimates have been validated and should be applicable for events in other regions where near-in data is not available. Source duration was estimated by comparing short- to long-period energy ratio in the P_{nl} data, relative to synthetics. This method, originally proposed by *Zhao and Helmberger* [1996], was tested against the more traditional method of measuring the width of direct pulses, and proved to

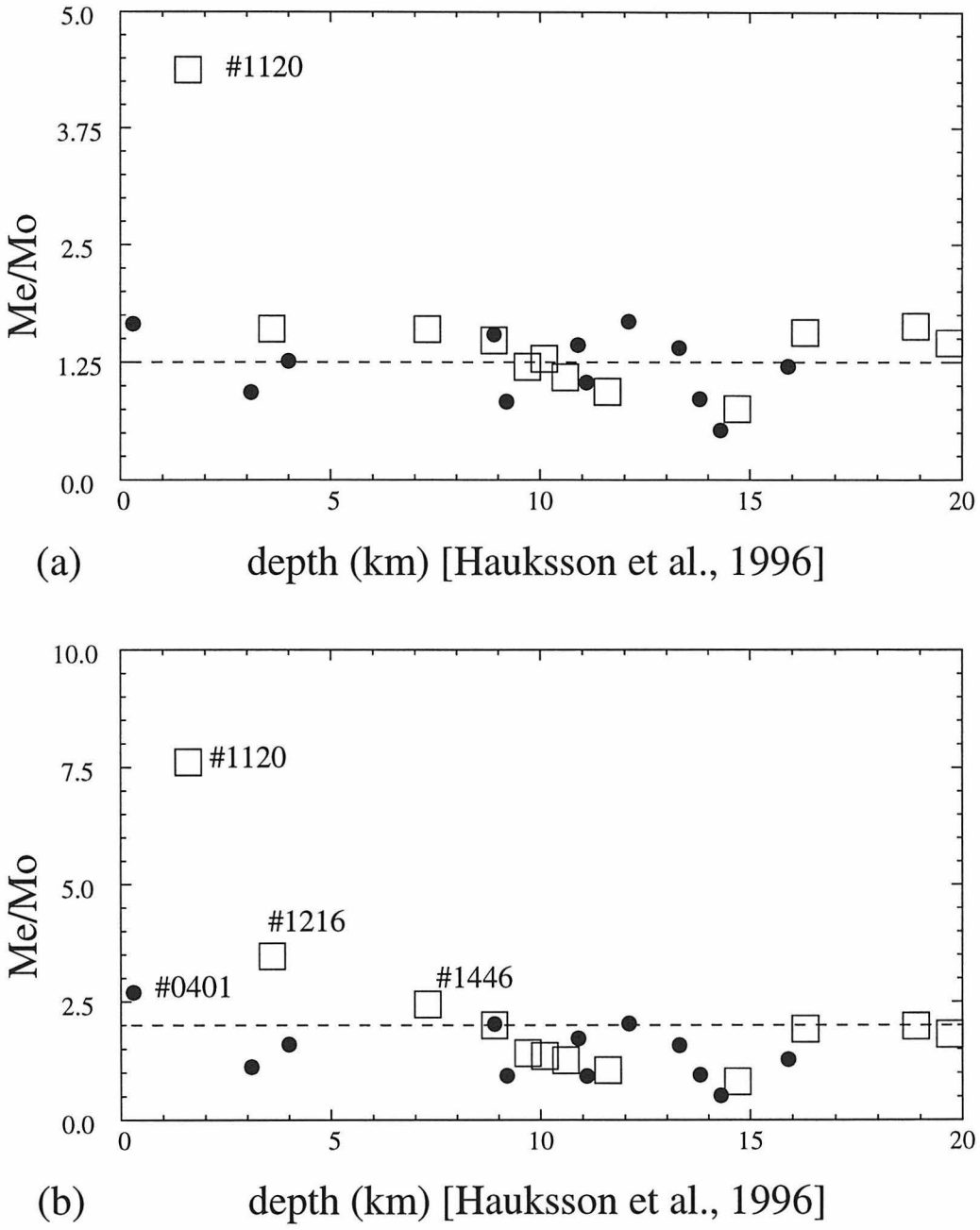

Figure 3.15: M_e/M_0 ratio of Northridge aftershocks with respect to focal depths by *Hauksson et al.* [1995]. (a) in low-frequency band (LP3090). (b) in high-frequency band (WASP). Black dots correspond to events under the mountains. Squares correspond to events under the San Fernando basin. Vertical components at stations BAR, GSC, ISA, PAS, PFO, RPV, SVD, and VTV are used to calculate M_e.

be an effective means of modeling broadband seismograms and providing consistent source duration estimates. Stress drop of the aftershocks were calculated using these estimates and their depth distribution indicates a zone of high relative stress drop at the depth range of 5 to 15 km, with the larger events yielding the highest stress drops.

Acknowledgements

We thank the Data Center of the Southern California Earthquake Center for making the Northridge data set available. Katrin Hafner helped us in retrieving these data. Craig Scrivner, Andy Michael, Jeroen Ritsema and Lind Gee provided critical reviews along with very helpful suggestions. This research was supported by SCEC under the contract #569933, as funded by NSF #89-20136 and USGS #1434-93-G-2322. Contribution No. 5653, Division of Geological and Planetary Sciences, California Institute of Technology, Pasadena, California.

Chapter 4 Source characteristics of the January 17, 1994 Northridge, California earthquake from regional broadband modeling

4.1 Abstract

Broadband regional records are modeled to determine source mechanism, seismic moment, fault dimension and rupture directivity for the January 17, 1994 Northridge Earthquake. Modeling is done using both theoretical Green's functions (tGf) and empirical Green's functions (eGf). From the theoretical modeling, we obtain a source mechanism with strike 128^o, dip 33^o and rake 106^o for the mainshock, using a source estimation algorithm by *Zhao and Helmberger* [1994]. While the fault orientation seems resolvable from regional data, the moment estimation is less reliable due to inadequate synthetic waveform fits to the observed surface waves. This appears to be caused by the combination of propagational effects and fault complexities. Further investigation of the source characteristics is carried out with a new method of using eGfs. As an eGf, we select the January 17, 1994 17:56 GMT aftershock, which occurred near the onset of the mainshock and had a similar source mechanism. The source duration of the mainshock, as seen from the regional surface waves observed at various stations, is obtained by searching for the trapezoidal far-field source-time function for each station which, when convolved with the aftershock data, best simulates the mainshock data. Stations to the north see shorter source durations than stations to the south. Modeling these with theoretical predictions of rupture on a square fault, we constrain the effective fault dimension to be 14 km with rupture

along the direction of the average rake vector. A moment of $(1.4 \pm 0.9) \times 10^{26}$ dyne·cm with a stress drop of $\sim$120 bars is obtained for the mainshock from our eGf study.

4.2 Introduction

Recent advances in seismic acquisition are making it possible to rapidly estimate source parameters of significant earthquakes. Typical questions asked by seismologists after a large event such as the Northridge Earthquake are: (1) Where did it occur and how large was it? (2) What were its fault parameters? (3) Which plane ruptured and in what direction? (4) Would we expect to see surface breakage? Currently, the first two questions are answered by modern seismic arrays shortly after the earthquake. Answering the remaining questions often requires further study. For the Northridge Earthquake, however, work was complicated both by propagational effects introduced by the San Fernando basin, and by the loss of a critical TERRAscope station (ISA) to the north (Figure 4.1). Loss of records from station ISA made necessary the use of records from stations farther to the north, at much greater epicentral distances than those used in previous modeling studies in Southern California [*e.g. Dreger and Helmberger*, 1991a]. Thus, given the relatively long, structurally complex paths connecting Northridge to the three distant stations (PKD1, CMB and MLA), we chose to augment our theoretical modeling with an eGf study.

The eGf study was further motivated by the azimuthal variation in absolute timing of the mainshock relative to a nearby aftershock of similar depth and source mechanism. Broadband waveform comparisons of the main event and this aftershock are shown in Figure 4.2. The seismograms recorded at stations to the north of both events are very similar in shape and timing, though their amplitudes are different by three orders of magnitude. In contrast, the Rayleigh waves from the mainshock are considerably delayed relative to the aftershock at stations to the south (*i.e.*, BAR). This observation motivates further investigation of rupture directivity.

Based on the above considerations, we address three issues. First, we establish faulting parameters using only the body waves. They should be less influenced by

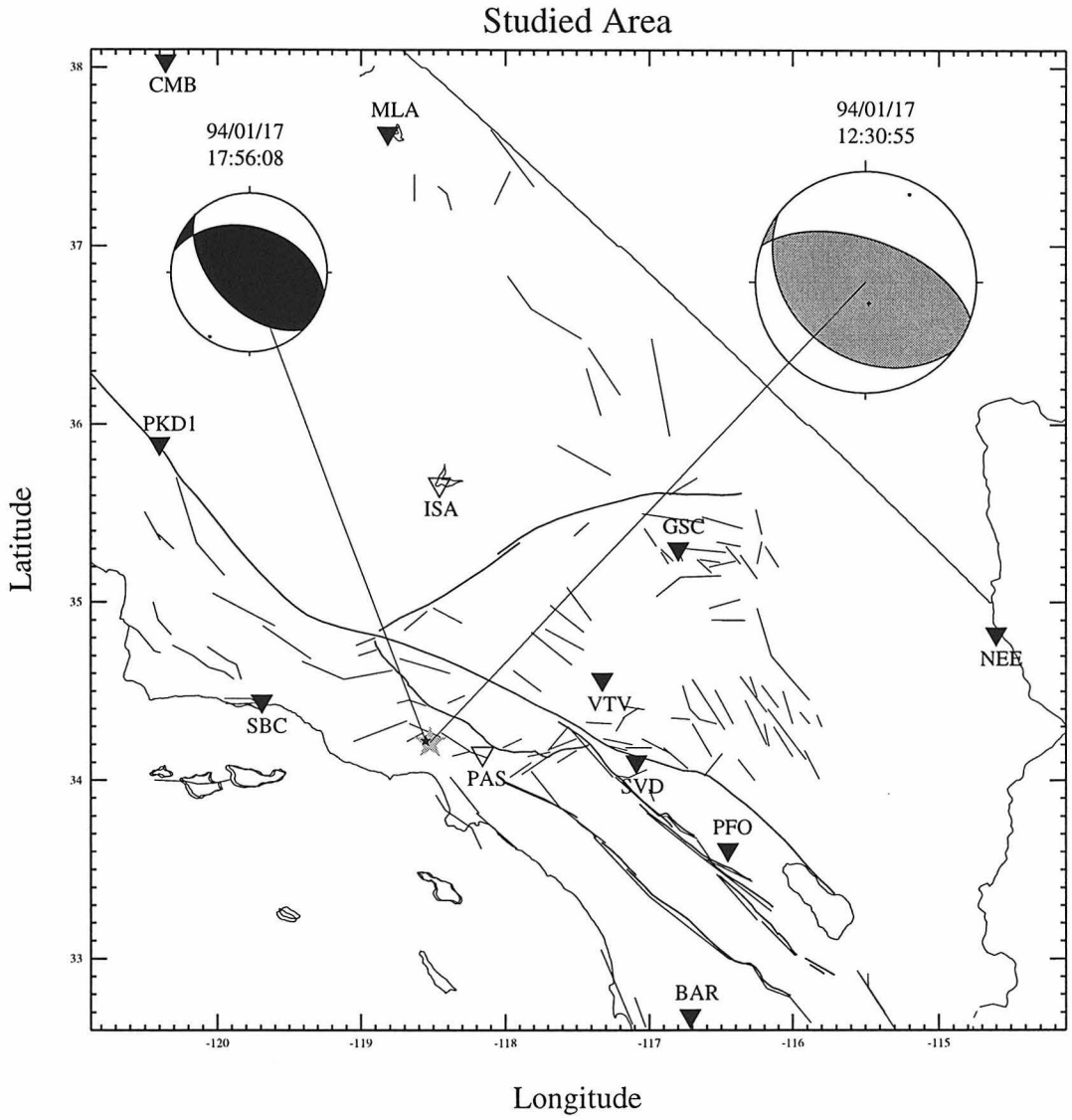

Figure 4.1: Some of the broadband stations (triangles) in Southern California and the epicenters of the mainshock (gray star) and the aftershock (dark star). Stations used in this study are shown with solid triangles. Also shown are the origin times and our preferred double-couple source mechanisms for the two earthquakes.

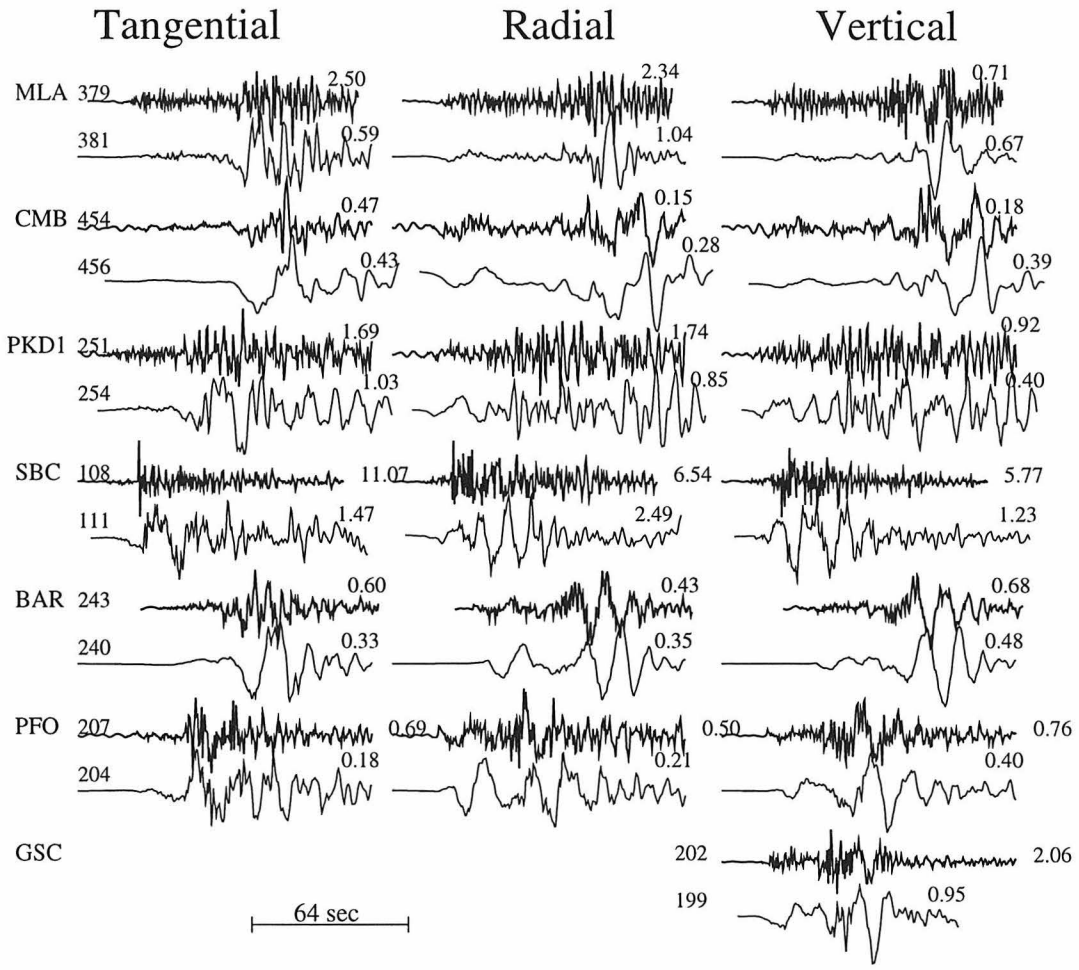

Figure 4.2: Comparison of the broadband displacement records between the Northridge mainshock (light traces) and the aftershock (heavy traces). Seismograms in each pair are aligned in absolute travel time. Station names, distances (km) and peak amplitudes (cm for the mainshock and 10^{-3} cm for the aftershock) are also shown.

Data used	Focal depth assumed (km)	Strike (^{0})	Dip (^{0})	Rake (^{0})	Moment (10^{25} dyne·cm)
P_{nl}	11	132	35	113	9.4
P_{nl}	15	128	33	106	10.
P_{nl}	19	126	28	99	13.
Whole	15	128	33	106	8.1

Table 4.1: Estimated source parameters of the mainshock. Our best moment estimate is $(1.4 \pm 0.9) \times 10^{26}$ *dyne-cm* from the eGf study.

basin effects, compared to the surface waves. Second, we model complete displacement records of the 17:56 GMT aftershock (Figure 4.1) and the mainshock using theoretical Green's functions. Finally, as the main purpose of this paper, we examine fault dimension and rupture directivity and estimate the seismic moment of the main event, using the waveforms from the 17:56 GMT aftershock as empirical Green's functions.

4.3 Source estimation with theoretical Green's functions

We first estimate the mainshock source parameters using a grid-search source estimation algorithm due to *Zhao and Helmberger* [1994]. This method selects the source mechanism which minimizes the L1 and L2 norms between the data and synthetics and often produces a stable solution from a relatively sparse data set. For this procedure, we use broadband displacement records from five TERRAscope stations (BAR, GSC, MLA, PFO, SBC) and two BDSN stations (CMB, PKD1) (Figure 4.1). The source is modeled with a point double-couple with a trapezoidal far-field source-time function (1.5 sec, 1.5 sec, 1.5 sec). The standard Southern California crustal model (SC) [*Dreger and Helmberger*, 1991a] is used for most of the stations except the station NEE, for which we use a model developed for the Basin and Range province by *Song et al.* [1996]. Synthetic seismograms are generated by a frequency-wavenumber matrix propagation algorithm [*Saikia*, 1994a].

Source estimation is done in two steps. In the first step, only the P_{nl} waves

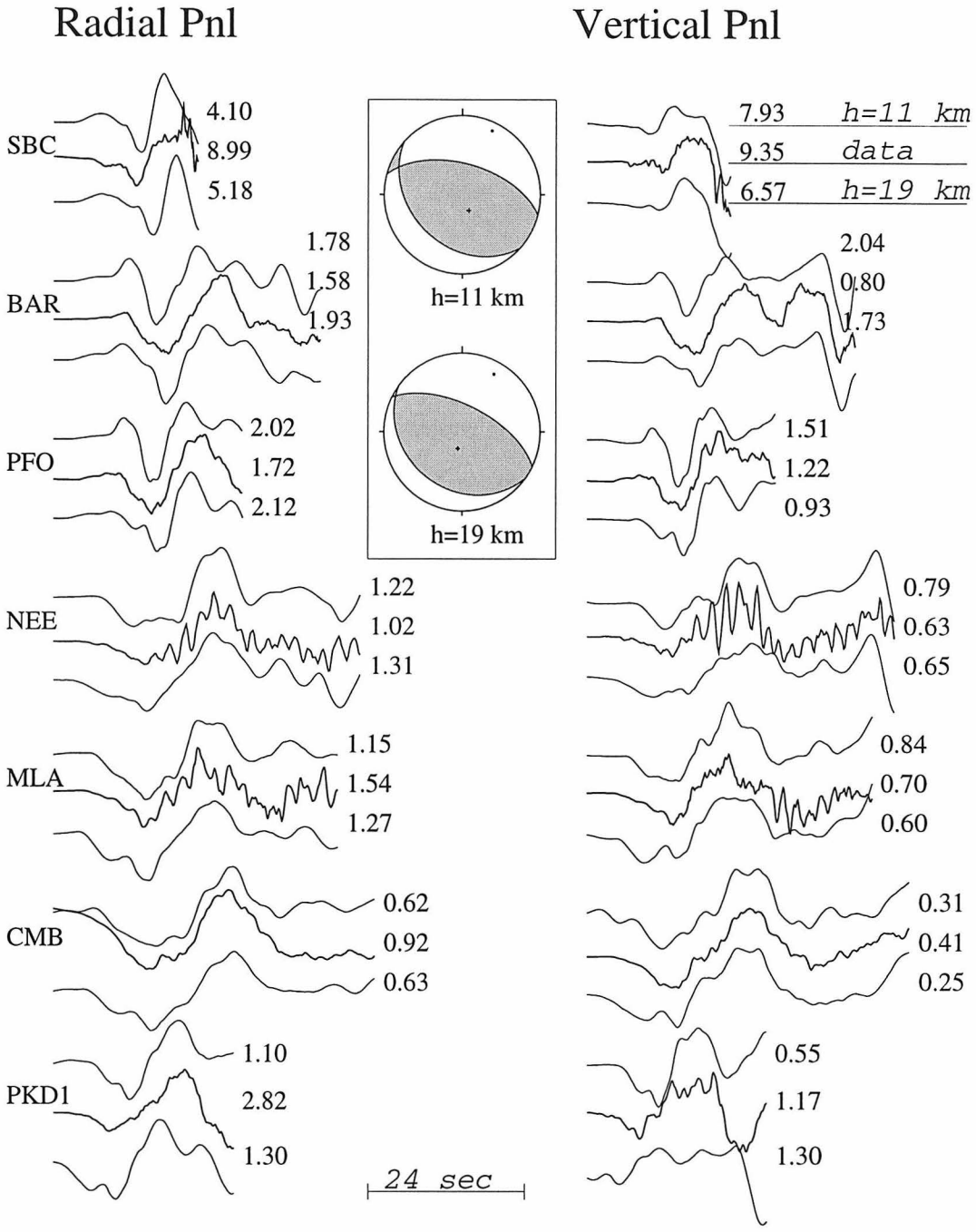

Figure 4.3: Comparison of broadband displacement data (mainshock, P_{nl} only) and the corresponding synthetic waveforms. The middle heavy traces are data. Top traces are synthetics assuming a source depth of 11 km and bottom traces are synthetics for a source depth of 19 km. Peak amplitudes (mm) are shown above each trace, given the appropriate seismic moment (Table 1) for the synthetics. The source mechanism solutions for the two source depths are also shown.

recorded at the above stations are used in the process and we cycle through different source depths (11, 15, and 19 km). Estimated source parameters for different focal depths are presented in Table 4.1. Figure 4.3 compares the P_{nl} portion of the broadband data and synthetics for source depths of 11 and 19 km. The source mechanisms obtained are also shown. The fits between data and synthetics are generally good, with small differences between fits for each depth. The source parameters for the three depths are very similar. These are probably because the source propagation spans a substantial depth range. However, fits between the data and synthetics for a source depth of 19 km are better than those for a source depth of 11 km, especially near the onset of the P_{nl} waves at stations PFO and BAR (Figure 4.3). This suggests that the source was deep, or at least the rupture began at a depth closer to 19 km than 11 km. The average depth is near 15 km according to the above criteria used in this estimation technique and the fits between the P_{nl} data and the corresponding synthetics for a source depth of 15 km appear to be the best in an average sense among the three depths tested (Figures 4.3 and 4.4). In the second step, we fix the depth at 15 km and add in surface waves in the estimation procedure. Figure 4.4 shows the comparison between the broadband data and the corresponding synthetics for the mechanism obtained in the whole waveform source estimation. At most of the stations, the P_{nl} waves and the surface waves are both modeled reasonably well. This estimation was done to see if the surface waves require the same source orientation as the P_{nl} waves, since the surface waves should be more sensitive to the shallow structure. That is, if the mechanism changed dramatically during the rupture, we might expect to get a different source mechanism by including surface waves in the estimation. However, addition of the surface waves to the P_{nl} waves in the procedure produces the same mechanism as that obtained with the P_{nl} waves alone (Table 4.1). This feature makes the eGf study in the next section reasonable, since apparently only one fault plane was involved. The seismic moment obtained from the whole waveform estimation is smaller than that obtained using the P_{nl} waveforms alone. This again suggests that a substantial portion of the earthquake energy was released deeper than 15 km.

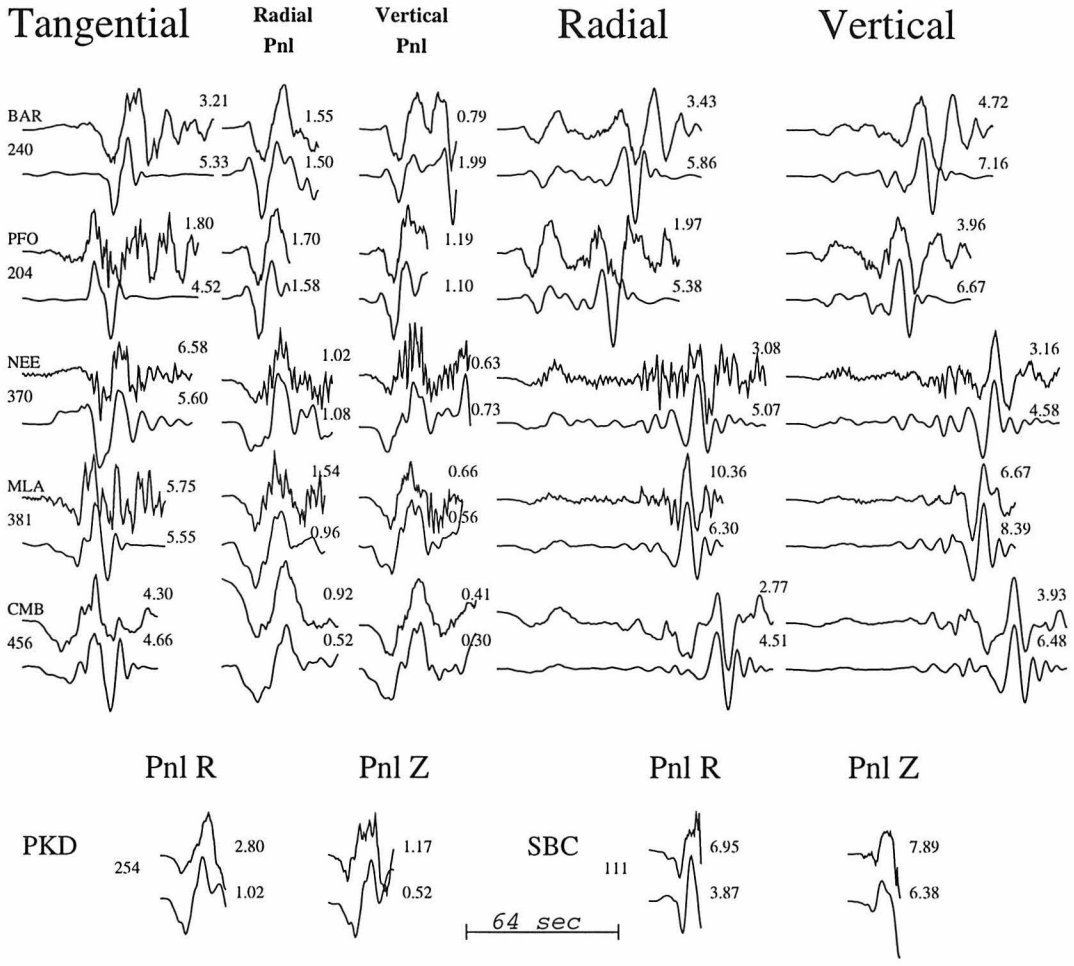

Figure 4.4: Comparisons of broadband displacement data (mainshock, whole waveform; top traces) and the corresponding synthetic waveforms (bottom traces) assuming a source depth of 15 km. Source estimation with P_{nl} waves only and that with the whole waveform yield about the same mechanism. Peak amplitudes (mm) are given above each trace, given a seismic moment of 8.1×10^{25} dyne·cm for the synthetics.

Some attention needs to be paid to the far-field source-time function. The (1.5 sec, 1.5 sec, 1.5sec) trapezoid seems to work well for the P_{nl} waves, as is seen in the synthetic waveforms in Figures 4.3 and 4.4. For surface waves shown in Figure 4.4, however, the synthetics are shorter-period than the data by a factor of 2, especially at stations BAR and PFO to the south. This is not unexpected since the slowly travelling surface waves should see a longer source duration for a propagating source. We address the issue of source propagation in the next section, with an eGf study.

Ideally, an event used as an eGf should be at the same location and have the same source mechanism as the event being investigated, to ensure that both earthquakes have similar source and propagational effects. To this end, we select the January 17, 1994 17:56 GMT aftershock as an eGf for our study. This small event occurred within 5 km of the mainshock, at the location (118.57W, 34.22N), and at a depth of roughly 17-20 km [*Thio and Kanamori*, 1996; *Hauksson et al.*, 1995].

A source mechanism was obtained for this aftershock using the same source estimation procedure and broadband records convolved with a long-period Press-Ewing (LP3090) instrument response. The convolution was necessary due to the large high-frequency component in the records, which could otherwise have been difficult to model. This also desensitizes our moment estimation to the attenuation factors in the crustal model used for the tGfs and reduces the related uncertainty. Our modeling analysis indicates that this small event has a very short source duration no broader than 0.4 sec. Source estimation at long-period with different depths (14, 17 and 20 km) yields about the same source mechanism. Figure 4.5 shows the comparison of broadband records (aftershock) convolved with a LP3090 response, and appropriate synthetics for the depth of 17 km. The source mechanism obtained for the aftershock (strike 120^0, dip 42^0, rake 100^0) is quite similar to that of the mainshock. The seismic moment obtained is $(6.8 \pm 2.5) \times 10^{22}$ dyne·cm. The uncertainty in the moment estimation reflects the scattering in the peak amplitude ratio between the data and the synthetic waveforms. It does not include that introduced by the uncertainty in assuming the crustal model (SC), mainly in the receiver functions at various stations, which may cause an error of up to 20% in the moment estimation. The latter is due

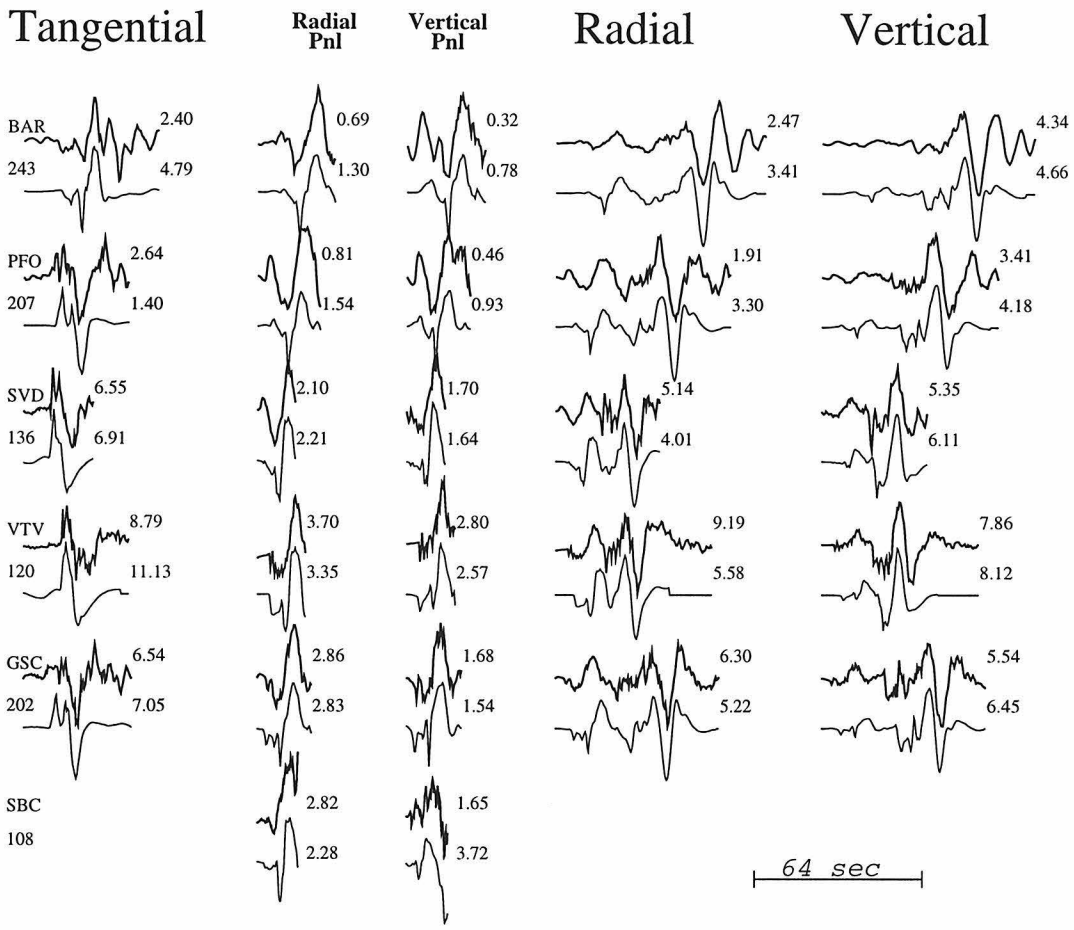

Figure 4.5: Comparisons of broadband displacement data (top traces), convolved with a long-period Press-Ewing instrument response, and the corresponding synthetic waveforms (bottom traces) for the aftershock, assuming a source depth of 17 km. Peak amplitudes (10^{-3} mm) are given above each trace, given a moment $M_o = 6.8 \times 10^{22}$ dyne·cm for the synthetics.

to the fact that one could usually model the surface waves with the velocities of the surface layer varying by 20%, given the appropriate velocity-thickness trade-off [*e.g. Song et al.*, 1996]. Taking this into account, we estimate the aftershock moment to be $(6.8 \pm 3.9) \times 10^{22}$ dyne·cm. We address later how the first part of the uncertainty might be reduced.

4.4 Source characteristics from eGf modeling

The main event is larger in moment than the aftershock by three orders of magnitude, but the waveform comparisons in Figure 4.2 show some similarities in wave shape. However, there are lags in absolute timing between the waveforms of the aftershock and of the main event. While time lags at stations to the north (*i.e.,* CMB and MLA) are small, those at stations to the south (*i.e.,* BAR, PFO) are comparatively large. These are indications of mainshock source directivity. As discussed above, the aftershock has a very short duration and a mechanism and location very similar to those of the main event. It is thus an appropriate eGf for use in a study of the mainshock source characteristics.

However, there are some assumptions that need to be explained in the present use of empirical Green's functions. We can express the displacement of the aftershock as

$$S_A(t,\vec{r}) = G(t,\vec{r},\vec{\xi},\tau) * \delta(\tau-\tau_a) * \delta(\vec{\xi}-\vec{\xi}_a) * [M_a s_a(t)] = G(t,\vec{r},\vec{\xi}_a,\tau_a) * [M_a s_a(t)], \quad (4.1)$$

where $G(t,\vec{r},\vec{\xi},\tau)$ is the propagational Green's function, or the far-field displacement due to a point-source of step dislocation with unit moment at time τ and source position vector $\vec{\xi}$. The Green's function has a dimension of $\frac{length}{energy}$. $s_a(t)$ is the far-field source-time function of the aftershock. It is normalized to unit area and has a dimension of $\frac{1}{time}$. M_a is the seismic moment of the aftershock.

Suppose the main event is represented by a cluster of point-sources of step dislocation in the source region, each with a moment $m(\vec{\xi})dA$, where dA is the infinitesimal

area. The displacement produced by each point-source, $(\vec{\xi}_s, \tau_s)$, is

$$S_s(t, \vec{r}) = G(t, \vec{r}, \vec{\xi}_s, \tau_s) * [m(\vec{\xi}_s) dA\, \delta(t)]. \tag{4.2}$$

Note that τ_s is related to $\vec{\xi}_s$ through the rupture velocity vector. Using the reciprocal relation for source and receiver times [*Aki and Richards*, 1980], we can rewrite $S_s(t, \vec{r})$ as

$$S_s(t, \vec{r}) = G(t, \vec{r}, \vec{\xi}_s, \tau_a) * \left[m(\vec{\xi}_s) dA\, \delta\left(t - \Delta t(\vec{\xi}_s)\right)\right], \tag{4.3}$$

where $\Delta t(\vec{\xi}_s) = (\tau_s - \tau_a)$ is a function of $\vec{\xi}_s$.

The main event displacement is the sum of displacement of all the point-sources

$$S_M(t, \vec{r}) = \int\!\!\int_A S_s(t, \vec{r}) = \int\!\!\int_A G(t, \vec{r}, \vec{\xi}_s, \tau_a) * \left[m(\vec{\xi}_s)\, \delta\left(t - \Delta t(\vec{\xi}_s)\right)\right] dA. \tag{4.4}$$

For small enough source dimension, we can assume

$$G(t, \vec{r}, \vec{\xi}_s, \tau_a) = F(\vec{\xi}_s - \vec{\xi}_a) G(t, \vec{r}, \vec{\xi}_a, \tau_a) * \delta(t - \Delta t'(\vec{\xi}_s - \vec{\xi}_a, \vec{r})). \tag{4.5}$$

That is, the difference in the Green's function due to the spatial separation between a point-source of the main event and the aftershock can be represented by a time delay $\Delta t'(\vec{\xi}_s - \vec{\xi}_a, \vec{r})$ and a scale factor $F(\vec{\xi}_s - \vec{\xi}_a)$. Note, however, that this approximation would be more appropriate if we use a particular correction for each arrival based on its phase velocity. Fortunately, it is the surface waves that dominate the records, which have predictable phase velocities. Moreover, surface waves are relatively long period and their waveforms are less affected by small source mislocation. Thus, this assumption is justified for surface waves. The scale factor $F(\vec{\xi}_s - \vec{\xi}_a)$ is due to the difference in source depth between the point-source of the main event and the aftershock and should be determined by the amplitude ratio of their surface waves. For simplicity, we can approximate $F(\vec{\xi}_s - \vec{\xi}_a)$ by its value at the center of the rupture segment, $F(\vec{\xi}_c - \vec{\xi}_a)$.

Since $G(t, \vec{r}, \vec{\xi}_a, \tau_a)$ is independent of $\vec{\xi}_s$, we are now able to rewrite equation (4) by

convolving both sides with $s_a(t)$ (Recall that $s_a(t)$ is the far-field source-time function of the aftershock)

$$S_M(t,\vec{r}) * s_a(t) = G(t,\vec{r},\vec{\xi}_a,\tau_a) * [M_a s_a(t)] * \frac{F(\vec{\xi}_c-\vec{\xi}_a)}{M_a}$$

$$\cdot \int\!\!\int_A \delta\left(t-\Delta t'(\vec{\xi}_s-\vec{\xi}_a,\vec{r})\right) * \left[m(\vec{\xi}_s)\delta\left(t-\Delta t(\vec{\xi}_s-\vec{\xi}_a)\right)\right] dA. \tag{4.6}$$

Using equation (1), we have

$$S_M(t,\vec{r}) * s_a(t) = \frac{F(\vec{\xi}_c-\vec{\xi}_a)S_A(t,\vec{r})}{M_a} * \int\!\!\int_A m(\vec{\xi}_s)\,\delta\left(t-\Delta t''(\vec{\xi}_s-\vec{\xi}_a,\vec{r})\right) dA. \tag{4.7}$$

where $\Delta t''(\vec{\xi}_s-\vec{\xi}_a,\vec{r}) = \Delta t'(\vec{\xi}_s-\vec{\xi}_a,\vec{r}) + \Delta t(\vec{\xi}_s)$. Assuming $s_a(t) = \delta(t)$, or the aftershock is small enough, this expression can be written as

$$S_M(t,\vec{r}) = \left(F(\vec{\xi}_c-\vec{\xi}_a)\,\frac{M_m}{M_a}\right)\, S_A(t,\vec{r}) * s_m(t,\vec{r}), \tag{4.8}$$

with M_m the seismic moment of the main event and $s_m(t,\vec{r})$ its far-field source-time function at a particular station:

$$s_m(t,\vec{r}) = \frac{1}{M_m}\int\!\!\int_A m(\vec{\xi}_s)\,\delta\left(t-\Delta t''(\vec{\xi}_s-\vec{\xi}_a,\vec{r})\right) dA. \tag{4.9}$$

If we further assume uniform rupture, $m(\vec{\xi}_s) = \frac{M_m}{A}$, we obtain

$$s_m(t,\vec{r}) = \frac{1}{A}\int\!\!\int_A \delta\left(t-\Delta t''(\vec{\xi}_s-\vec{\xi}_a,\vec{r})\right) dA. \tag{4.10}$$

This expression reduces to a unit-area trapezoidal function if we simulate the rupture with a line of point sources sweeping through a rectangular fault plane (Figure 4.6), as demonstrated by *Langston* [1978]. Parameters of the trapezoid for a certain station depend on the fault dimension and the rupture velocity and direction, or just two parameters, the fault dimension and the rupture direction, assuming a square fault and a rupture velocity.

To obtain the appropriate trapezoids for each station, we search through a set of

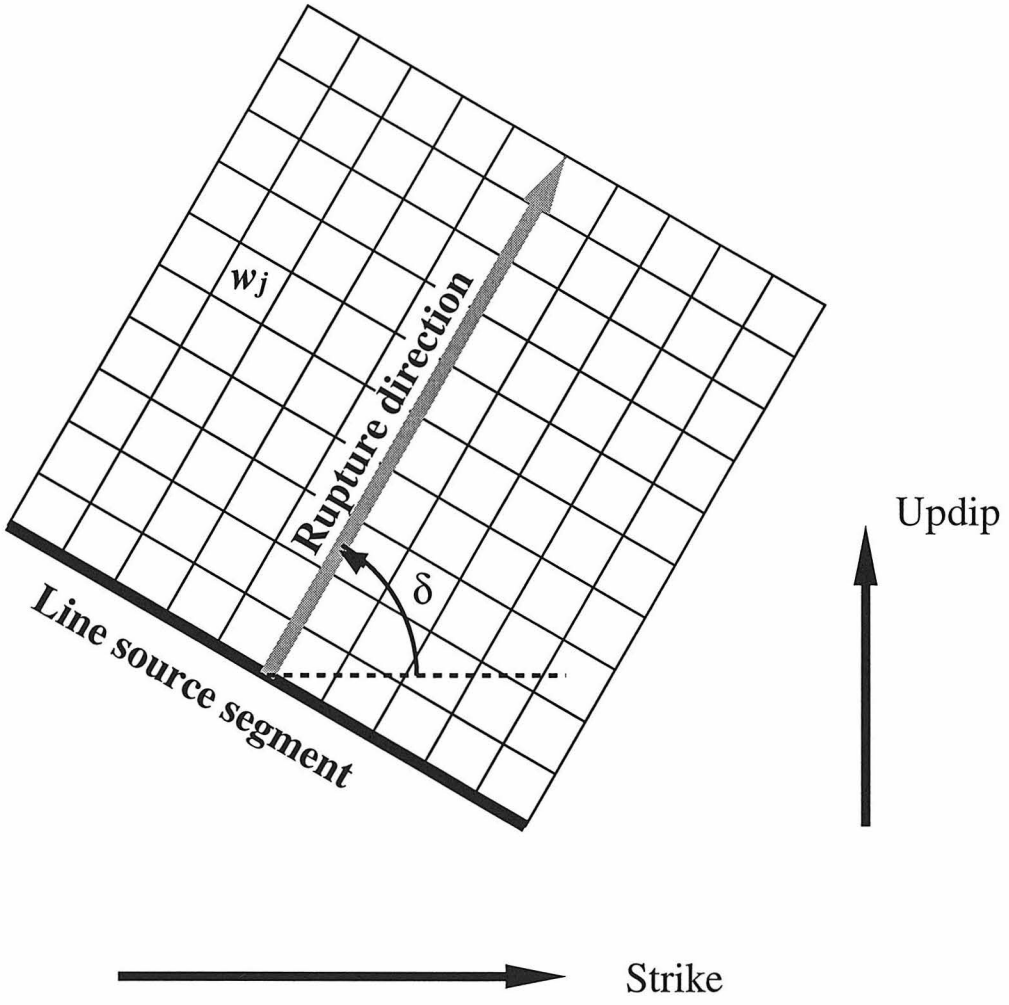

Figure 4.6: Map view of a discretized fault. Rupture is simulated by a line source segment propagating perpendicular to itself. The rupture angle δ, relative to the fault strike, is defined here to specify the rupture direction. When calculating the synthetic seismograms, each element of the fault is represented by a point-source with a weighting factor w_j. $w_j = 1$ is used in this study.

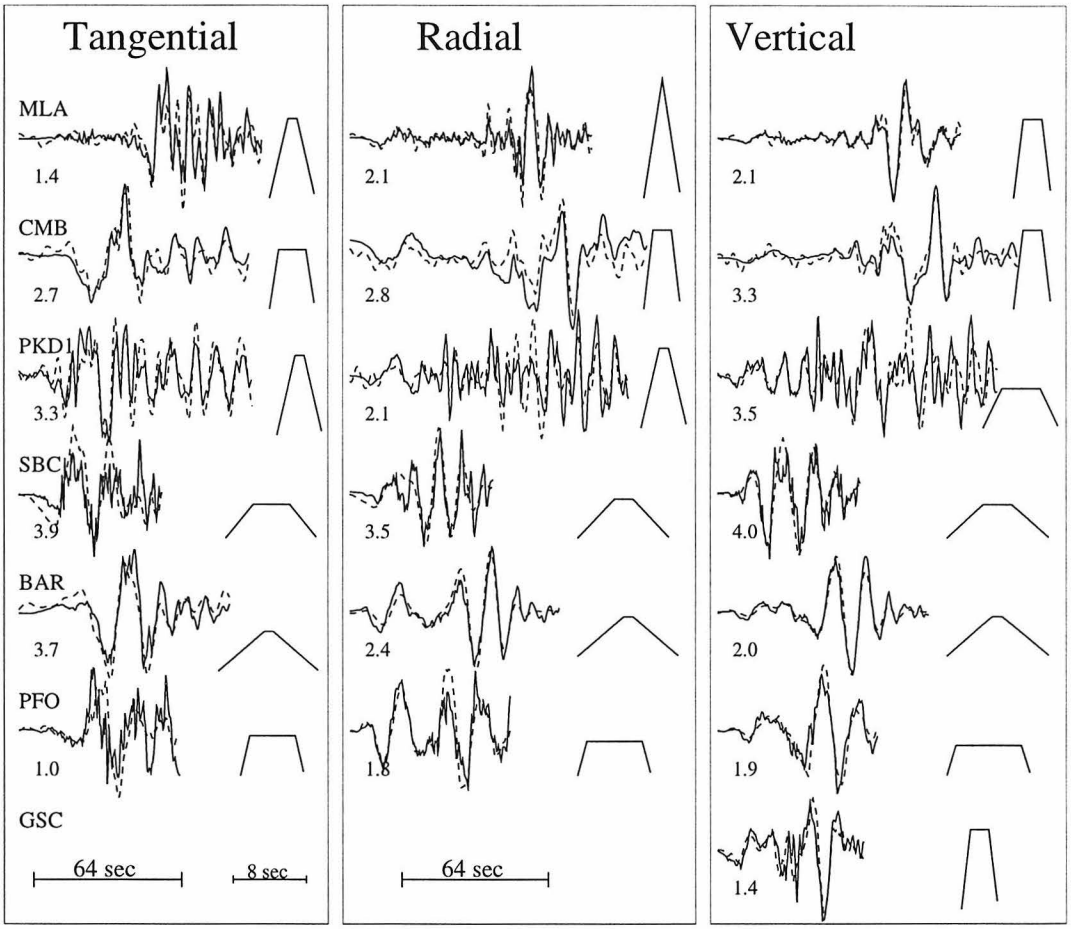

Figure 4.7: Comparison of displacement data (solid traces) from the Northridge mainshock and the corresponding empirical simulations (dashed traces). Each pair of seismograms are aligned in absolute travel time. Also plotted are the trapezoidal far-field source-time functions used for each station, as determined by our method. The small number (in thousands) indicates, for each component, the amplitude ratio of the mainshock data to the simulation.

unit-area trapezoids and convolve the aftershock data with each tested trapezoidal function to simulate the mainshock data for each component. We then compare the simulations with the data to select the most appropriate trapezoid for that component. A criterion based on the averaged L1 and L2 norm [*Zhao and Helmberger*, 1994] is used for this purpose. Figure 4.7 shows comparison between the mainshock displacement data and results from the convolution. At most of the stations (*i.e.,* MLA, CMB, BAR and GSC vertical), the empirical simulations fit the mainshock data very well, with especially good fits to the Rayleigh waves. However, some of the Love wave complexity at short periods is not as well-modeled, most notably at stations SBC and PFO, which will be discussed later.

The duration of the trapezoids required for the best simulation (Figure 4.7) varies azimuthally from station to station, with narrow trapezoids required for stations to the north and broader trapezoids required for stations to the south. To explain this azimuthal variation, we average the trapezoid duration for three components at each station and model the duration as a function of azimuth with Langston's [1978] formulation. In this procedure, we assumed rupture on a square fault with a rupture velocity of 3 km/sec. We also assumed a Rayleigh wave velocity of 3 km/sec and a Love wave velocity of 3.1 km/sec as obtained from the surface wave synthetics (SC model). With these, we obtained a fault dimension of 14 km. Figure 4.8 shows the comparison between the observed trapezoid duration and the calculated duration for rupture in three different directions on a square fault of the above dimension. Among these predictions, $\delta = 106^o$ gives the best fit to the azimuthal variation of the source duration, indicating rupture along the direction of the average rake vector.

Figure 4.9 displays the eGf simulation to the mainshock data using the predicted trapezoids for each station by the uniform rupture model with $\delta = 106^o$. The agreement with the observed waveforms is about as good as in Figure 4.7. This result suggests that the fault dimension and the rupture direction are the most important variables and can be easily estimated following the above procedure. Such a procedure might be automated and used in routine processing of broadband array data.

Better fits to the observed far-field source-time functions can be obtained by al-

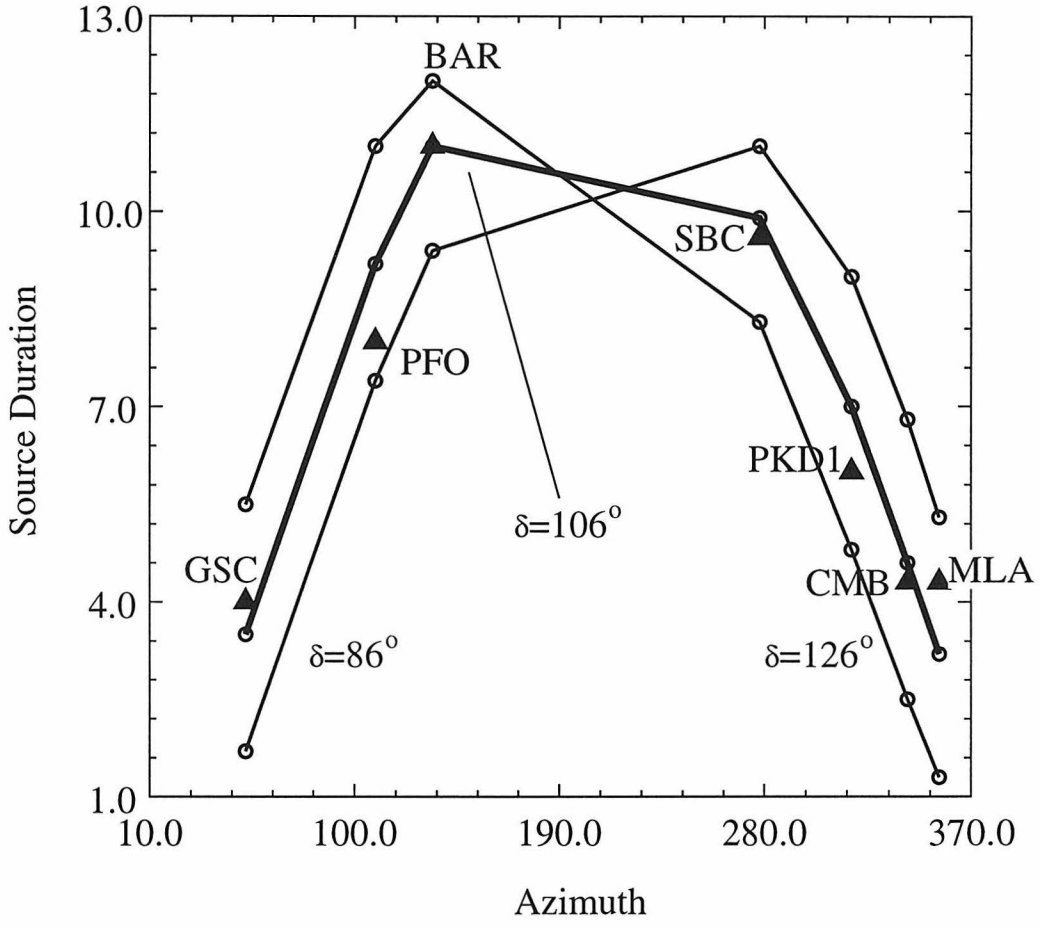

Figure 4.8: Comparison of the observed trapezoid width (triangles) for each station and the predicted width (circles) with $\delta = 86^o$, 106^o, and 126^o.

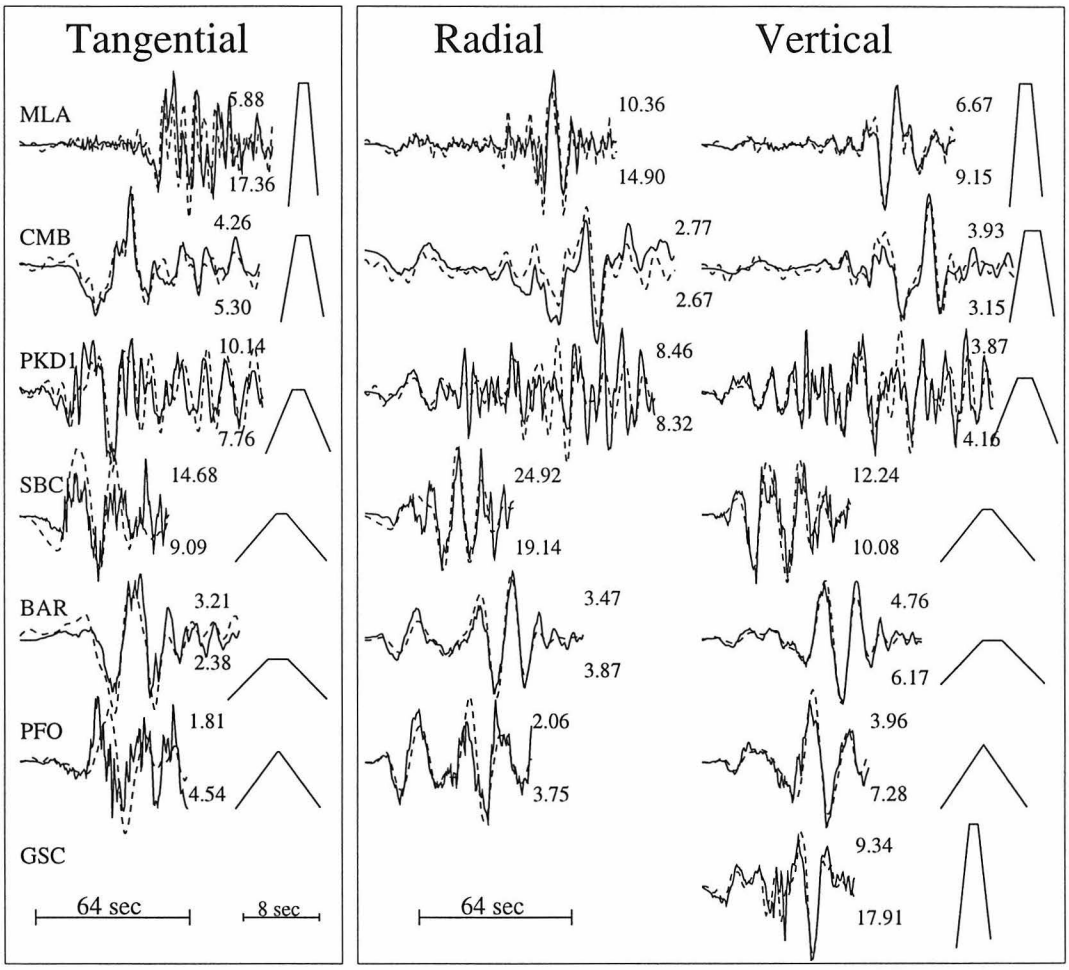

Figure 4.9: Comparison similar to Figure 4.7 except that the trapezoidal far-field source-time functions used here are the predicted ones from our simple rupture model. Peak amplitudes (mm) are shown above each trace for the data and below for the simulation. An amplitude ratio of 2600 between the main event and the eGf simulation is applied.

lowing more parameters as demonstrated for this same event by *Dreger* [1994]. He achieved this by applying a deconvolution of the aftershock from the mainshock observations and inverting for individual slip vectors on a 1160-element grid. Several zones of strong slip (asperities) were identified from this procedure which presumably are controlled by the short period signals at some stations such as observed at SBC in Figure 4.9. The reliability of these detailed results depends on the quality of the eGfs. However, non-uniform slip for this event is also recoverable from teleseismic observations as given by *Thio and Kanamori* [1996]. Figure 4.10 compares the mainshock data with the eGf simulations using their source model. The complexity in this source model does improve the short-period empirical fitting to the mainshock data at some stations. For example, the three pulses on the tangential component at station SBC are modeled quite successfully. Although there are no significant improvement of the overall fit to the mainshock data in Figure 4.10 over that in Figure 4.9, we do see that the regional broadband recordings bear information on the source asperity.

The average surface wave amplitude ratio for a source at 15 km depth to one at 17 km depth is about 1.2 for the ranges studied, assuming the SC structure. Choosing this value for $F(\vec{\xi}_{\mathbf{c}} - \vec{\xi}_{\mathbf{a}})$ in equation(8), we obtain a moment of $(1.5 \pm 1.5) \times 10^{26}$ dyne·cm for the main event from the aftershock moment (Figure 4.7). The uncertainty includes those inherited from the aftershock moment estimation and those that reflect the scattering in the peak amplitude ratio between the mainshock data and the empirical simulations (Figure 4.7). The latter is partially introduced by the difference between the source mechanism of the two events and the fact that the main event spanned a large depth range. We have excluded the tangential component at the station PFO in the above estimation since its peak amplitude is especially sensitive to the source mechanism change (Figure 4.11), probably because it is near the null axis of the focal sphere.

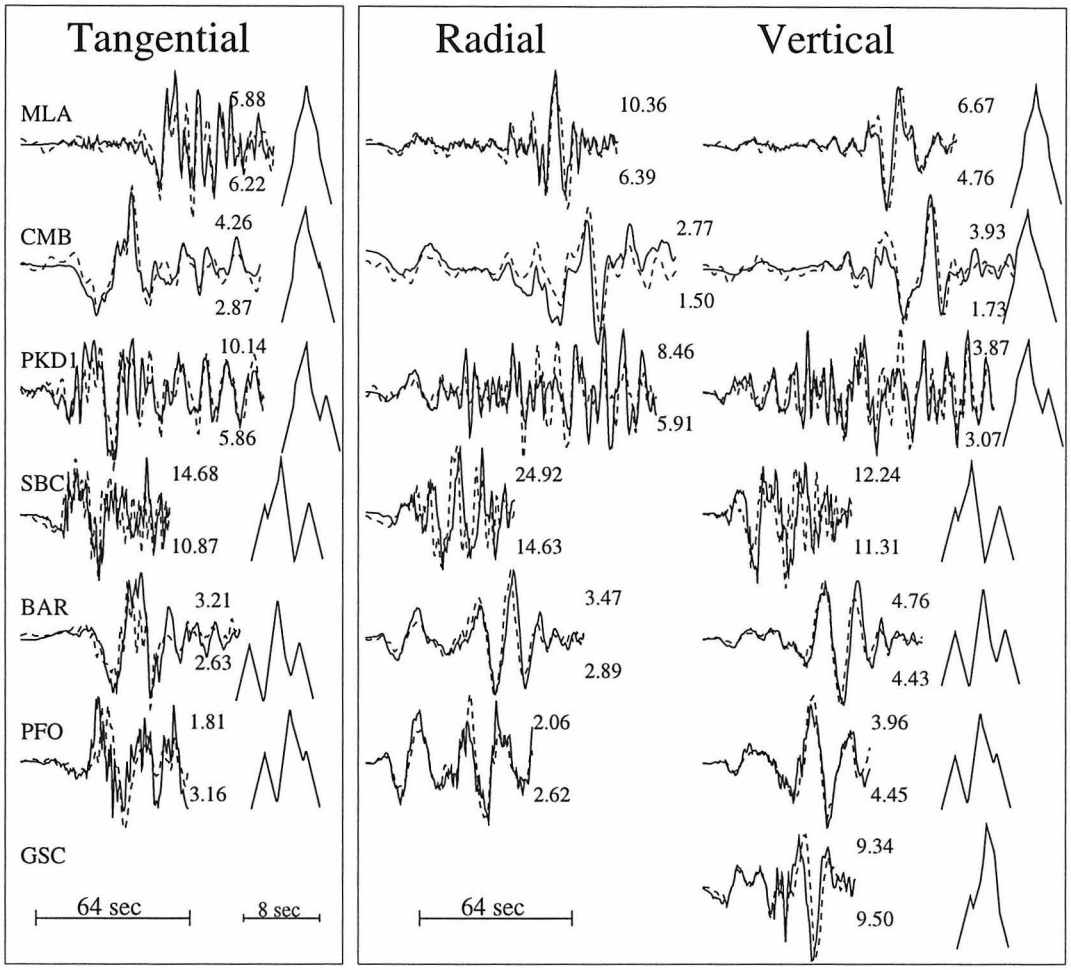

Figure 4.10: Comparison similar to Figure 4.7 except that the moment and the far-field source-time functions used here are synthesized from the results of *Thio and Kanamori* [1996].

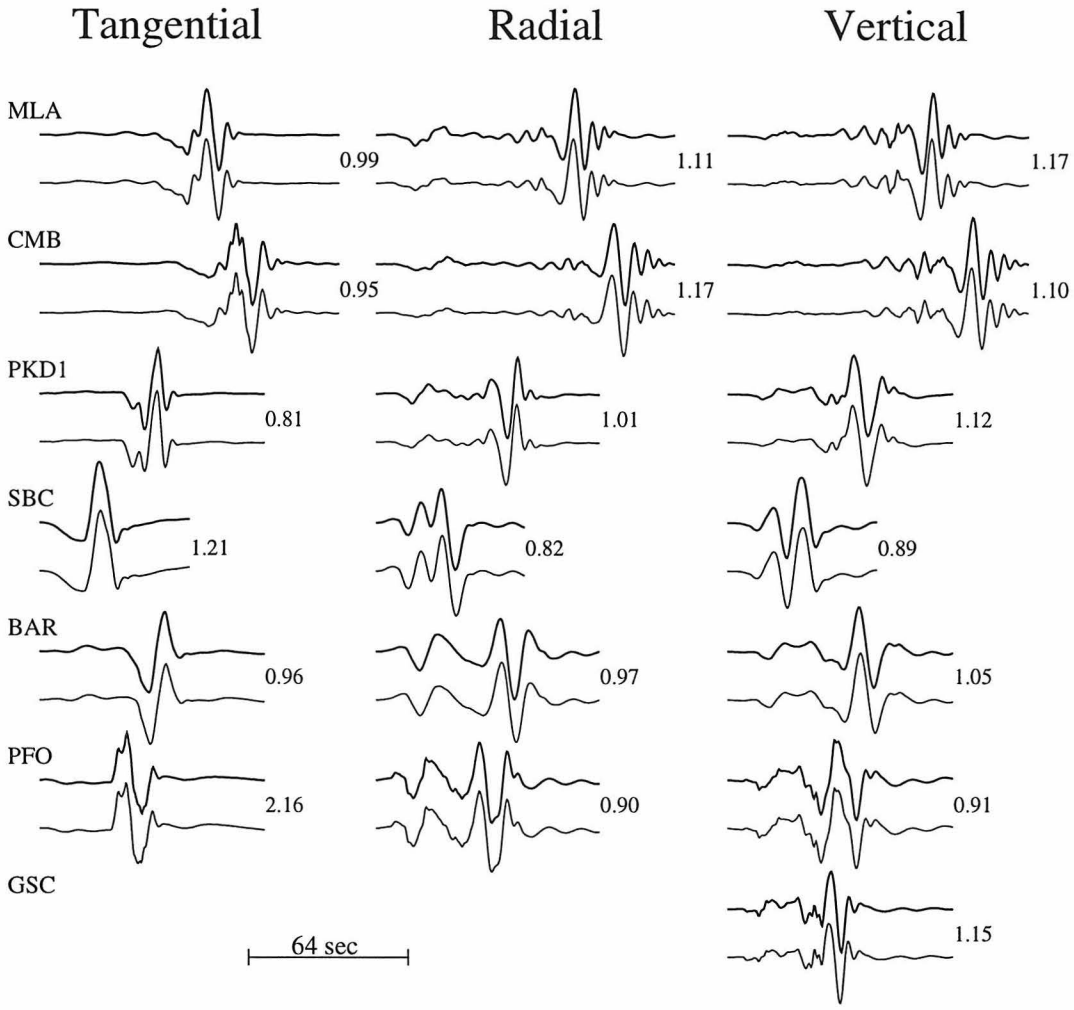

Figure 4.11: Comparison of two groups of synthetic waveforms generated with the aftershock source mechanism (top traces) and the mainshock source mechanism (bottom traces), respectively. A common seismic moment and the same set of far-field source-time functions in Figure 4.7 are used for the synthetics in each group. The number indicates the peak amplitude ratio between the bottom trace and the top trace for each pair of synthetics.

4.5 Discussion

To answer the question of directivity in a more elegant manner, it is necessary to explain in greater detail a few assumptions made in the preceding sections. In the process of determining the rupture direction of the main event, we have used the south-dipping plane as the fault plane. On this plane, the preferred rupture direction is parallel to the direction of the average rake vector, that is, upward and roughly northward. The main event spanned a depth range from about 19 km to 12 km. If the rupture takes place on the conjugate nodal plane, a rupture direction towards the north and downward produces equally good fits to the trapezoidal duration. Thus, just as first-motion study alone does not discern the true fault plane from its auxiliary plane, our method alone does not discern the most likely rupture direction from the other equally good candidate. However, in the case of the Northridge Earthquake, we can combine the information we get in the last two sections to uniquely determine the fault plane and the rupture direction. As discussed earlier, the earthquake initiated deep and a substantial amount of energy was released at a depth greater than the average depth. This is consistent with the focal depth, 19 km, given by *Hauksson et al.* [1995]. However, our average source depth, in terms of energy release, is shallower than the depth of initial rupture. Thus these arguments together suggest that rupture propagated upward and thus on the south-dipping plane, as demonstrated by the aftershock distribution [*Hauksson et al.*, 1995]. We have developed the capability to determine this feature before the aftershock distribution information becomes available.

For an eGf study to be justified, it is required that the mainshock have the same source mechanism as the aftershock and that this mechanism persist during its rupture so that the radiation patterns of the two sources are similar. It is also required that the aftershock occur sufficiently close to the mainshock so that path effects and timing can be considered identical. In the Northridge earthquake study, the two events have source mechanisms similar enough that the change in the synthetic waveforms due to the slight difference in the source mechanism can be ignored for our purposes

(Figure 4.11). More over, as discussed earlier, the main event remained about the same source mechanism throughout its rupture. Thus, we believe that the radiation pattern of the main event is adequately accounted for by the aftershock. Generally, if the two events are close enough to make the eGf method appropriate, but are off in location by a small amount, we may see a small relative time shift between the mainshock data and the corresponding empirical simulation. In Figure 4.7, however, the data and the empirical simulation are aligned in absolute travel time and no significant time shifts are observed. This indicates the compatibility of the relative location and the origin time of these two events. Note that the small uncertainty in the source depth of the aftershock has little effect on the relative timing of the regional seismograms from the two events and will not affect our conclusion of the general rupture direction. Moreover, since we have corrected for the depth effect in our moment estimation for the main event from the aftershock, the impact of the aftershock depth on the moment estimation of the main event will be small.

In Figure 4.12, we use broader far-field source-time functions and let them vary from station to station. Most of the misfit of the surface wave width between data and synthetics in Figure 4.4 disappears (*e.g.,* stations BAR and PFO). However, the surface waves at most stations, such as PKD1 and SBC, are still not well-modeled, due to the inadequacy of the tGfs. At these stations, the data contain many signals not seen on the synthetic waveforms. Some records, such as those at the station PKD1, are so complicated that it becomes difficult to distinguish body waves from surface waves. The amplitude data in Figure 4.5 is also scattered, which is responsible for the error in the moment estimation for the aftershock. In this figure, while the synthetic amplitude fits to the vertical (whole) are very good, with the largest error being only 23%, the differences on the radial are sizeable. The amplitude ratio of radial to vertical is less than one for most of the synthetics, which is also true for the data at the hard-rock sites BAR and PFO. This feature is also apparent in Figure 4.12 in the comparison between the mainshock data and the theoretical synthetics. The stations showing the largest radial to vertical amplitude ratios are PKD1, SBC and MLA. These same stations are rich in high frequency arrivals relative to hard rock

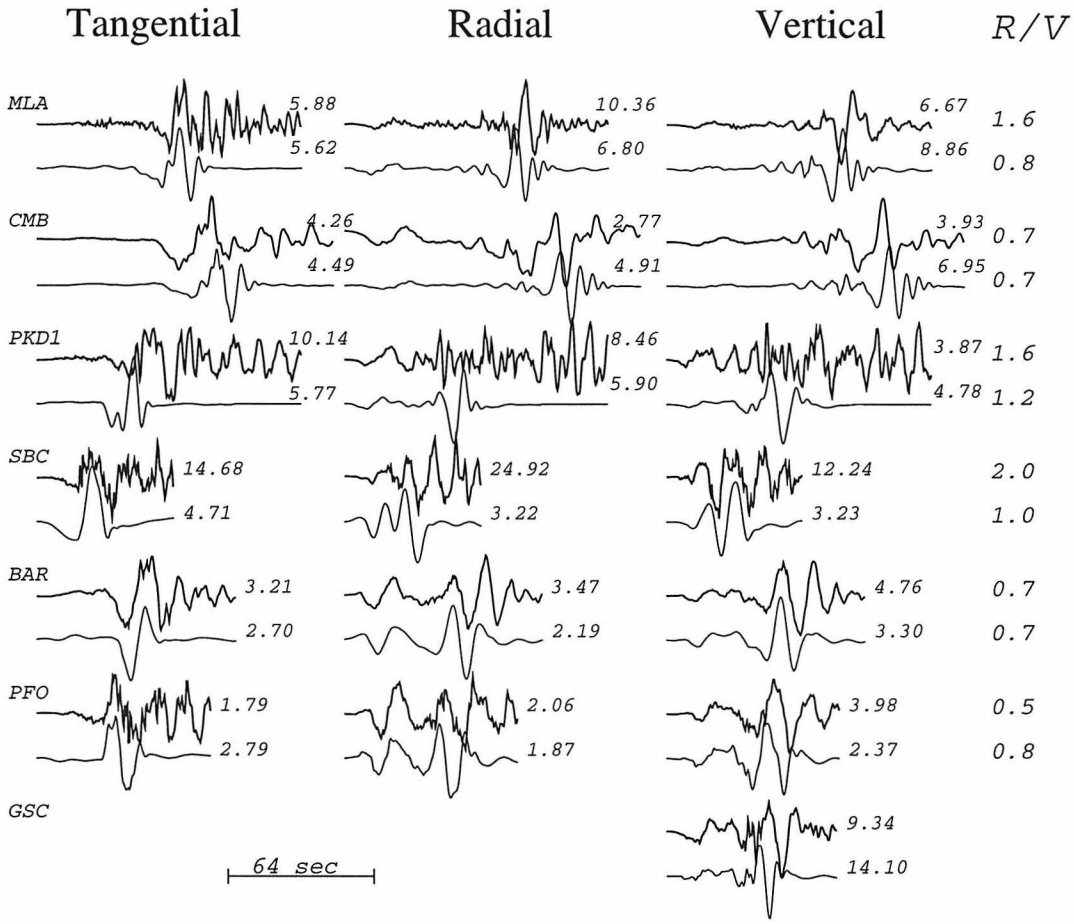

Figure 4.12: Comparison of displacement data (top traces) from the Northridge mainshock and the corresponding theoretical synthetics (bottom traces). Each pair of seismograms are aligned in absolute travel time. Peak amplitudes (mm) are given above each trace. A moment of 8.1×10^{25} dyne·cm and the same set of far-field source-time functions in Figure 4.7 are used for the synthetics. The rightmost column is the amplitude ratio (R/V) of the radial component to the vertical component for the data and the synthetics.

V_P (km/sec)	V_S (km/sec)	ρ g/cm^3	thickness km
Basin structure (from top):			
2.2	1.0	1.7	1
3.3	1.67	2.0	1
4.4	2.34	2.3	2
5.0	2.84	2.5	3
5.72	3.3	2.7	4
Crustal structure (from top):			
2.8	1.5	2.5	0.8
5.72	3.3	2.7	3.2
6.2	3.58	2.8	20
6.9	4.0	3.0	1
7.8	4.45	3.4	5
7.8	4.40	3.4	10
7.8	4.35	3.4	-

Table 4.2: Elastic constants for models in Figure 4.13

stations (e.g., compare MLA to CMB).

Such complexities are difficult to model theoretically but some of these features can be seen in 2-D synthetics such as those shown in Figure 4.13 [*Stead*, 1990]. The upper panel of this figure shows four different crustal models (Table 4.2); the lower panel shows three-component seismograms corresponding to these models. Note that the waveforms, especially the P_{nl} portion, are similar in all cases. This partially explains the adequacy of simple flat-layered models in obtaining source parameters with P_{nl} waves alone. One substantial effect of the basin structure is the different time delays of the surface waves relative to the P_{nl} waves. Compared to those in Figure 4.13*a*, Rayleigh waves in Figure 4.13*b* develop an extra later pulse due to the basin structure near the source region. As discussed in *Ho-Liu and Helmberger* [1989], this later pulse becomes more obvious when the earthquake ruptures shallow soft materials. This may have happened in the case of the Northridge Earthquake, which occurred in the San Fernando basin. Seismograms in Figure 4.13*c* show the same feature as those in Figure 4.13*b*. Notice the change of the tangential and radial amplitudes versus the vertical amplitude from Figures 4.13*a* to 4.13*b*, and to 4.13*c*, as slow structure begins

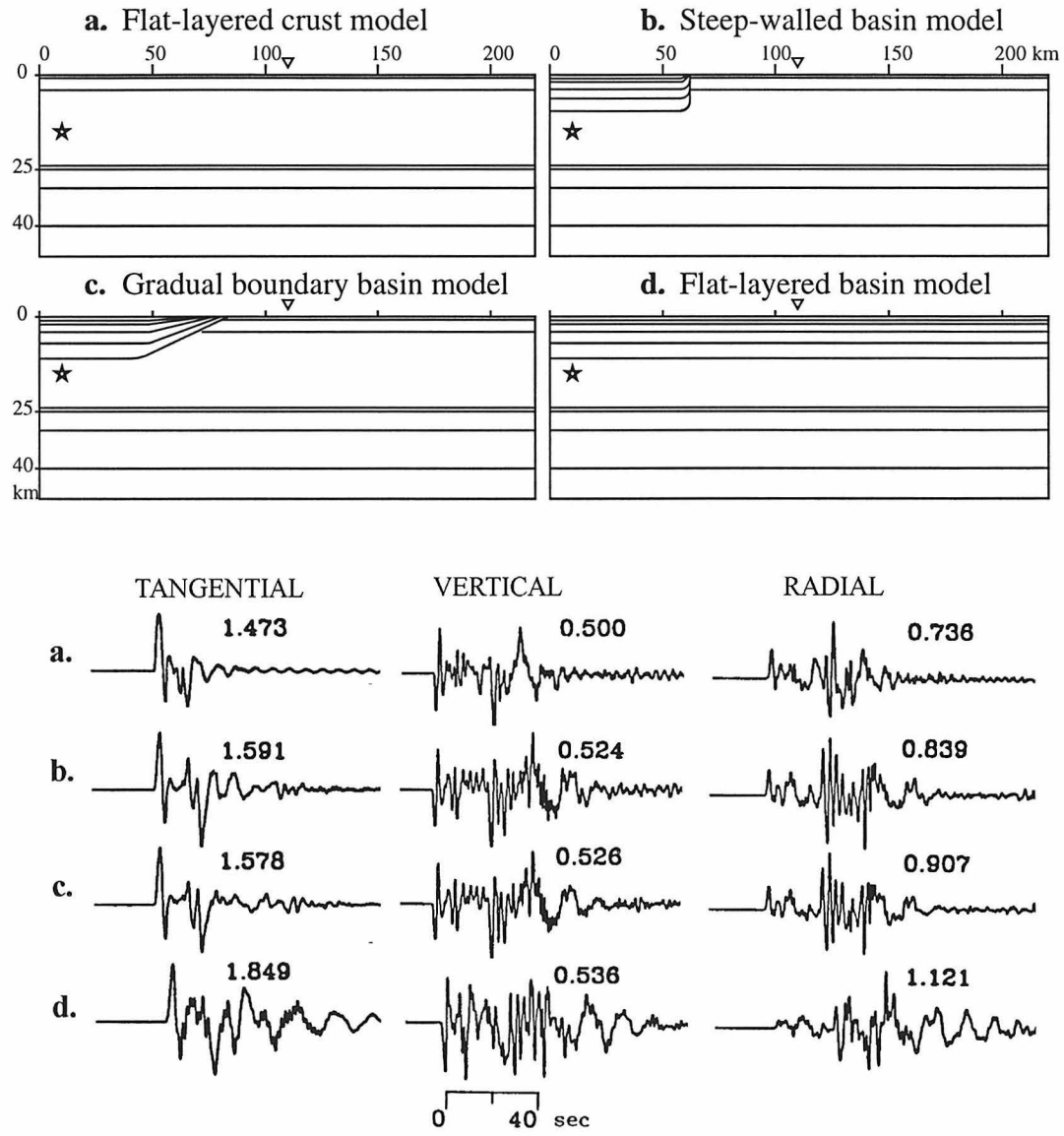

Figure 4.13: Four crustal models (upper panel) and the corresponding three-component seismograms (lower panel) computed with a finite difference method, after Stead [1990]. Sources are indicated by stars and receivers by triangles.

to dominate and as the transitional structure changes. The extreme case is shown in Figure 4.13*d*. When basin structures are involved in the whole source-receiver path, the radial component of the Rayleigh wave becomes exaggerated and the late-arriving scattered surface waves well developed. Paths connecting the Northridge Earthquake to Stations PKD1 and SBC would be two examples of these extremely complicated basin effects. Detailed 2-D modeling along these paths would explain both the waveforms and the amplitudes much better.

As far as the moment estimation is concerned, however, if we weight the vertical components relative to the horizontal in our moment estimation for the aftershock using the tGf approach, we would be able to reduce the moment uncertainty introduced by 2-D effects. Thus, the seismic moment estimate for the aftershock becomes $(6.1 \pm 1.6) \times 10^{22}$ dyne·cm, where the error (20% or $\pm 1.2 \times 10^{22}$ dyne·cm in this case) introduced by assuming a specific 1-D model is the major part of the uncertainty. The mainshock moment is now estimated to be $(1.4 \pm 0.9) \times 10^{26}$ dyne·cm. This uncertainty is smaller than that if we have taken the tGf approach for the mainshock moment estimation but still larger than commonly recognized.

4.6 Conclusions

In conclusion, we estimated the source parameters of the Northridge mainshock with comparatively stable P_{nl} waveforms, assuming a point double-couple source, and obtained the following solution for this earthquake: strike 128^0, dip 33^0 and rake 106^0. Addition of surface waves to the estimation procedure yielded a solution consistent with that obtained from the P_{nl} waveforms alone. A new method of using empirical Green's functions to constrain the fault dimension and rupture direction is introduced. Results for the Northridge Earthquake suggest that the mainshock ruptured a south-dipping plane with a fault dimension of 14 km, and propagated along the direction of the average rake vector. The most likely seismic moment is 1.4×10^{26} dyne·cm, as obtained from our eGf study, which is equivalent to a stress drop of about 120 bars on a fault of the above dimension. However, the seismic moment can range

from 0.5 to 2.3 $\times$ 10^{26} dyne·cm. Our results are compatible with those obtained by *Wald et al.* [1996] and *Thio and Kanamori* [1996].

Acknowledgements

We thank Craig Scrivner, Hiroo Kanamori, Chandan Saikia and one anonymous reviewer for their reviews of the manuscript. This research was supported by SCEC, contract number 569933 NSF EAR89-20136. Contribution No. 5545, Division of Geological and Planetary Sciences, California Institute of Technology, Pasadena, California.

Chapter 5 Source estimation of finite faults from broadband regional networks

5.1 Abstract

Fast estimation of point-source parameters for earthquakes has progressed much in recent years due to the development of broadband seismic networks. The expansion of these networks now provides the opportunity to investigate second-order effects such as source finiteness for regional and local events on a routine basis. This potential motivates the development of methods to quickly generate synthetic seismograms for finite sources. This is possible when the fault dimension is small compared to the source-receiver distance and when the structure around the source region is relatively simple. To study the directivity for a finite source, we discretize the fault region into a set of elements represented as point-sources. We then generate the generalized rays for the best-fitting point-source location and derive for each separate ray the response for neighboring point-sources using power series expansions. The response for a finite fault is then a summation over rays and elements. If we sum over elements first, we obtain an effective far-field source-time function for each ray, which is sensitive to the direction of rupture. These far-field source-time functions are convolved with the corresponding rays and the results summed to form the total response. A simple application of the above method is demonstrated with the tangential motions observed from the 1991 Sierra Madre earthquake. For this event, we constrain the fault dimension to be about 3 km with rupture towards the west, which is compatible with other more detailed studies.

5.2 Introduction

In recent years, due to the development of broadband seismic networks, the estimation of point-source parameters for earthquakes using regional records has been made faster and more reliable [*e.g. Thio and Kanamori*, 1995; *Ritsema and Lay*, 1995; *Walter*, 1993; *Dreger and Helmberger*, 1991a; *Patton and Zandt*, 1991]. *Zhao and Helmberger* [1994] developed a grid search method to estimate point-source orientation, depth, magnitude and duration with broadband data. This technique has been recently utilized by *Scrivner and Helmberger* [1995] in their preliminary work on developing an early warning system. However, synthetic fits to waveform data for many earthquakes could be significantly improved by adding directivity or fault finiteness, which indicates that source finiteness plays an important role for many moderate to large earthquakes. Thus, being able to quickly estimate such characteristics and generate synthetics for complex sources would be highly useful. Current methods used for generating responses from complex sources rely on direct summation of point-source responses or approximate reflectivity approaches based on source decomposition [*Saikia and Helmberger*, 1997], which are both time consuming processes. Here, we introduce a method based on the generalized ray theory [*Helmberger*, 1983] to efficiently compute synthetic seismograms for complex sources. This technique can be applied to faults with small dimensions compared to the source-receiver distance, in regions where the structure around the source can be modeled as a layer of constant velocity. We apply this method to estimate the source dimension and general directivity of the 1991 Sierra Madre, California earthquake. This event occurred in the middle of the TERRAscope array (Figure 5.1) and was well studied [*e.g. Dreger and Helmberger*, 1991a; *Wald*, 1992]. The latter study used a large collection of local data, strong motion and teleseismic seismograms to establish rupturing to the southwest. Comparing our results against this solution illustrates the usefulness of our new technique.

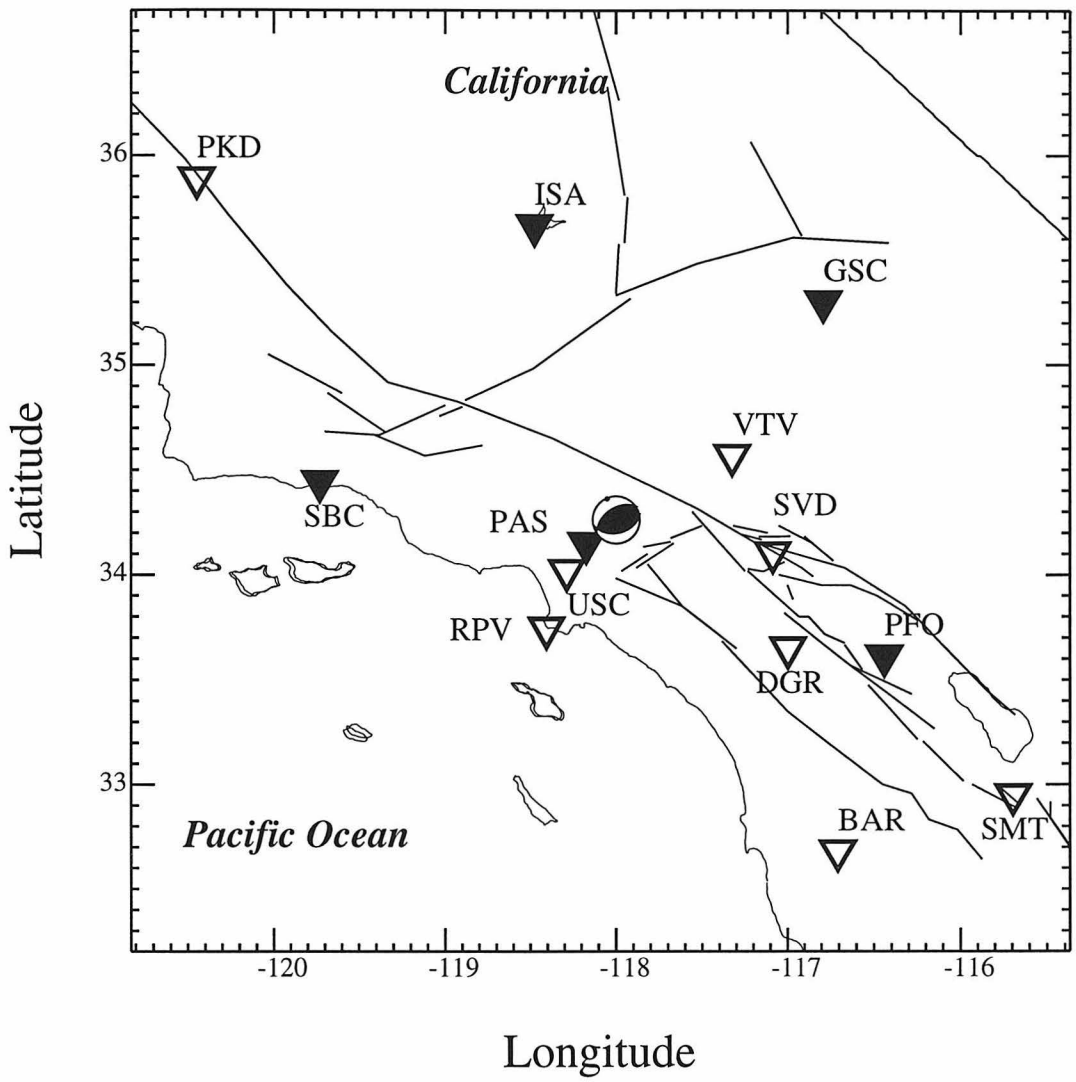

Figure 5.1: Broadband stations (triangles) located in southern California. Stations used in this study are plotted as solid triangles. The source mechanism of the Sierra Madre earthquake, determined by Dreger and Helmberger [1992], is shown at the epicenter.

5.3 The ray-shifting method

From the Generalized Ray Theory [*Helmberger*, 1983], for a layered half-space, a generalized ray with ray parameter p_0 is associated with the characteristic travel time, t_0,

$$t_0 = p_0 r + \sum_i \eta_i d_i. \tag{5.1}$$

r is the source-receiver distance. η_i is the vertical slowness of the ray in each layer and d_i is the vertical distance of the ray segment in each layer. If the paths from two point-sources are close, the responses at the receiver for the two point-sources are similar in shape and amplitude and differ primarily by a small time shift, dt_0 [*Helmberger et al.*, 1992]. As an approximation, we treat p_0 as constant and use a Taylor-series expansion for t_0 around the point-source position (r, h) to represent the time variance dt_0. That is,

$$dt_0 = \frac{\partial t_0}{\partial r} dr + \frac{\partial t_0}{\partial h} dh \tag{5.2}$$

with $\frac{\partial t_0}{\partial r} = p_0$ and $\frac{\partial t_0}{\partial h} = -\epsilon \eta_s$, where $\epsilon = 1$ for down-going rays, and $\epsilon = -1$ for up-going rays. $\eta_s = \left(\frac{1}{v_s^2} - p_0^2\right)^{\frac{1}{2}}$ is the vertical slowness of the ray p_0 in the source region, and v_s is the velocity in the source region. For a finite fault, we discretize the rupture region into a set of elements, each represented as a point-source (Figure 4.6). The total response, $s_j(t)$, at the receiver for a point-source j in the neighborhood of the reference point-source can be derived from that for the reference point-source by summing the rays, each properly lagged in time.

$$s_j(t) = \left(\sum_i R_i(t - dt_{0_{ij}}) \right) * f(t). \tag{5.3}$$

$R_i(t)$ is the response for ray i for the reference point-source, and $\sum_i$ indicates summation over rays. If the point-source is not a step dislocation, a far-field source-time function f(t) is used as in equation 5.3. Equation (3) is justified if we avoid source radiation nodes by omitting nodal stations.

To illustrate that the Taylor-series expansion and the shift technique are reasonable approximations, we compared the point-source responses that are calculated

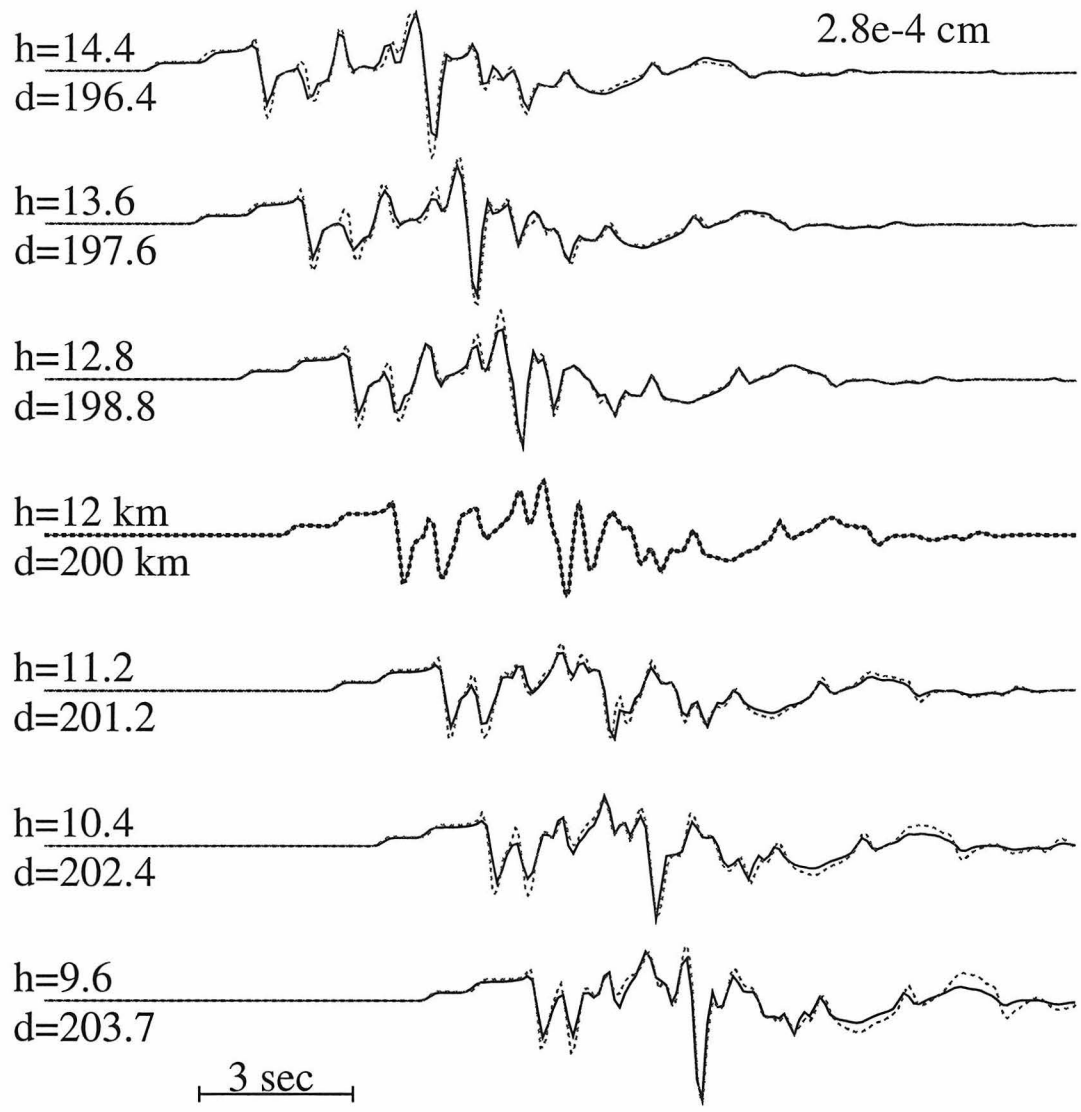

Figure 5.2: A set of point-sources are used to simulate a linear rupture on a fault plane (strike 242^0, dip 50^0, rake 74^0). Rupture starts at 14.4 km depth with a rupture angle 45^0. Seven point-sources on this line are selected here for comparison. Each dashed trace is the point-source response in displacement at the receiver for the given distance and depth. These point-source responses are calculated independently and shifted properly to reflect the origin time difference due to rupture, as in a conventional point-source summation procedure. Solid traces are point-source responses at the same receivers derived from the response for the h=12 km point-source by lagging each ray properly to reflect the origin time difference due to rupture and the travel time difference due to varying point-source positions using the Taylor-series expansion approximation for t_0. Crustal model SC (Table 1) is used for the calculations and a far-field source-time function (0.2 sec, 0.2 sec) is used for each point-source. Seismograms are plotted on the same scale with the amplitude of the first solid trace shown.

Model LOHS1				Model SC			
V_p (km/s)	V_s (km/s)	ρ (g/cc)	Z^1 (km)	V_p (km/s)	V_s (km/s)	ρ (g/cc)	Z (km)
4.5	2.6	2.4	0.0	5.5	3.18	2.4	0.0
5.9	3.5	2.67	4.0	6.3	3.64	2.67	5.5
6.6	3.8	2.8	16.0	6.7	3.87	2.8	16.0
8.0	4.1	3.1	26.0	7.8	4.5	3.0	35.0
8.2	4.2	3.3	30.0				

Table 5.1: Model parameters. After Dreger and Helmberger [1991]. Z is the depth to the top of the layer.

with equation 5.3 for the standard Southern California model (SC, Table 5.1) and those calculated exactly (Figure 5.2). Some of the more important ray responses for a source at a depth of 12 km are displayed in Figure 5.3. As the source changes depth, these arrivals interfere with each other, with the Love wave showing the most variation as displayed in Figure 5.2. The similarity of these two sets of responses demonstrates that the timing of the individual rays is a more important parameter than the change in individual waveshape.

For the finite fault, a time lag dT_j is applied to each point-source to simulate the propagation of the rupture front across the fault, and the total response $S(t)$ at the receiver is the sum of those for all the point-sources,

$$S(t) = \sum_j w_j s_j(t - dT_j) = \sum_j w_j \left(\sum_i R_i(t - dt_{0_{ij}} - dT_j) \right) * f(t) \qquad (5.4)$$

where $\sum_j$ indicates summation over point-sources, and w_j is the weighting factor for point-source j, representing slip distribution on the fault plane (Figure 4.6). If we generate and store the separate generalized rays for the best fitting point-source location, we can then shift each ray accordingly and sum them to form the total response of a complex source, as in equation 5.4.

Rearranging the summation, equation 5.4 can be rewritten as

$$S(t) = \sum_j w_j \left(\sum_i R_i(t) * \delta(t - dt_{0_{ij}} - dT_j) \right) * f(t) \qquad (5.5)$$

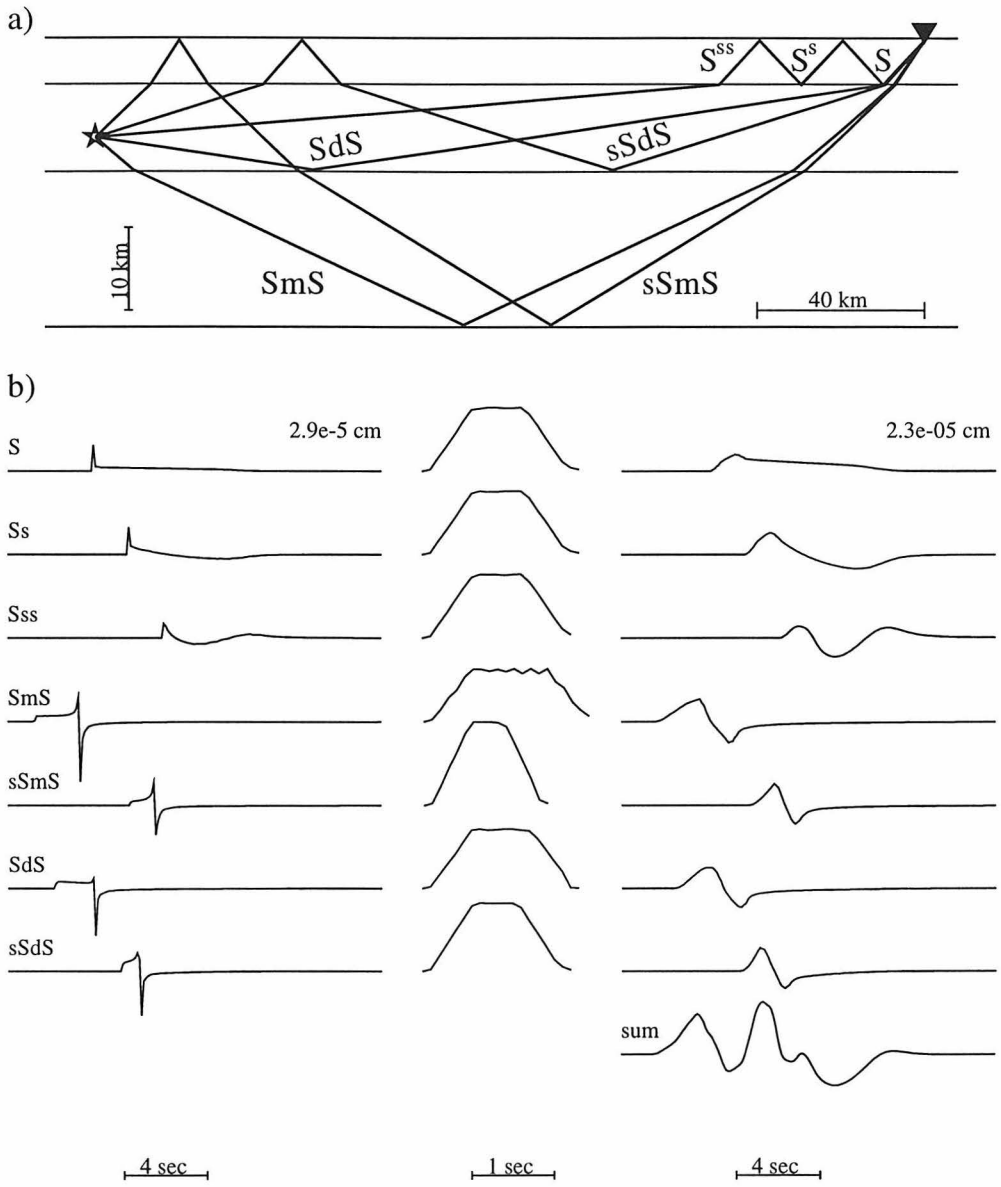

Figure 5.3: a). Paths of some of the important rays shown in *b)*. The star indicates the source and the triangle the receiver. b). Ray responses (left column, displacement) and the corresponding unit-area far-field source-time functions (middle column, with a different time scale). Each ray is convolved with its corresponding far-field source-time function and the results (right column) are summed to form the total response (the right bottom trace) from the complex source. In this example, a 3-km-long line source segment propagates 2 km up-dip from a depth of 12 km at a constant velocity 3.0 km/sec on a fault plane striking 242^0 and dipping 50^0. Source-receiver distance is 200 km and the station azimuth is 44^0. Seismograms are plotted on the same scale with the amplitude of the first trace in each column shown. A far-field source-time function (0.1, 0.1, 0.1 sec) is used for each point-source. Model SC (Table 1) is used.

or,

$$S(t) = \sum_i R_i(t) * \sum_j w_j \left(\delta \left(t - dt_{0_{ij}} - dT_j \right) * f(t) \right). \tag{5.6}$$

In this manner, we have defined a far-field source-time function

$$F_i(t) = f(t) * \sum_j w_j \delta(t - dt_{0_{ij}} - dT_j) \tag{5.7}$$

for ray i as the result of the rupture across the finite fault. Equation 5.7 is similar to equation (A1) in *Langston* [1978], except that the latter approximates $dt_{0_{ij}}$ with an analytic expression which is appropriate for teleseismic rays. From this point of view, the total response at the receiver can be seen as the summation of all the generalized rays convolved with corresponding far-field source-time functions.

In Figure 5.3*b*, a set of rays are selected to demonstrate the process of building the total response for a complex source via equation 5.6. Note that each ray, unlike rays from a point-source, has its own individual source-time function dependent on its ray parameter. In this case of up-going rupture, the source-time functions for down-going rays (*e.g.* SmS, SdS) have longer durations than those for up-going rays (*e.g.* $sSmS, sSdS$). Given the fault geometry and the faulting characteristics, one can generate synthetics in this way much faster than direct summation of point-source responses. In the next section, we will apply this technique to a forward search procedure to constrain the fault dimension and directivity.

5.4 Application to the 1991 Sierra Madre earthquake

The simplest application of the above method is to estimate the source dimension and general directivity of an earthquake assuming models with no asperities. We applied our method to the 1991 Sierra Madre earthquake, which occurred in the middle of the TERRAscope array and was well recorded at stations PFO, GSC, ISA and SBC. Although we did not restrict the response $S(t)$ in equation 5.6 to be the tangential

motion, we will use only the tangential components in this experiment to reduce the number of rays involved for simplicity. We use the tangential components of broadband data from the four stations PFO, GSC, ISA and SBC to estimate the fault dimension and the rupture direction. Broadband records of this event were inverted by *Dreger and Helmberger* [1991a] to obtain a point-source solution with strike 235^0, dip 50^0, and rake 74^0. They used a triangular far-field source-time function with a duration of 1 sec, determined by measuring the width of the tangential component direct *S*-wave recorded at station PAS.

We investigate the fault dimension and general directivity via a forward search approach, using simple fault models of square faults with uniform slip. Using the Haskell model [*Haskell*, 1964], a finite fault is simulated with a propagating line source with a constant velocity (Figure 4.6). For this earthquake, a triangular far-field slip function of duration 0.1 sec is used for the line source. We test faults of a range of dimensions. For each fault, the rupture angle is allowed to vary from 0^0 to 360^0 in increments of 15^0. Synthetic seismograms are generated for each station and compared to the data. The fitness of a certain source geometry, the fault dimension and the rupture direction, is judged based on the least-square error between data and synthetics, defined as,

$$Misfit = \frac{\sum_s \left(\frac{r_s}{r_0}\right)^p \int_t [Obs(t) - Syn(t)]^2 \, dt}{\sum_s \left(\frac{r_s}{r_0}\right)^p \int_t Obs(t)^2 dt}. \tag{5.8}$$

$\sum_s$ indicates summation over stations. Distance correction $\left(\frac{r_s}{r_0}\right)^p$ is applied to give stations at different distance, r_s, approximately the same weighting [*Zhu and Helmberger*, 1996a]. $r_0 = 200$ km is a reference distance and $p = 1$ is used in these tests since we are mostly dealing with Love waves.

Figure 5.4 shows the misfit between data and synthetics as a function of rupture angle on the fault plane (strike 235^0, solid circles) for selected fault sizes. Although the fault size varies significantly, these functions show similar patterns and the indicated rupture direction is not strongly related to the fault size. For this test, the functions all

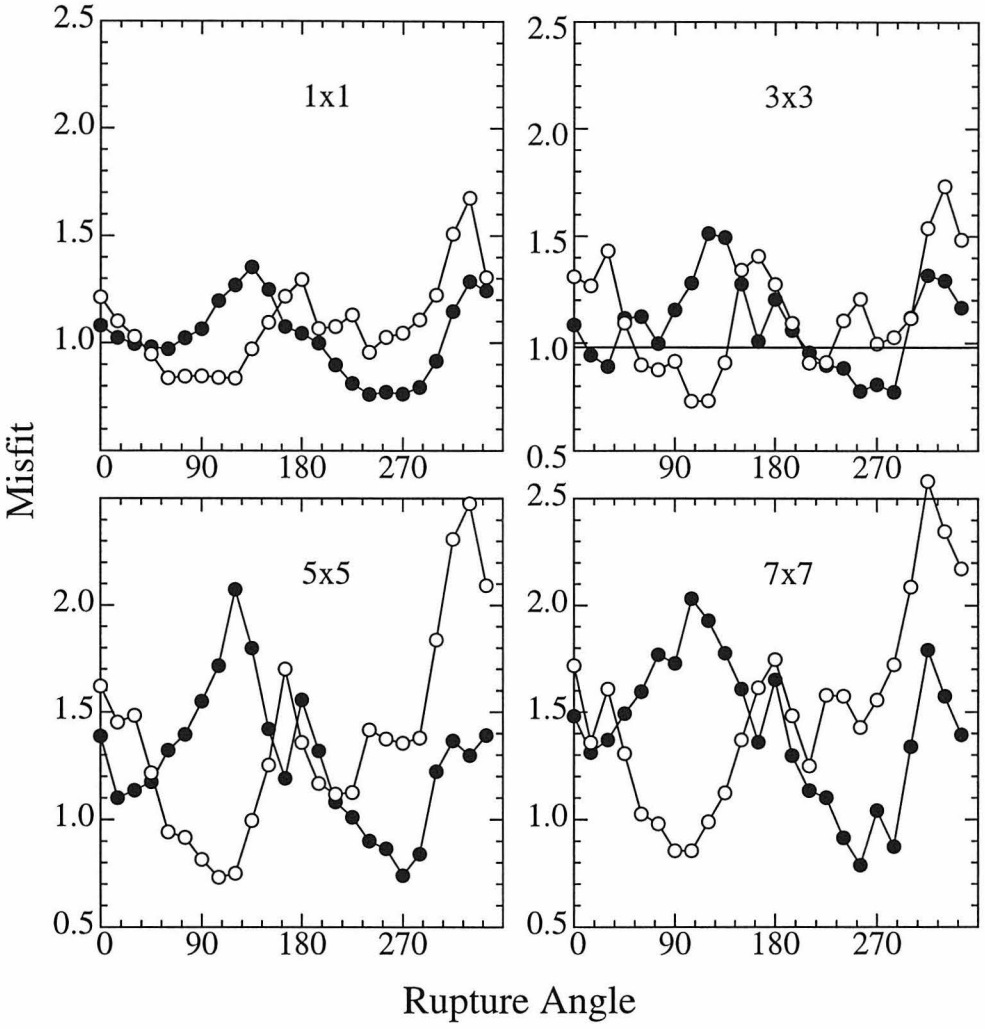

Figure 5.4: Misfit between data and synthetics as a function of rupture angle on the fault plane for different fault dimensions selected to model the 1991 Sierra Madre event. Solid circles are for rupture on the fault plane. Open circles, the conjugate plane. Rupture velocity is 3.1 km/sec. Stations GSC, PFO, SBC, and ISA are used and the crustal model is SC (Table 1). The straight line in the 3×3 box indicates the misfit value for synthetics with Dreger and Helmberger's [1991] point-source.

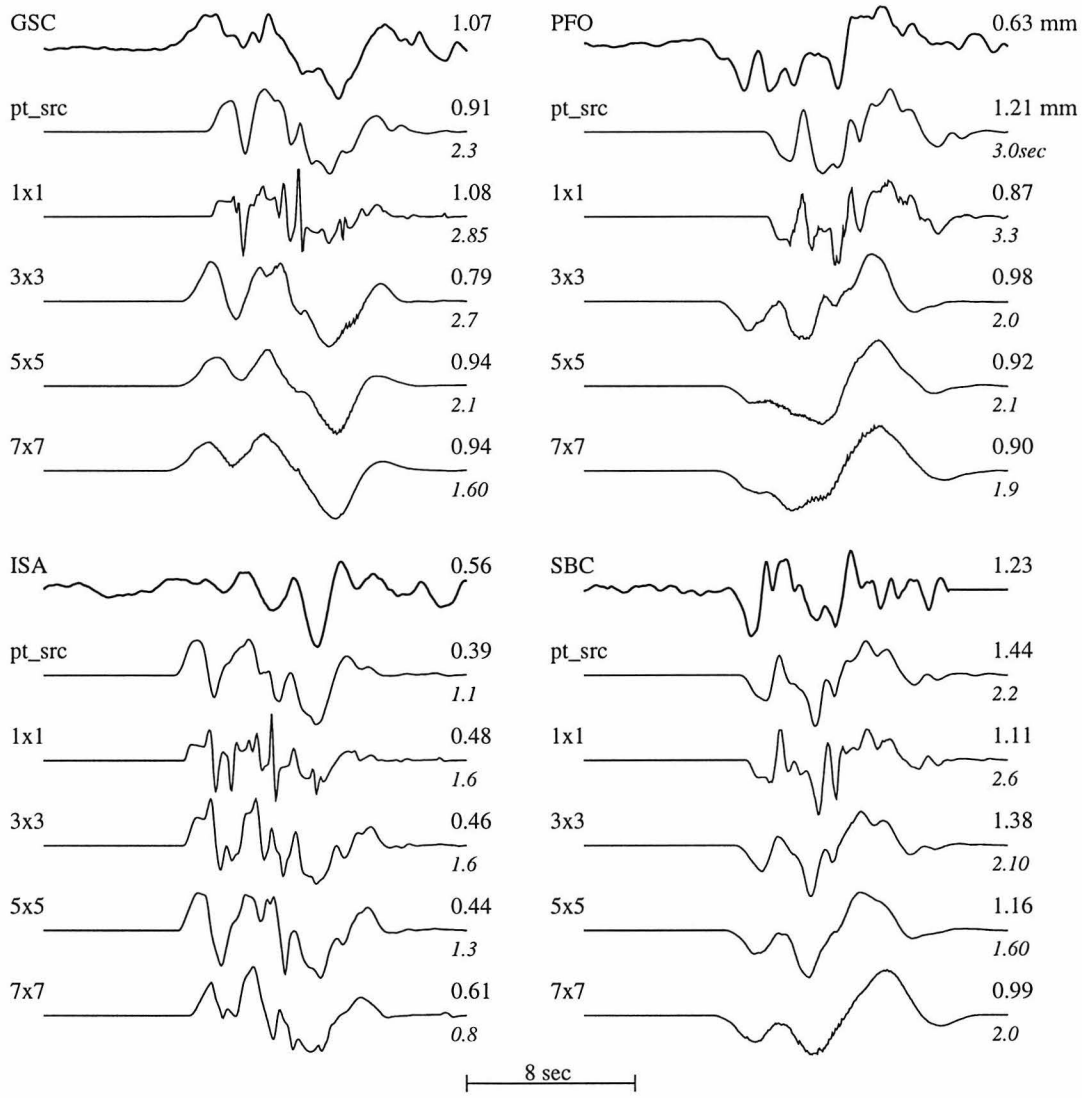

Figure 5.5: Comparison between data and the best-fitting synthetics for different fault sizes, for the 1991 Sierra Madre event. Fault sizes are shown at the beginning of each synthetic trace. "Pt_src" indicates Dreger and Helmberger's [1991] point-source. The rupture angles used are the best ones found in the appropriate boxes in Figure 5.4. Synthetics are shifted in time relative to the data before computing the misfit and the amount of shift is shown in seconds. A positive number indicates synthetic shifting to the right. Seismic moments of $3.6, 2.0, 3.6, 4.6$ and 5.6×10^{24} dyne·cm are used for the synthetics, respectively, as determined in the modeling process. Seismogram amplitudes are given in mm.

have smaller values for rupture angles around 270^0, which indicates rupture downdip on the fault plane. The minimum misfit value for different fault sizes are at the same level, but the misfit function is more sensitive to the rupture direction for larger faults. If rupture is placed on the conjugate plane (strike 79^0, open circles), smaller misfit values occur at the rupture angles around 100^0, which indicates rupture updip on the conjugate plane. In both cases, the horizontal component of the rupture is toward northwest. Figure 5.5 shows the comparison between data and the best-fitting synthetics for these preferred fault orientations. Synthetics for Dreger and Helmberger's [1991b] point-source is also shown for comparison. These synthetics fit the data in shape reasonably well, but the amplitude variation is relatively large (about 40%). In this respects, finite faults make better predictions than does the point-source. In waveshape, synthetics for fault size 3×3 and $5 \times 5 km^2$ also fit the data better than the point-source synthetics, especially for stations GSC and PFO. Nevertheless, based on these misfit functions displayed in Figure 5.4, it is difficult to determine the fault dimension without other data. However, other finite-source inversion studies usually assume additional constraints such as moment, which is determined by teleseismic modeling or long period regional inversions [*Wald*, 1992]. If we adopt Zhao and Helmberger's [1994] moment estimates of $(3.0 \pm 0.7) \times 10^{24}$ dyne·cm, we can eliminate those fault dimensions greater than 5 km by assuming rupture velocities less than the shear velocity in the fault region. Smaller dimensions are still possible if we allow longer rise times for the line source, but a fault dimension of 3 km appears the most appropriate.

As mentioned earlier, the Taylor-series expansion and time domain shift technique in our method is most appropriate for large source-receiver distance. For short distance, the ray parameter of a generalized ray from a point-source to the receiver is subject to substantial change as the position of the point-source changes on the finite fault. In Figure 5.6, we compare the synthetics calculated via our approximation and those calculated by directly summing point-source responses for a small source-receiver distance. In each group, the seismograms are aligned in absolute timing. The comparison indicates that the approximation yields a slight shift, delay in this case,

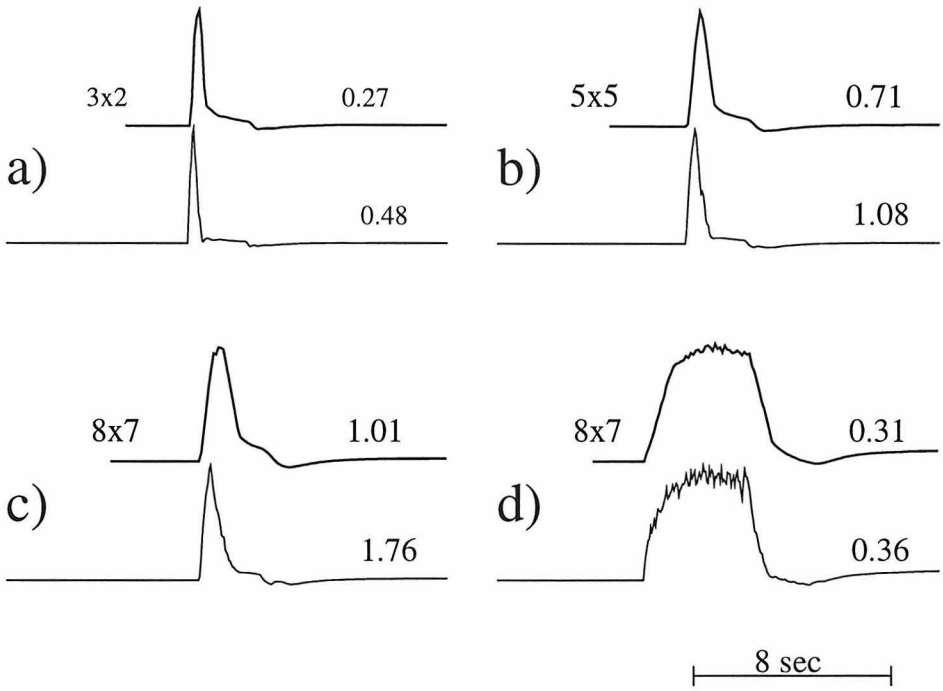

Figure 5.6: Comparison between synthetics calculated with our method (upper traces) and those calculated by directly summing point-source responses (lower traces) for a short distance (21 km). Fault sizes are given in *km*. Point source orientation is: strike 235^0, dip 50^0, rake 74^0. Station azimuth is 232^0. Rupture angles are 45^0 for *a), b)* and*c)*; 225^0 for *d)*. Numbers at the end of each trace indicate relative peak amplitude.

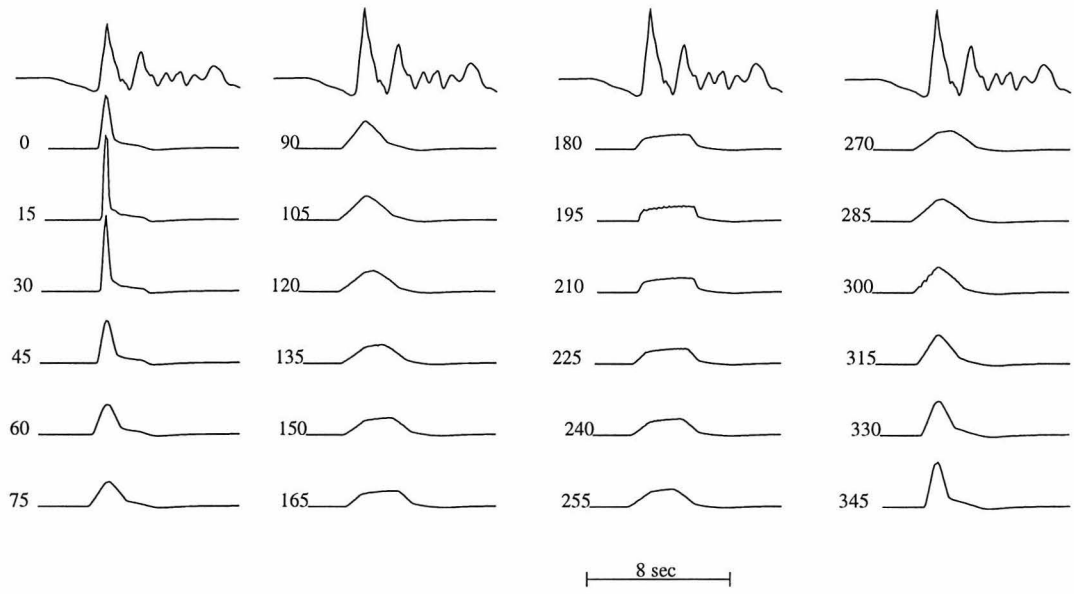

Figure 5.7: Comparison between data (PAS, tangential motion, the first trace in each column) and synthetics for fault size 5×5 km and varying rupture angles. Seismograms in each column are aligned in absolute timing and scaled with respect to peak amplitude. Numbers indicate rupture angles.

of the main energy group. The overall wave shape are simulated reasonably well, but some high-frequency energy is lost due to the smoothing effect associated with the approximation, especially when the rupture is towards the station (Figure 5.6*(a), (b), (c)*).

However, since we are always using imperfect Green's functions in various modeling practice, the above inadequacy does not necessarily make the approximation unusable. In cases where the major concern is the wave shape, instead of timing or amplitude, as in the procedure described above, our rough approximation provides a fast means to calculate synthetics for complex sources. This encourages us to use local stations in the procedure to constrain the fault size and general rupture direction. In this test, we use crustal model LOHS1 [*Dreger and Helmberger*, 1991a] and the tangential motion observed at station PAS. For illustration, the synthetics for fault size 5×5 km^2 and varying rupture angles are compared with the data in Figure 5.7. Since the direct arrival (S) is by far the strongest pulse in the synthetics for local stations, unlike regional records, the various synthetics in Figure 5.7 are essentially

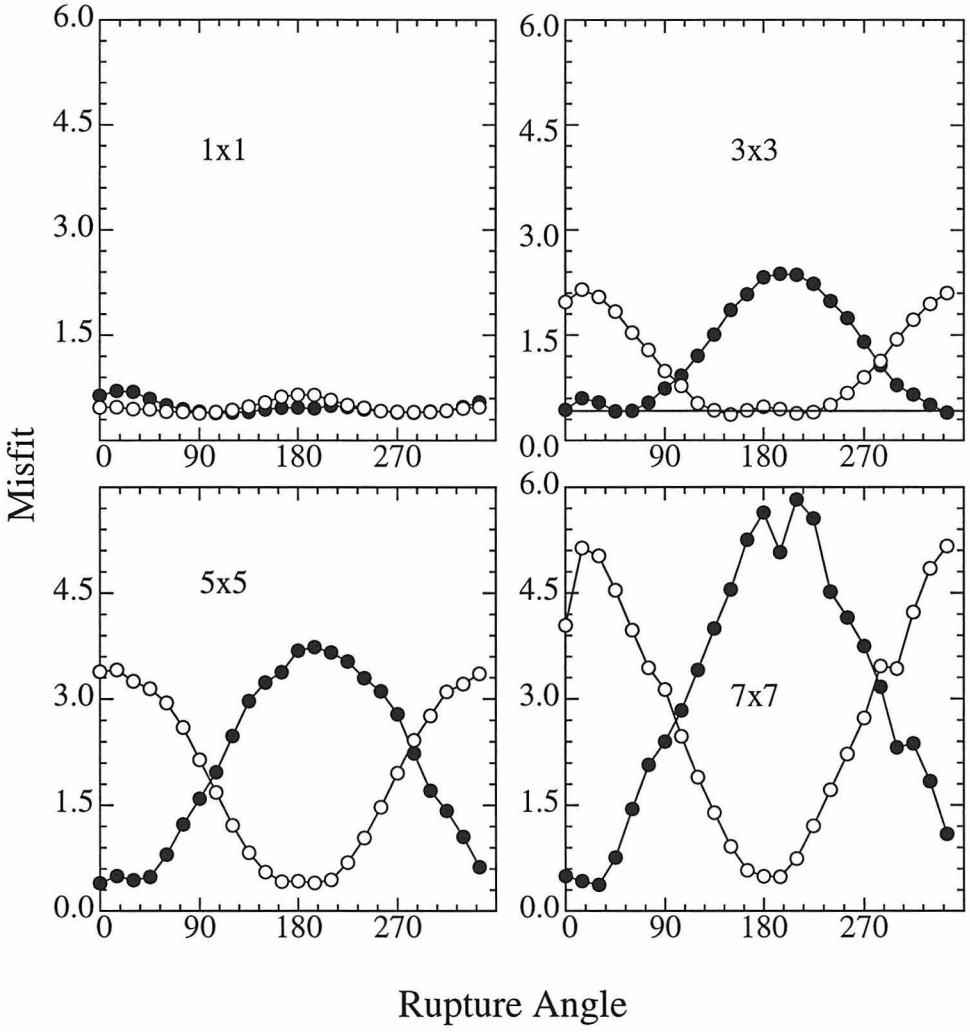

Figure 5.8: Misfit between data and synthetics as a function of rupture angle on the fault plane (solid circles) for different fault dimensions. Only the tangential motion at station PAS is used in this test. Open circles are for rupture on the conjugate plane. Rupture settings are the same as in Figure 5.4. Model LOHS1 [Table 1] is used. The straight line in the 3×3 box indicates the misfit value for synthetics with Dreger and Helmberger's [1991] point-source.

different fits of direct S to the first pulse in the data. With the simple source model we are using, the far-field source-time function for direct S is a trapezoid, and the search among different fault size and rupture direction is mainly a procedure to find a trapezoid with appropriate width. When the fault size is fixed at 5×5 km^2, rupture angles around 0^0 (rupture towards southwest) are preferred (Figure 5.8). At about 200^0 (rupture away from PAS) the code actually fits the direct S to the first two pulses in the data. Note that there is serious trade-off between the fault size and rupture angle in affecting the width of the source-time function of one ray. This is clearly seen in Figure 5.8, where the misfit between synthetics and data is shown as a function of the rupture angle. When the fault size gets smaller, the pulse width, thus the misfit function becomes less sensitive to the rupture direction. The fault with a dimension of 1 km behaves like a point source, although we do see that, on this small fault, rupture towards PAS makes the direct S pulse in the synthetics too sharp and rupture away from PAS makes it too broad. The preferred rupture direction is actually updip or downdip. This trade-off between the fault size and the rupture direction can be avoided if better local-station coverage is provided. Or, we can use the information we gain from the modeling of the regional records to constrain the fault size, as discussed above. With the fault size so constrained, local data is a better indicator of the rupture direction, since it is dominated by fewer rays.

In our next experiment, we combine the local data (station PAS) with regional data (stations GSC and PFO) in the modeling process. Station ISA and SBC were excluded since the problem with the Green's functions for these two stations are more severe than for the others [*Helmberger et al.*, 1992]. The misfit functions for different fault sizes are shown in Figure 5.9. Figure 5.10 displays the fits for the preferred orientations. With these three stations, the misfit function is more sensitive to the fault size than in the previous experiments, and a fault size of 3 km is preferred based on the misfit functions. The general trend of these functions look more or less like those in Figure 5.8 for station PAS only, even though we have applied the distance correction in the definition of the misfit function. This indicates that, for a given fault size, station PAS plays a dominant role in determining the general rupture direction,

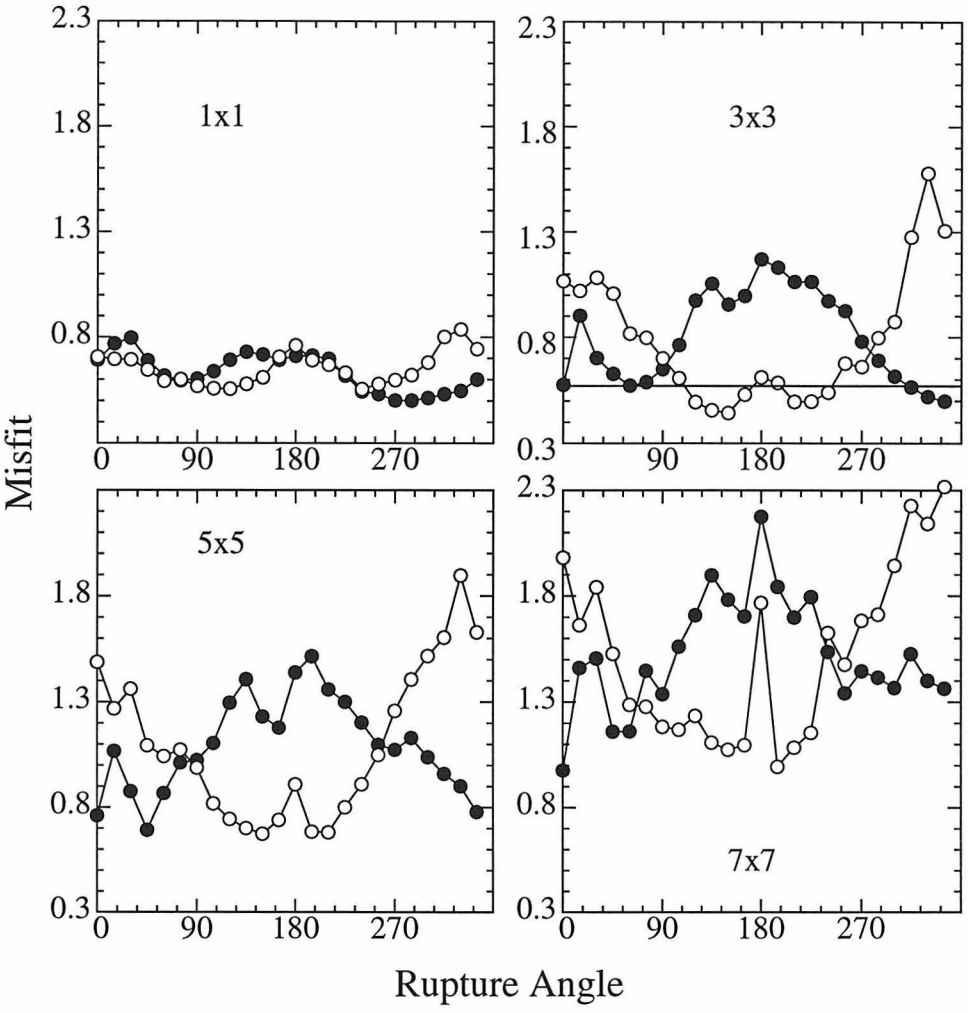

Figure 5.9: Misfit between data and synthetics as a function of rupture angle on the fault plane (solid circles) for different fault dimensions. Tangential displacement data at stations PAS, GSC and PFO are used. Open circles are for rupture on the conjugate plane. Rupture settings are the same as in Figure 5.4. Model SC is used for stations GSC and PFO. Model LOHS1 is used for station PAS. The straight line in the 3×3 box indicates the misfit value for synthetics with Dreger and Helmberger's [1991] point-source.

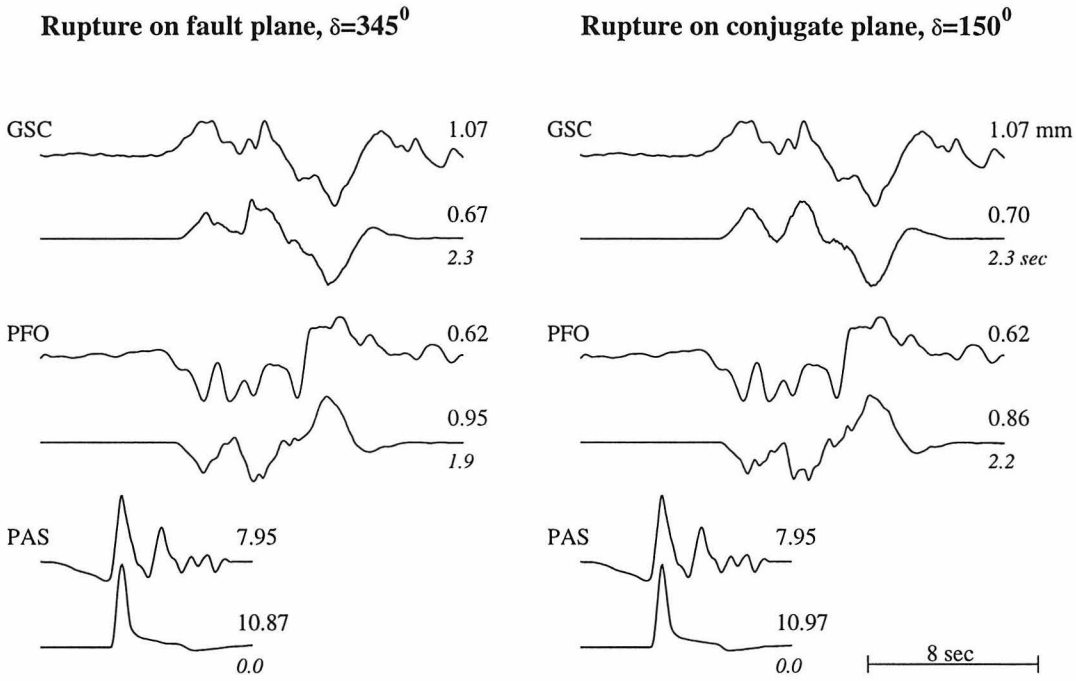

Figure 5.10: Comparison between data and synthetics for stations GSC, PFO and PAS. The fault size is $3 \times 3km^2$. A seismic moment of 3.1×10^{24} dyne·cm are used for synthetics, as determined in the modeling process. Seismogram amplitudes are given in mm and the time shift between data and synthetics are given in seconds.

roughly westward in this case. In the neighborhood of this direction, the effects of the regional records become important.

5.5 Discussion and Summary

In the study of finite faults, many parameters are involved. In the above tests, we used simple square faults with fault orientation and rupture velocity fixed. Slip on the fault was also assumed to be uniform. In reality, one can either rely on other types of data to constraint parameters such as fault orientation, total seismic moment and rupture velocity, or one can develop more sophisticated inversion schemes to invert for these parameters together with the slip distribution. Considerable effort on the study of slip asperity has been made in the last decade [*e.g. Hartzell and Heaton*, 1983; *Wald*, 1992]. With the approximations discussed in this paper, the inversion for the weighting factors w_j of individual sub-faults (point-sources) in equation 5.4 can be made faster.

For the Sierra Madre earthquakes, we were not able to discern the fault plane from its conjugate plane. Our experiments indicate that the vertical component of the directivity, *i.e.*, updip or downdip rupture is not well constrained with regional records. This is partially due to the fact that regional rays usually have large take-off angles which make them less sensitive to vertical component of the rupture (*e.g.*, S, S^{ss}, SdS, Figure 5.3). The rays SmS and $sSmS$ would have the most power to resolve updip or downdip rupture, but the interplay between the down-going phases such as SmS and up-going phases such as direct S and S^s (Figure 5.3) makes it more difficult to detect. Local data is more sensitive to the rupture direction for a given fault size, but adding just one local station (PAS) did not solve the problem. In the last experiment, the preferred rupture direction is westward and downdip on the fault plane or westward and updip on the conjugate plane. Note for a thrust or normal event, the fault plane and its conjugate plane have similar strike directions. When both planes have medium dip angles, which was the case for the 1991 Sierra Madre earthquake, this type of source mechanism is intrinsically more difficult, compared to

other types of mechanisms, for any method using far-field data to distinguish rupture on fault plane or on its conjugate plane. With better station coverage and improved Green's functions, the situation should improve.

It is well known that the seismogram amplitude is a very important piece of information to use in study of the source directivity [*e.g. Kanamori et al.*, 1992]. As discussed earlier, the amplitude ratio between the data and synthetic varies significantly from station to station (Figures 5.7 and 5.10). Rupture on finite faults predict these ratios better than does the point-source. However, any significant station bias on the seismic moment would obscure the picture. In a study of the Landers sequence, *Jones* [1995] reported that the long-period seismic moment for station GSC is consistently greater (by 20 percent) than for PFO. *Song and Helmberger* [1997] also noticed similar phenomena in their source study of the Northridge aftershocks. Thus, to reliably use the amplitude information in directivity studies, such station bias needs to be established. Fortunately, with the expanding broadband network, it will become possible to calibrate such effects for individual stations.

In summary, we developed a numerical method based on the generalized ray theory to efficiently calculate synthetic seismograms from complex finite faulting processes. The approximations in this method are justified when the fault dimension is small compared to the source-receiver distance and when the structure around the source region is relatively simple so that the whole rupture region resides in a constant velocity layer. This method is applied in a grid-search approach to estimate the finite source characteristics of the 1991 Sierra Madre earthquake with simple source models. Our results indicate westward rupture with a fault dimension of about 3 km, which are generally consistent with those of *Wald* [1992]. Local data also proved usable and were particularly useful in our experiments.

Acknowledgements

We thank Craig Scrivner, Jennifer Scott, and Laura Jones for their reviews of the manuscript. Chuck Ammon and Jeroen Ritsema provided critical reviews along with very helpful suggestions. This research was supported by the Department of Defense and was monitored by the Air Force, Office of Scientific Research, under the contract F49620-93-1-0221, and by SCEC #645080 as funded by NSF 8920136. Contribution No. 5480, Division of Geological and Planetary Sciences, California Institute of Technology, Pasadena, California.

Chapter 6 Pseudo Green's functions and waveform tomography

6.1 Abstract

Retrieving source characteristics for moderate-sized earthquakes in sparsely instrumented regions has been made possible in recent years, through the modeling of waveforms at regional distances. The techniques used in such studies model waveforms successfully at long period, using Green's functions for simple 1-D crustal models. For small earthquakes ($M < 4$), however, long period signals are usually noisy and modeling short-period waveforms requires refined Green's functions such as used in the empirical Green's function approach. In this article, we present a new technique that generates such Green's functions by perturbing individual generalized ray responses calculated from a 1-D model. The model is divided into blocks and velocities in the blocks are allowed to vary, which shifts the arrival time of the individual rays similar to conventional tomography. The amplitudes of the rays are perturbed independently to accommodate local velocity variations in the structure. For moderate-sized earthquakes with known source mechanism and time history, the velocity variation in each block and the amplification factor for individual rays can be optimized using a simulated annealing algorithm. The resulting modified Green's functions, Pseudo Green's functions, can be used to study the relative location and characteristics of neighboring small events. The method is also useful in retrieving 2-D structure, which is essentially waveform tomography.

6.2 Introduction

Many earthquakes have occurred in Southern California since the introduction of the TERRAscope array. Nearly 400 events have been recorded broadband with magnitude greater than 3.5. Techniques for inverting long-period data to obtain first order source parameters such as mechanism, depth and moment have become well developed, *e.g.*, *Dreger and Helmberger* [1991a], *Ritsema and Lay* [1995], *Zhu and Helmberger* [1996b]. These techniques model waveforms successfully at long period, using Green's functions for simple 1-D crustal models. Currently, these efforts are limited to earthquakes with magnitude greater than 4.0. The nature of the difficulty can be seen by comparing the recordings of a typical earthquake sequence of different magnitude. Figure 6.1 displays broadband and long-period records of the 1991 Sierra Madre earthquake and two of its aftershocks (Figure 6.2). As can be seen, long-period noise tends to overwhelm the signal at about magnitude 4. To study small events, it is necessary to avoid long-period signals in the broadband recordings and model shorter-period waveforms. Doing this requires refined Green's functions.

One of the applications, or usefulness, of point-source parameters is to fine-tune the propagation model involved and further investigate structure heterogeneity. The method of *Zhao and Helmberger* [1994], further improved by *Zhu and Helmberger* [1996b], is a natural approach towards this goal. This method matches observed seismograms against synthetics over discrete wave-trains and allows relative time shifts between individual wave-trains, *e.g.*, the P_{nl} wave-train and the Rayleigh wave (hence the name "cut and paste"). This allows a better correlation between data and synthetic waveforms. One example of this method being applied to the 28 June, 17:00, 1991 Sierra Madre aftershock (Figure 6.2) is shown in Figure 6.3. The upper panel shows the source inversion using long-period records from stations GSC, PFO and ISA. Synthetics at station SBC are predictions with the resulting source mechanism. The lower panel displays the predicted broadband synthetics at all four stations. The waveforms are well-matched, especially the long period records at stations GSC, PFO and ISA. The SV waves are used together with the Rayleigh waves and the latter

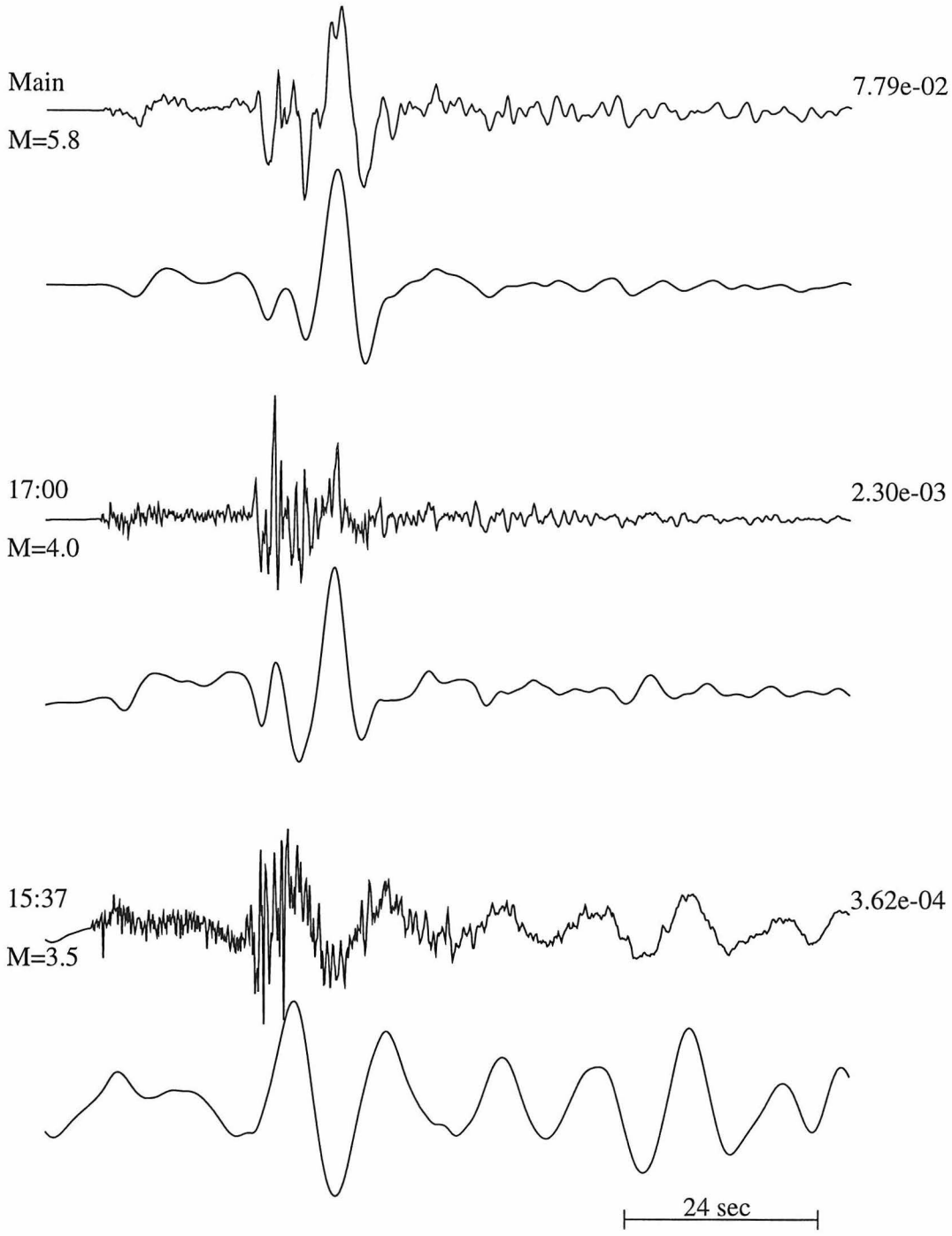

Figure 6.1: Comparison of broad and long-period data for the 1991 Sierra Madre sequence. The top pair of traces show the recording at station GSC for the 1991 Sierra Madre mainshock, with the upper trace broadband and the lower trace filtered with a long-period Press-Ewing instrument response. The next two pairs display the comparison for two aftershocks.

dominates the comparison between the data and synthetics, as seen in the complete radial and vertical components (Figure 6.3). However, it seems that a small timing perturbation would bring the SV synthetics into alignment with the observation (*e.g.*, station ISA). This is more clearly seen on the vertical components (Figure 6.3, lower panel). These time shifts, together with those for the P_{nl} waves, the Love waves and the Rayleigh waves, are indicative of further adjustment of model velocities, as discussed in Chapter 2. However, all these time shifts may not be satisfied with adjustments to a 1-D model. Furthermore, timing perturbations on individual arrivals would fit the data to a higher level of detail and would even fix the problems for station SBC (Figure 6.3). One immediate question that follows such observations is how to adjust the velocity structure to achieve these fine timing perturbations. Or, if this question turns out to be too difficult to answer for some cases, is it possible, from a practical point of view, to perform such perturbation and make use of the resulting high resolution Green's functions? The article tackles the above questions.

High resolution Green's functions are useful and necessary to study the initiation process and source complexity of large events. For these purposes, we have resorted to empirical Green's functions [*Hartzell*, 1978]. However, the application of empirical Green's functions is limited by many factors, such as source mechanism and location. Thus, our success in recovering higher order parameters such as rupture properties have been limited, largely due to the inability to correct for propagational effects at short periods. In other words, we have not been able to exploit the broadbandness of the TERRAscope data routinely because of the lack of quality broadband Green's functions.

In this article, we present a new technique that generates such Green's functions, or pseudo Green's functions (pGf) as we call them. Pseudo Green's functions are less dependent on source-mechanism and can be adjusted for small difference in source location. The technique is tested on the Sierra Madre earthquake of 28 June 1991 and its two aftershocks on the same day (Figure 6.2). The Pseudo-Green's functions obtained from the $M_L = 4.0$ aftershock at 17:00 GMT are used to model a smaller aftershock of $M_L = 3.5$ at 15:37 GMT. These events are chosen because they occurred

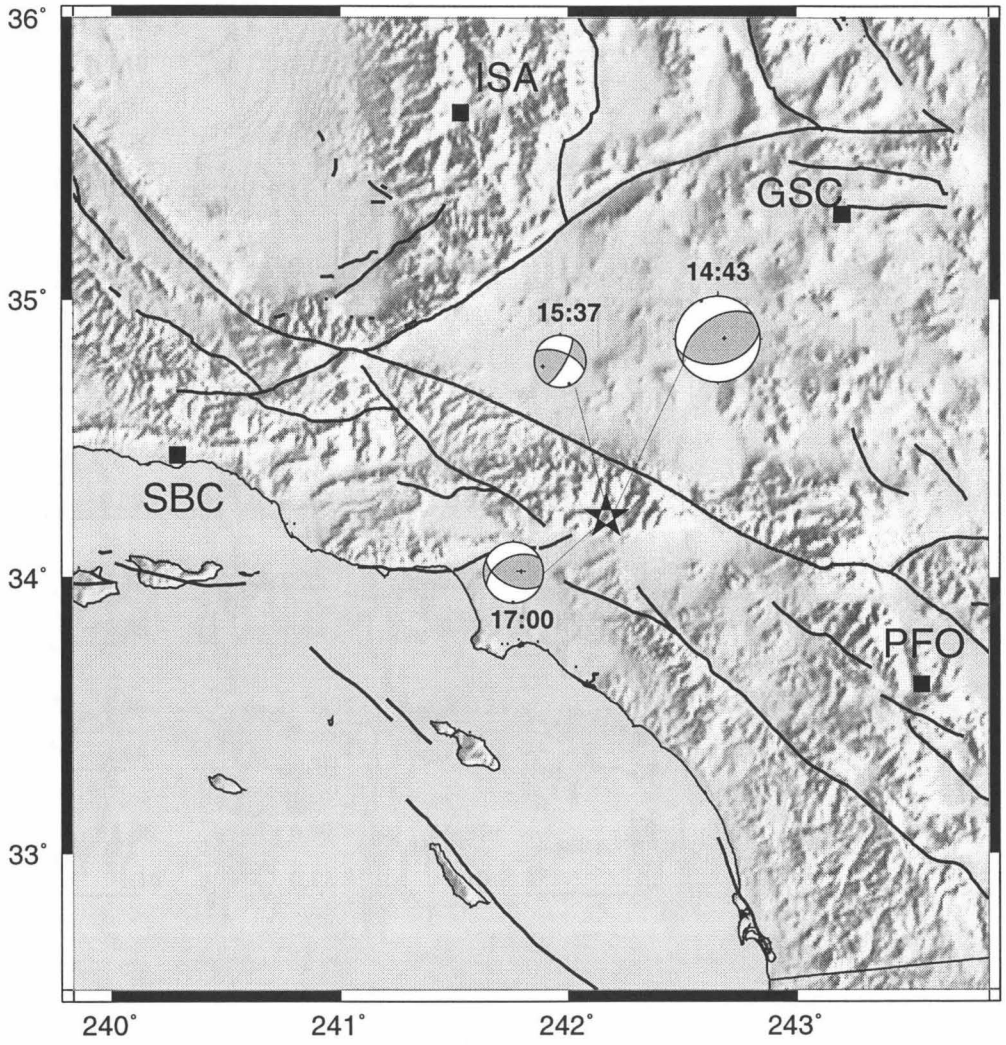

Figure 6.2: Topographic map of Southern California and epicenters and source mechanisms of the Sierra Madre mainshock and its two aftershocks. Also shown are the locations of four TERRAscope stations used in this study.

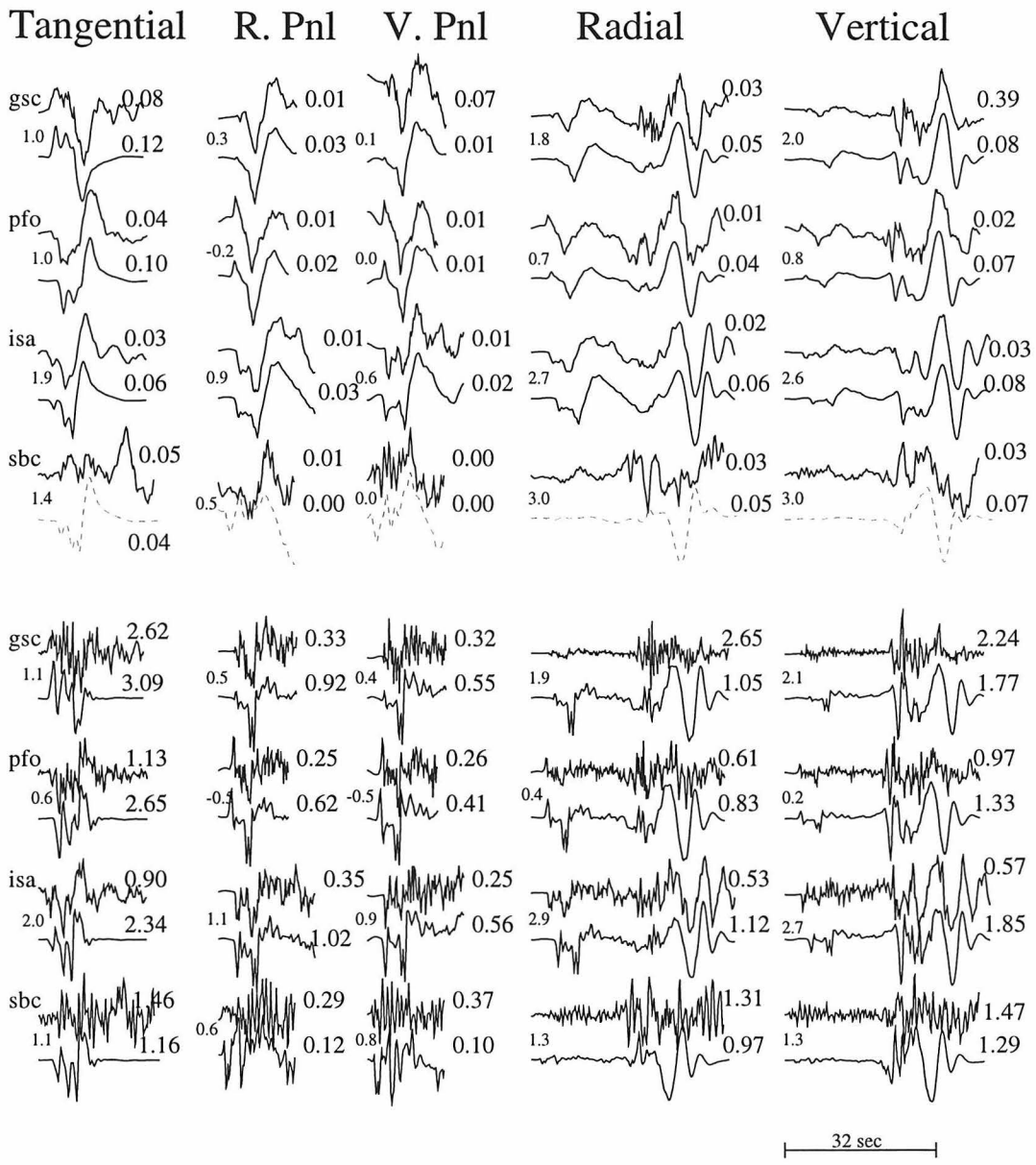

Figure 6.3: Comparison of data and SC synthetics for the Sierra Madre aftershock (17:00). The upper panel shows the result of the source estimation process with stations GSC, ISA and PFO. A source mechanism of $(244^0, 48^0, 51^0)$ is obtained, with a source time function of (0.2, 0.3, 0.2 sec). The P_{nl} waves are enlarged and shown separately, as they are processed in the inversion routine. Synthetics at station SBC are predictions with the result source mechanism. The lower panel show broadband predictions of the SC synthetics with the source mechanism derived from the long-period data (upper panel). Peak amplitudes are shown at the end of each trace. Small numbers indicate time delay of synthetics relative to data. After *Zhao and Helmberger* [1994].

in the middle of a dense array and occurred within 2 km of each other [*Hauksson*, 1994]. Previous studies [*e.g. Dreger and Helmberger*, 1991a; *Zhao and Helmberger*, 1994; *Hauksson*, 1994] provide essential informations needed in our experiments, *e.g.*, source location, depth, mechanism and source-time function. Application of the pGf technique in waveform tomography is also discussed.

6.3 From eGf to pGf – the pGf method

From the Generalized Ray Theory [*Helmberger*, 1983], a synthetic seismogram consists of a series of ray responses that describe energy packets arriving at the receiver along various paths. The travel-time of an individual ray is controlled by the integral slowness along its path. A mild perturbation of the 1-D model usually preserves the shape of the ray responses [*Song et al.*, 1996]. This is demonstrated in *Stead* [1990], where he conducted finite-difference computation of a set of similar 2-D models (Figure 4.13). The amplitudes of the ray responses, however, are more sensitive to the velocity perturbation and usually depend on very local changes in the model.

The method we describe in this section resembles the conventional travel-time tomography in that travel-times of individual rays are connected to a slowness model, which consists of discrete, constant slowness cells. Besides modeling the travel-time of the first arrival, all important pulses on a seismogram are taken into consideration. These travel-times (t_0's of the generalized rays) are fit by matching the waveform data with the total synthetics ($S(t)$), which is the sum of all the individual ray responses ($R(t)$), after being shifted by dt and amplified by a factor A:

$$S(t) = \sum_i A_i(t) R_i(t) * \delta(t - dt_i). \tag{6.1}$$

In the above equation, i is the index to the rays and "*" denotes time-domain convolution. Convolution with the δ function in 6.1 corresponds to a time shift. The ray response $R_i(t)$ is computed from a reference 1-D model. The time shift dt_i is

formulated as in conventional travel-time tomography:

$$dt_i = \sum_j l_{ij} ds_j, \tag{6.2}$$

where ds_j is the velocity perturbation to block j and l_{ij} is the length for which ray i travels in block j. To minimize the effect of the amplitudes of the ray responses on fitting the travel-time, A_i's are allowed to change freely over a restricted range. This freedom in the parameterization also serves to obtain practical Green's functions, or the pseudo Green's functions, as will be discussed later.

Unlike the conventional travel-time tomography which usually features linearized inversion, our pGf technique takes a forward approach. A set of optimal parameters, the slowness perturbation in the model blocks (ds_j) and the amplification factor (A_i) for individual rays, are determined using a simulated annealing algorithm. The simulated annealing algorithm has been introduced in recent seismological studies, *e.g.*, *Sen and Stoffa* [1991], *Ammon and Vidale* [1993], and *Zhao and Frohlich* [1996]. *Zhao and Frohlich* [1996] described a modification and optimization of the simulated annealing algorithm, which is used in this exercise. In our application of this algorithm, we utilize a misfit function that is the least-square error between the data and the synthetic. This function is minimized as the optimal parameters are approached.

After a set of optimal parameters (ds_j, A_i) is found, the time shifts of the rays (dt_i) are computed again from the optimal velocity perturbation (ds_j) with equation 6.2. These optimal time shifts, together with the optimal amplification factors (A_i), are applied to the original 1-D impulse ray-responses to generate the pseudo Green's functions for the fundamental fault system, which consists of strike-slip, dip-slip (90^0 dip), and 45^0 dip-slip orientation.

Figure 6.4 shows an example of the pGf technique being applied to the 1991 Sierra Madre mainshock and the big aftershock (17:00), as recorded at station GSC (Figure 6.2). In this experiment, the standard Southern California model of *Dreger and Helmberger* [1991a] is used as the reference model (Table 5.1. Green's functions are combined with the source mechanism, source-time function and seismic moment

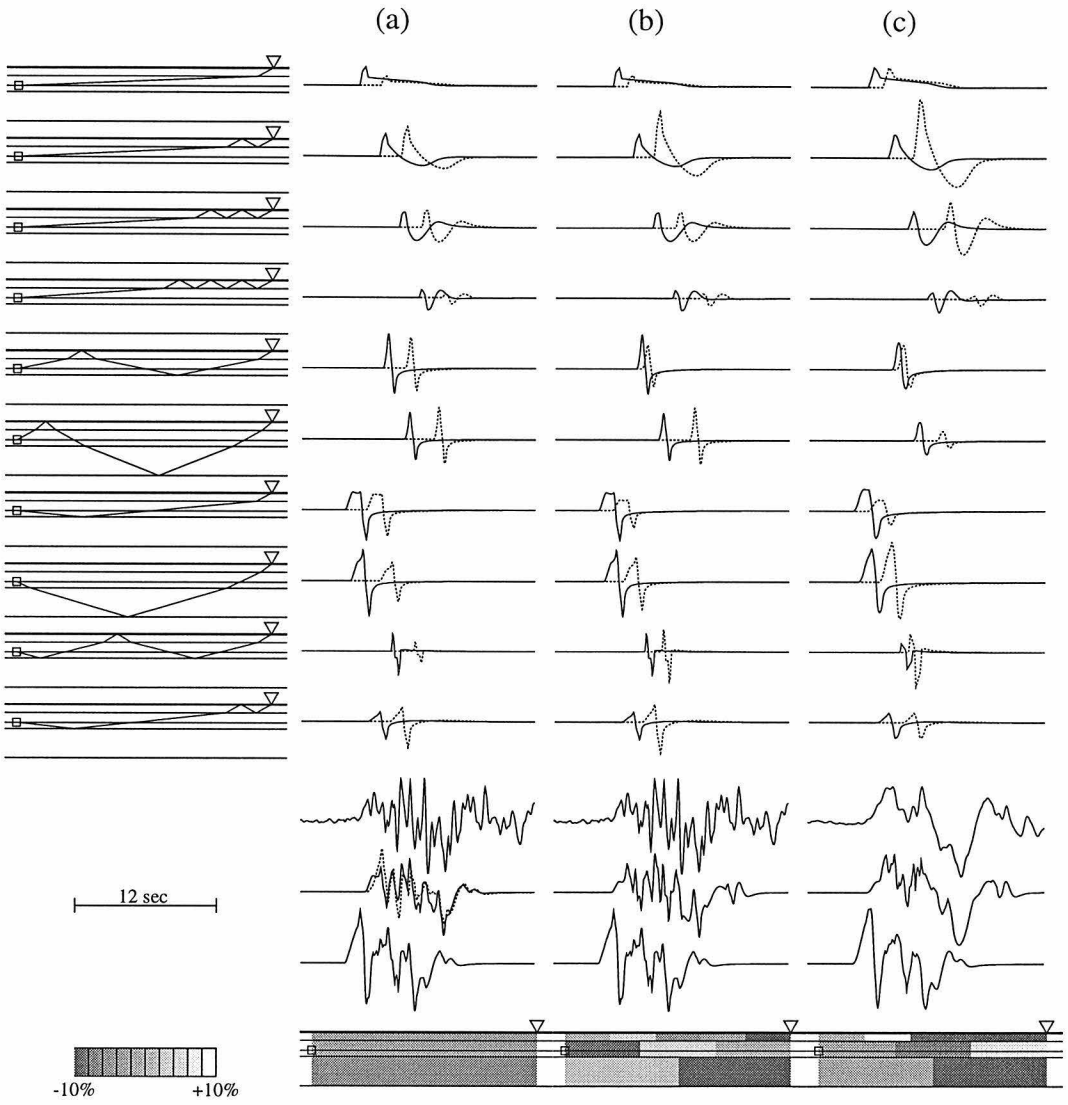

Figure 6.4: The pGf procedure used in generating pseudo Green's functions for the path from Sierra Madre to station GSC. The leftmost column shows the individual ray paths corresponding to the point-source responses shown to the right. Columns (a) and (b) are for the big aftershock (17:00) and column (c) is for the mainshock (14:43). Note column (a) allows only 1-D velocity changes, while in columns (b) and (c), the model is divided into 10 blocks. The lower three sets of seismograms (solid traces) contain the data, the pGf simulation, and the SC synthetic (bottom traces). The dotted trace in the lower panel in column (a) is the new 1-D synthetic for the model shown at the bottom of the same column. Point-source solution of *Zhao and Helmberger* [1996] is used.

of *Zhao and Helmberger* [1994] for both events to generate the original 1-D ray responses. In this figure, individual ray paths and responses are shown only for the most important rays, while the total synthetics contains a total of 14 rays. These rays comprises a sufficient ray set to match the complete synthetics as generated by the reflectivity method [*Saikia*, 1994b]. All seismograms are plotted in absolute time with the same amplitude scale. In column (a), each layer of the original 1-D model (SC) is perturbed as a single block. This setup has the minimal freedom in terms of fitting the travel-times. As a result, the onset of the simulation, that is, the sum of the rays after shifting and amplification, is slightly off, as compared to the data. The overall waveform, however, is well matched. If we take the resulting model, shown at the bottom, and compute 1-D synthetics for it, the new synthetics would be the trace shown superimposed on the perturbation result in lower panel. This comparison of the two synthetics demonstrates the goodness of the time-shift approximation. The strength of the pulses on these two synthetics does not match exactly and we picture the amplification effect as a result of many other factors, including source complexity and very local variation in the model, which we do not intend to model in this example. Column (b) displays another test on the aftershock. This time, the SC model is divided into 10 blocks, the slowness of which can vary independently. As a result of more freedom, the resulting simulation match the data better than in column (a). In Column (c), the same experiment is conducted using the mainshock data recorded at station GSC. As can be seen in the comparison of columns (b) and (c), the time shifts for most of the rays are consistent for the two events. However, the corresponding slowness models show a substantial difference. This brings up the non-uniqueness problem in the procedure in producing the required travel-time shifts.

In Figure 6.5, a set of experiments, showing a spectrum of parameterization schemes, are displayed for four station GSC. In general, as the starting model is divided into more blocks, the waveform fits is improved, but the corresponding models for different events show greater difference. The dotted traces show a case where the time-shifts of the individual rays are not connected by any physical model. The simulations fit the data almost exactly, but there is no way of transporting the op-

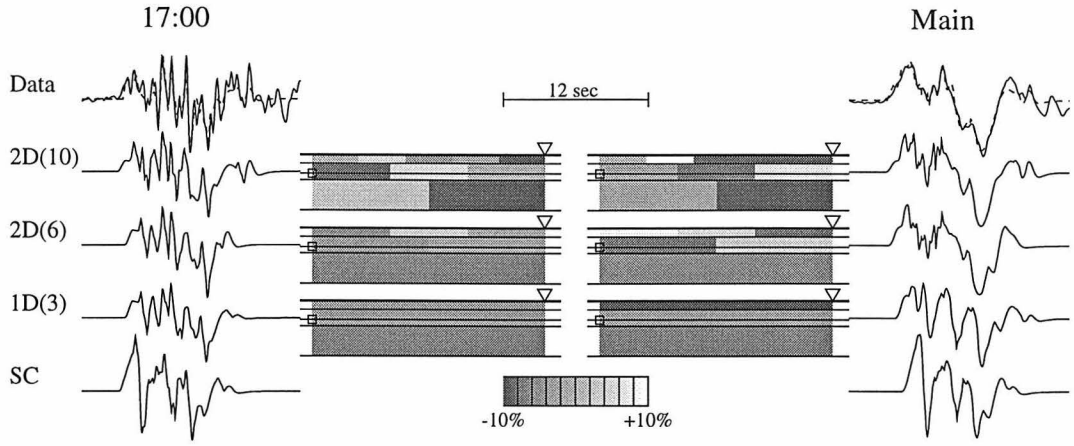

Figure 6.5: Data and simulations with different schemes of model division in the pGf procedure. Tangential component of broadband displacement data at station GSC is used. The results for the mainshock (right) and those for the aftershock (left) are compared. The original 1-D SC synthetics are shown at the bottom.

timal parameters from event to event. In the rest of our experiment, we choose to divide the model into 6 blocks since this setup seems to generate reasonable synthetic fits as well as model stability.

6.4 Application to the Sierra Madre aftershocks: pseudo Green's functions

We applied the above procedure to paths from Sierra Madre to stations GSC, ISA, PFO and SBC, using the tangential component of the broadband displacement data from the big aftershock (17:00). The aftershock data is used instead of the mainshock because presumably it is less contaminated by source complexity. Figure 6.6 shows the comparison between the data, the simulation and the original 1-D SC synthetic. The simulations fit the data well for all stations. Station SBC show great improvement over the original 1-D synthetics. The resulting models for different paths are different, but all display low-velocity in regions near the source.

Again, if we apply the time shifts (dt_i) and amplification factors (A_i) found in the above pGf procedure to the original 1-D impulse ray-responses for the basic faults,

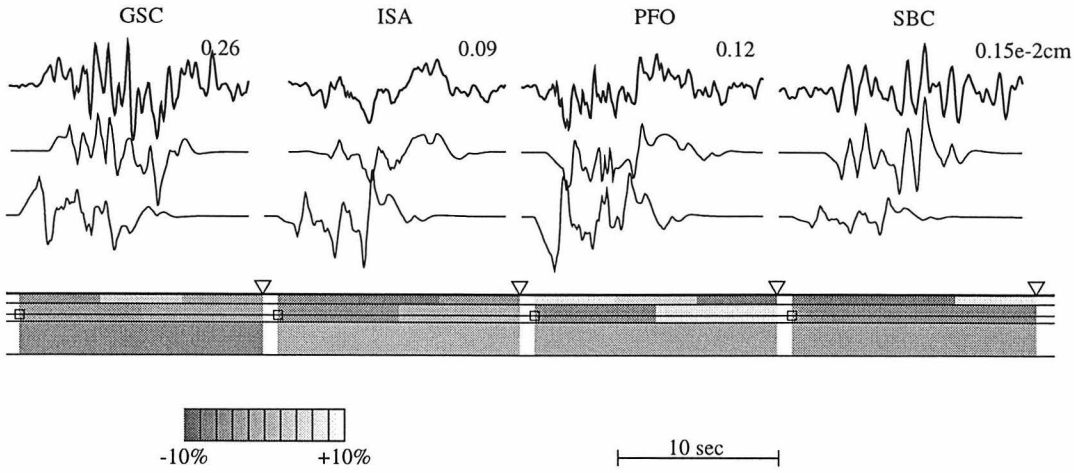

Figure 6.6: pGf simulations (middle traces) and the associated 2-D models from Sierra Madre to four TERRAscope stations. Tangential component of broadband displacement data (top traces) from the big aftershock is used. The SC model is used as the starting model for all paths. The point-source solution of *Dreger and Helmberger* [1991a] is used. The original 1-D SC synthetics (bottom trace) are also shown for comparison.

we obtain pseudo Green's functions as shown in Figure 6.7 for the path from the big aftershock to station SBC. These responses are fine-tuned, *i.e.*, time-shifted and amplified, in the above process to suit this particular path.

In Figure 6.5, we have seen some similarities between the models derived for similar paths using the aftershock data and using the mainshock data. This suggests similar time shifts are involved for the ray responses in the resulting pGf simulations. One immediate question is how the pseudo Green's functions derived from one event can be used to model another neighboring event. The most straight forward application that can answer this question is to invert a closely located small event for the source mechanism. Again, we choose a close and small event to avoid further special handling on the pGfs before they can be applied. To this end, we choose the small aftershock (15:37) which is located within 2 km of the big one [*Hauksson*, 1994]. Figure 6.8 shows the source inversion result for this small aftershock (15:37) with the method of *Zhao and Helmberger* [1994]. In this inversion, the tangential component of the broadband displacement data is modeled using the pGfs derived in the above test using data from the big aftershock (17:00). Broadband waveform data for event of

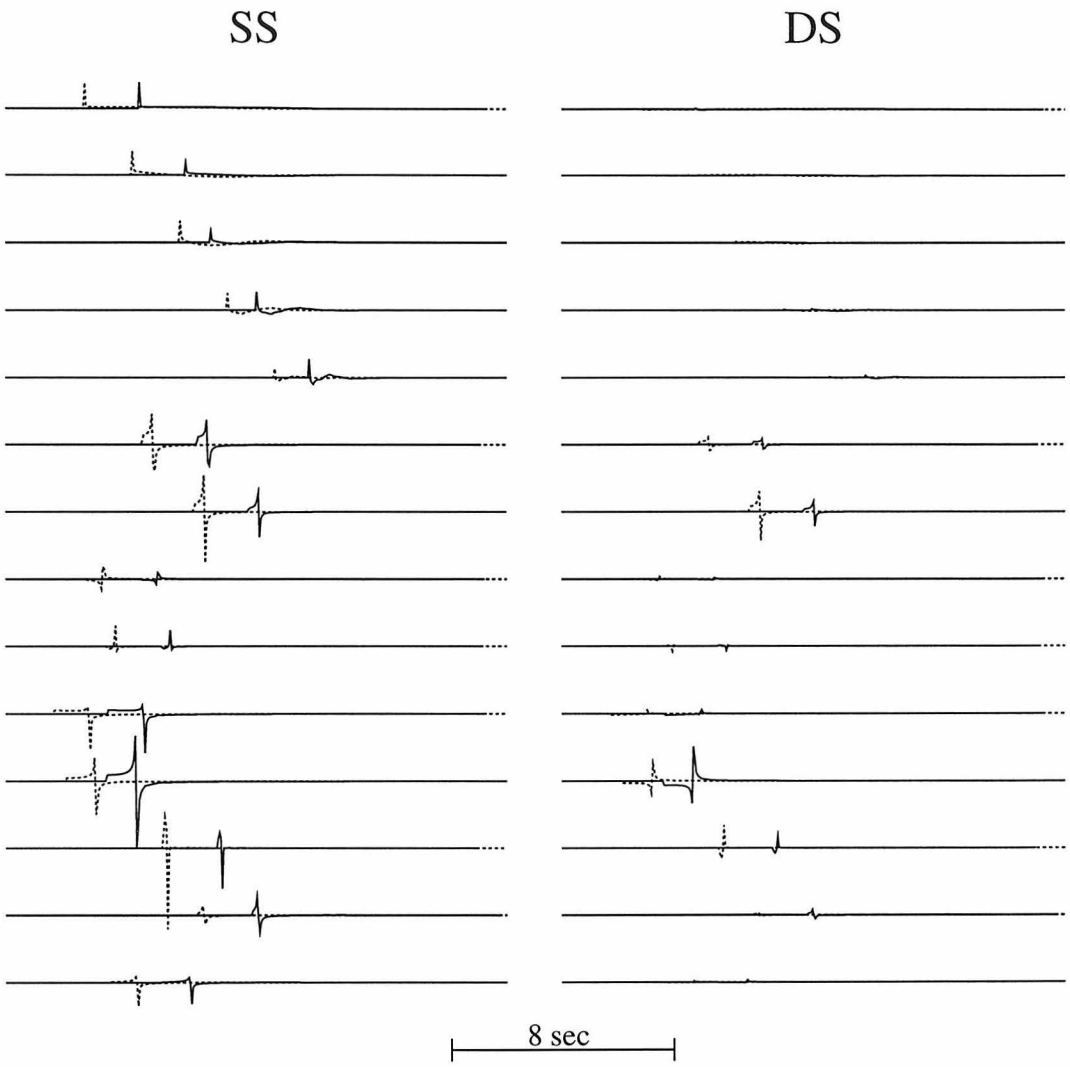

Figure 6.7: Strike-slip (left) and Dip-slip (right) impulse ray-responses (solid traces) that form the pseudo Green's functions from the big aftershock (17:00) of Sierra Madre to station SBC. The dotted traces are the original 1-D SC Green's functions.

this size (M_L=3.5) can be difficult to use for inversion of source mechanism if the relative timing between different high-frequency-rich phases (*e.g.*, $sSmS$ and SmS) in the Green's functions is off, which is the case for the 1-D SC synthetics. The pseudo Green's functions seem to do well in this respect for all four stations. Station SBC is usually problematic when modeling events from the east, due to the complex propagation effect associated with the basins along the path. However, stations in this azimuth are critical to the modeling of events in the Los Angeles region because there is already a gap in the distribution of stations to the southwest due to the Pacific ocean. With the pseudo Green's functions, the waveform fit to station SBC is satisfactory (Figure 6.8) and we see some hope for making good use of this critical station, or, in general, stations in this azimuth.

We notice that there are problems in the waveform fit in Figure 6.8, *e.g.*, at stations PFO and GSC. The late part of the record at station PFO is fit reasonably well, but there is problem with the front, which we believe has more to do with the data quality than the pGfs. For station GSC, however, the phase $sSmS$ on the synthetic is too strong when compared to the data. A tentative explanation for this is that the big aftershock occurred on a northeast-dipping thrust fault and probably ruptured upward, which strengthened the $sSmS$ arrival from the big aftershock, especially at station GSC. In other words, when the pseudo Green's functions were generated, they already have in them a source directivity that is not in the small aftershock. One remedy to this is to simultaneously invert multiple well-located events and average out the effect of source directivity on the arrival time.

6.5 Application to the Tibetan profile: waveform tomography

The pGf technique is an effective means to fine-tuning 1-D models per path (Figure 6.4). A 2-D model associated with a pseudo Green's function, however, can be viewed in different ways. For regional shallow events, as the Sierra Madre earth-

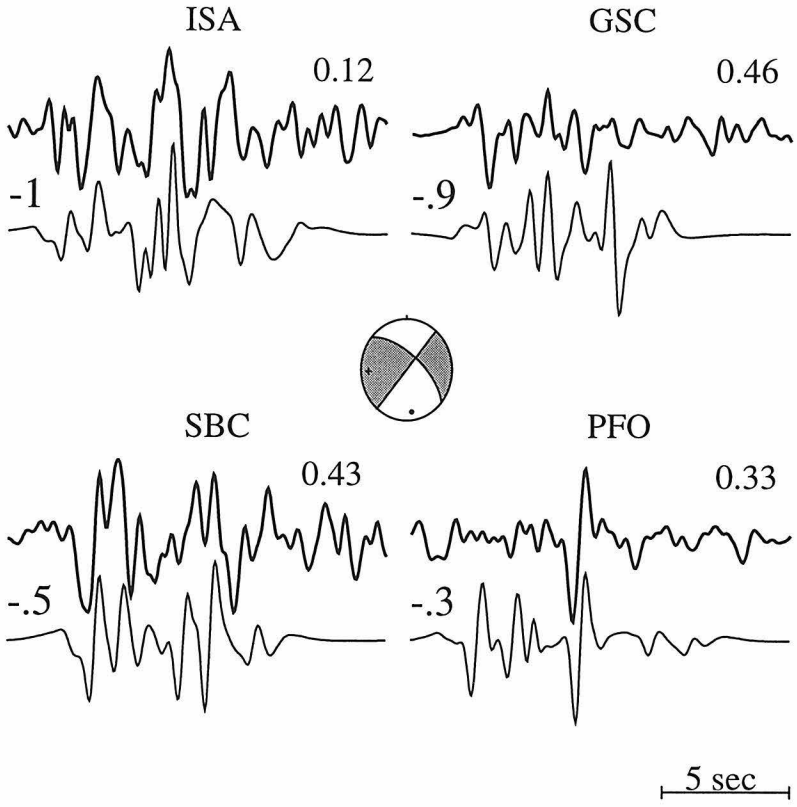

Figure 6.8: Comparison of the tangential component of the broadband displacement data of the small aftershock (15:37) and the simulations with eGfs derived using data from the big aftershock (17:00) for the same paths. The best-fitting source mechanism, shown at the center, and a source-time function of (0.2, 0.1, 0.2) sec are used to produce the simulations.

quakes in our example, there are usually two or three layers in the crust model and about a dozen rays contributing to the total response. The interference between these rays control the synthetic waveform. If we let the arrival time of the individual rays change freely, the waveform data can be simulated almost exactly, as shown in Figure 6.5. However, there is tremendous non-uniqueness in this process. Associating the arrival times of the contributing rays to a physical 1-D or 2-D model helps resolve this layer of non-uniqueness. Note that even when a model is used, there still exists non-uniqueness in the problem since obviously more than one model can produce the same or very similar set of time shifts. In our test, this layer of non-uniqueness has been reduced by choosing the most feasible model division scheme.

For upper mantle events, very few rays (3 or 4) often dominate the synthetic waveform. Moreover, the interference between these rays is often minimal. When a profile of records from an earthquake with well-determined source mechanism is inverted using our pGf technique, the resulting 2-D model can be indicative of the structure along the studied profile.

One such profile in the Tibet plateau is shown in Figure 6.9 where several shallow and intermediate depth earthquakes are recorded by a set of broadband three-component seismic recorders in a PASSACAL experiment jointly conducted by the Institute of Geophysics, State Seismological Bureau, China, the University of South Carolina, and the State University of New York at Binghamton. This profile has been well studied by *Zhu et al.* [1993] and *Zhu et al.* [1995] for the source mechanisms and for the crustal structure. The crustal model established by *Zhu and Helmberger* [1996b] is similar to that of *Romanowicz* [1982] and is suitable for modeling long period waveforms for this region. With this model, they were able to constrain the source mechanisms of these events, using the method of *Zhao and Helmberger* [1994]. Figure 6.10 displays 1-D synthetic fit to the SH data along the profile, using the point-source solution and the crustal model of *Zhu and Helmberger* [1996b]. An anatomy of the synthetics using generalized rays show that they are dominated by only 3 to 4 arrivals, 1 or 2 for near in stations (Figure 6.10, lower panel). These rays are separated in arrival time and the interference between them is minimal, which makes a

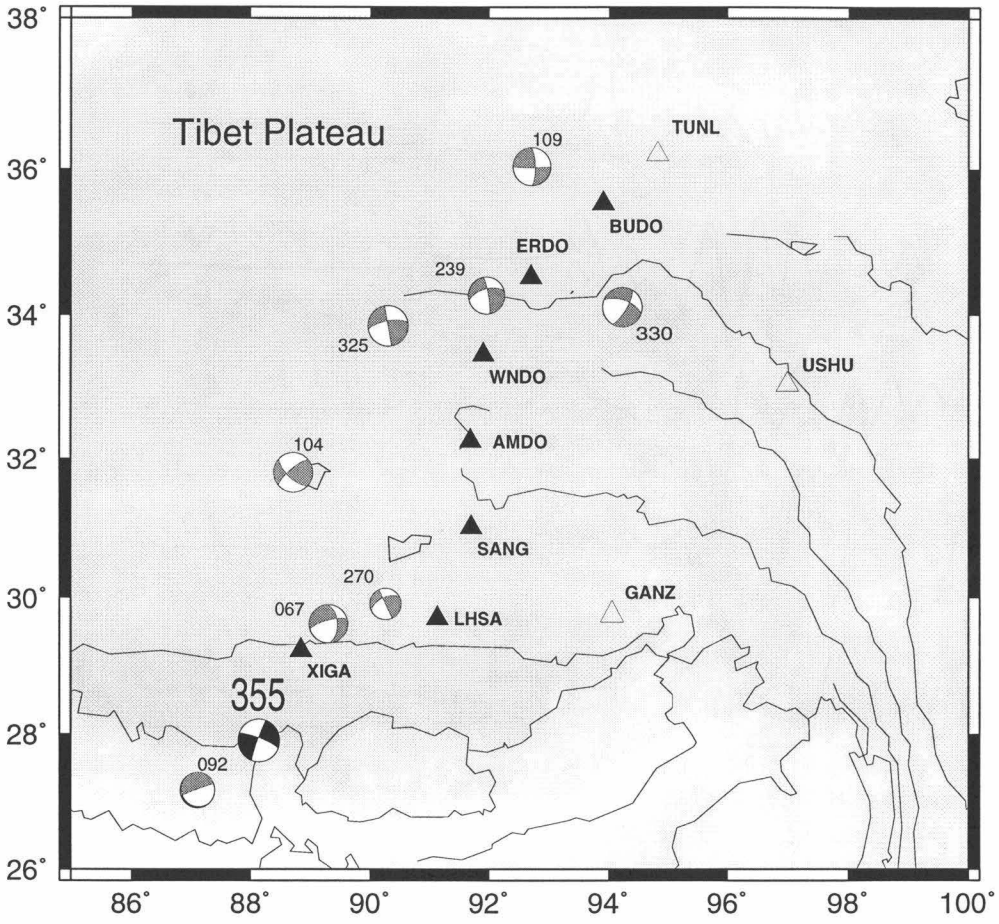

Figure 6.9: Topographic map of the Tibet plateau and a profile of broadband stations. Stations used in this study are represented as solid triangles. Some of the earthquakes recorded by these stations are shown with their locations and source mechanisms. Event 355, which is used in this study, has an estimated depth of 70 km. After *Zhu and Helmberger* [1996a].

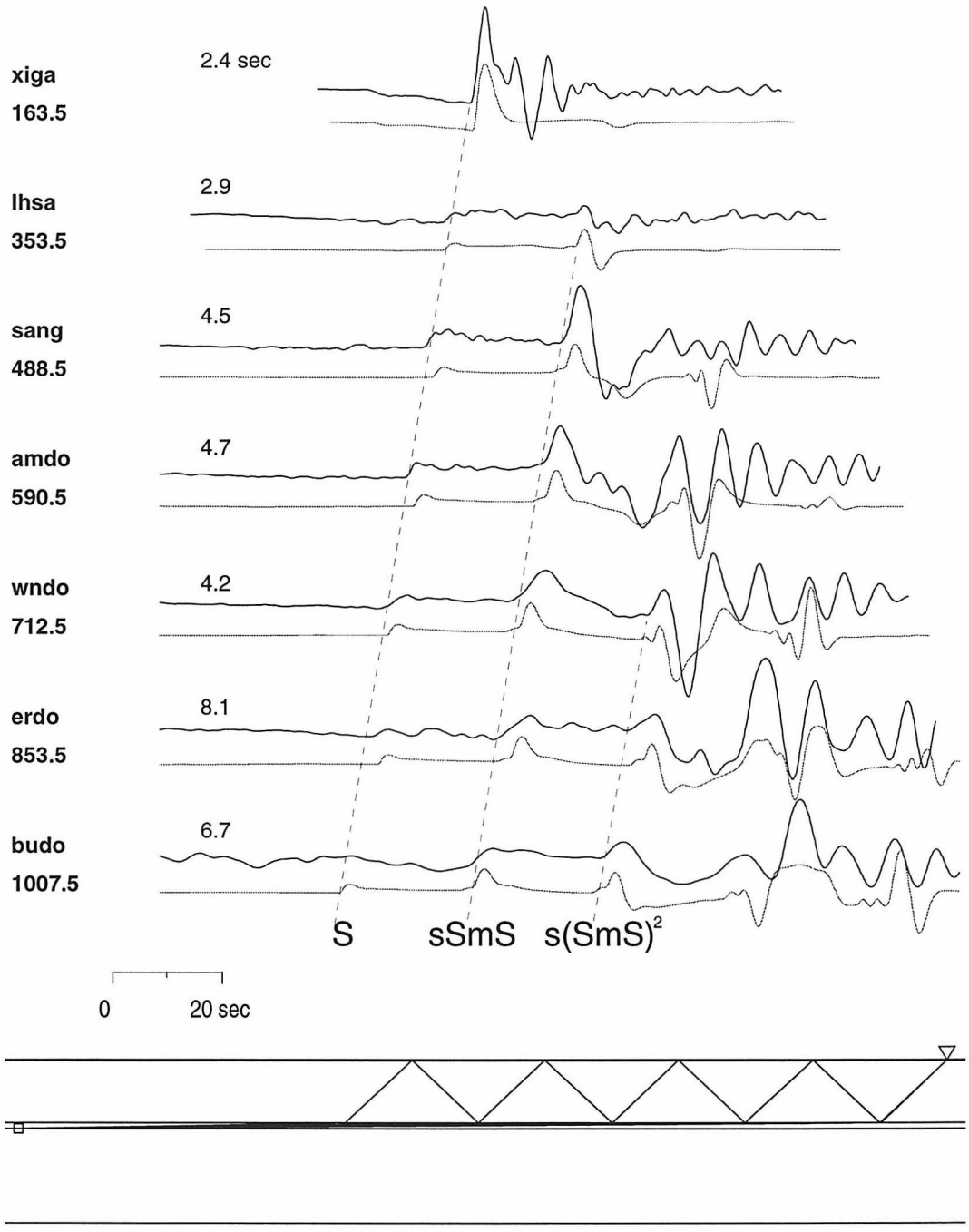

Figure 6.10: Comparison of SH Data (heavy traces) and 1-D synthetics (light traces) for event 355 and a profile of stations. The mechanism used is shown in Figure 6.9 (event 355), with a trapezoidal source-time function of (.5, .2, .5 sec). Dash lines indicate three arrivals. Note the first down-swing at station xiga is a near field effect. Model s-velocity is 3.5 km/sec in the crust and 4.7 in the mantle. Crust thickness is 65 km. Both data and synthetic are low-pass filtered with a corner frequency of 0.2 Hz. After *Zhu and Helmberger* [1996a].

good case for testing the pGf technique for waveform tomography. It is clear from Figure 6.10 that not only the first arrival, but also the later ones, contain important information about the crustal structure. At some stations, the first arrival is at or below the noise level but the second or third arrivals stand out clearly (*e.g.*, station budo). In this comparison (Figure 6.10), the complete synthetics are delayed by the indicated amount to align with the data. After the shifting, the waveform data is fit reasonably well. However, the relative timing between different arrivals needs further adjustment to fit all the important rays in timing. This, and the relative time shift between different stations, are indicative of the fine structure beneath each station and along the profile.

In our next example, this profile of SH data from event #355 is inverted for a 2-D crustal model (Figure 6.11). The point-source solution of *Zhu and Helmberger* [1996b] is used, with their crustal model as the reference model. In the inversion, the source location is allowed to move around within 5 km of what is used by *Zhu and Helmberger* [1996b]. The origin time is allowed to change by up to 2 sec and a station delay of up to 2 sec is allowed for each station. An optimal perturbation to the reference model is shown in Figure 6.11. With these perturbations, the relative arrival times are fit well. Although the absolute velocity in the model trades off with the origin time and probably the source depth, the two low-velocity regions in the new model show consistency with the crustal thickness (Figure 6.9) found in previous receiver-function studies of *Zhu et al.* [1993] and *Zhu et al.* [1995].

In this test, the reference model used has an extremely simple 1-layer crust. Only a few blocks are used in the model and station delays are allowed, in order to fit the arrival times. Another approach would be to use a slightly more complex model, say with a top layer in the crust, and divide the model into more blocks. In either case, better path coverage than what is used in the experiment is required in order to resolve the fine structure along the profile. This can be achieved by adding to the inversion more events, especially shallow ones.

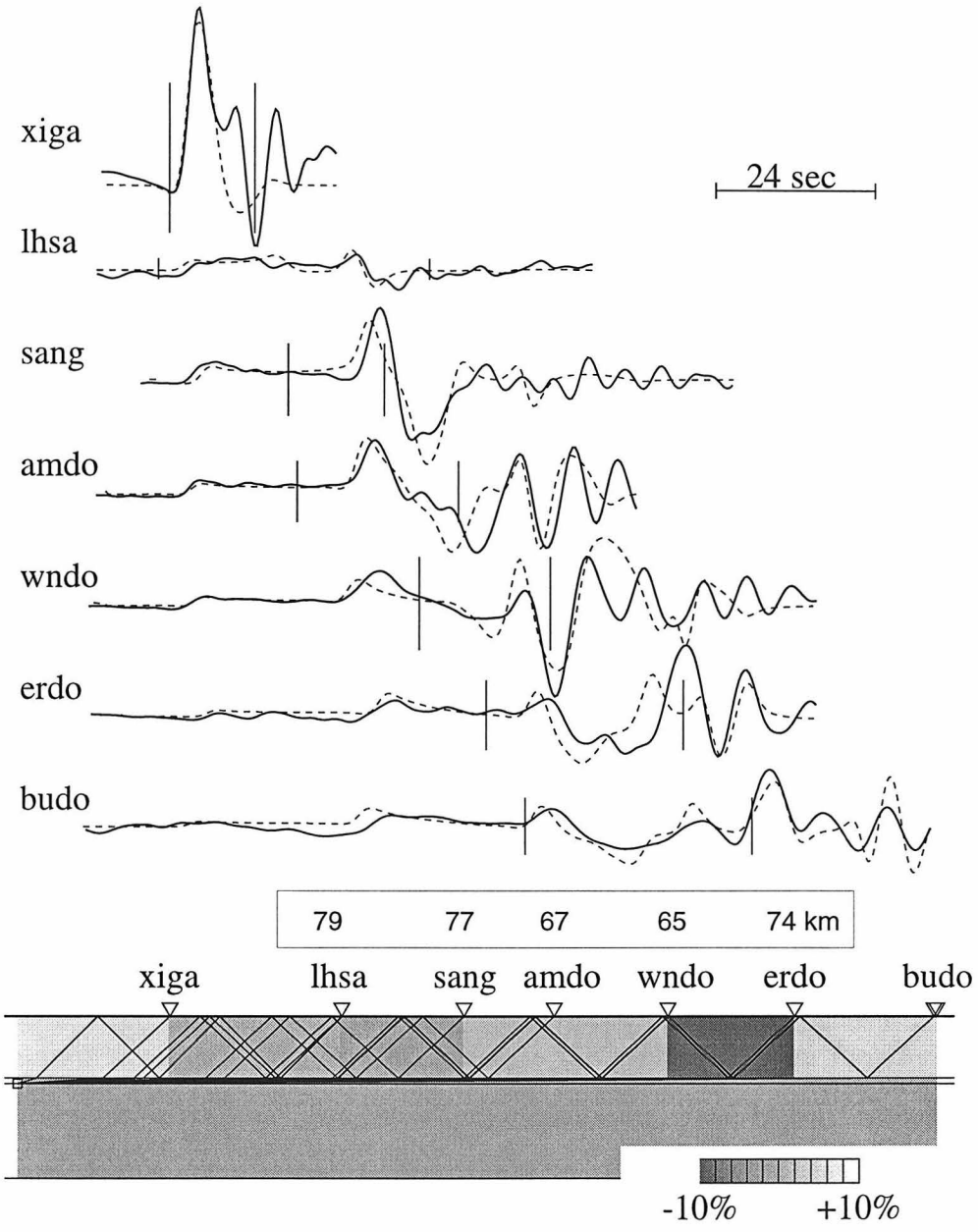

Figure 6.11: SH Data (solid traces) and pGf simulations (dotted traces) for the Tibet plateau. In the inversion, data is weighted with a factor $w(t) = 1$ for $t < t_0$ and $w(t) = e^{\frac{t_0 - t}{t_1 - t_0}}$ for $t \geq t_0$. t_0 and $t_1 (t_1 > t_0)$ are shown as vertical bars in the figure. The weighting is done so that the inversion is not dominated by the large late arrivals. A uniform upper mantle velocity is used in the inversion and the crust is divided into 7 blocks with the boundaries at the stations. Point-source solution of *Zhu and Helmberger* [1996a] is used for this earthquake (event 355). Numbers in the long box show crustal thickness in km, as estimated by *Zhu et al.* [1993].

6.6 Discussion and future work

In the development of the techniques, both in the previous chapter and this chapter, we have concentrated on the tangential component of the ground motion because of its simplicity as compared to the $P-SV$ system. In the future, however, it is possible and necessary to use the full ground motion by employing the three-component data. It is also possible to invert multiple events and multiple stations in a single simulation.

As shown in Figure 6.7, our pseudo Green's functions take the form of a set of impulse ray-responses to the fundamental faults. In the above Sierra Madre example, we simply summed the impulse responses and use the resulting two-component Green's functions (strike-slip and dip-slip) in the source inversion procedure. In reality, if the small aftershock is in the neighborhood of the big aftershock but of some distance away from it, we can further adjust the arrival time of each individual ray-response in the pGfs, with the method discussed in the last chapter, provided both events are well-located. From another point of view, if we have one well-located small event with source-mechanism known, we can invert for the relative location of a group of neighboring events using the pGf technique. Furthermore, if we take the assumption that a big event is a sum of small events, we can study the source finiteness and rupture directivity of big events by accurately locating the relative position and timing of the subevents in a big earthquake.

The amplification factors used to generate the pseudo Green's functions can offer additional information. Cite condition, attenuation, local velocity changes in the model and source complexities all contribute to the changes of the amplitude of a ray responses. Practically, the amplitude factors and the time shifts can be studied separately since many times only one of them is important in the problem. In fact, such separation reduces the number of parameters in the annealing process and effectively speeds up the simulation. In our Sierra Madre test, we have put off the consideration of the contributing source of the amplification factors, since we were mainly interested in getting usable Green's functions. However, because of the nature of the algorithm we use to find the pseudo Green's functions, *i.e.*, the simulated an-

nealing algorithm, it is possible to represent these factors as a combination of the site response and source directivity and invert them simultaneously when searching for the pseudo Green's functions. In our Tibet example, the optimal set of amplification factors allows good fits to the waveforms, but we have not investigated these factors either. One possible way to take these factors into account is to apply the local earth stretching approximation of *Helmberger et al.* [1996] and associate these factors with the transmission and reflection coefficients in the simulation process. With these, the pGf technique would be useful in testing existing 3-D P-wave tomography models and in developing 3-D pictures of S-velocity structure.

6.7 Closing remarks

We have introduced a series of techniques to model regional phases to resolve source characteristics and propagational effects. Our effort has been to improve resolution for the seismic parameters by modeling these phases in a broader frequency band, especially to the high frequency end. We started with 1-D synthetic, which is useful in resolving point-source parameters, and looked into different approaches of obtaining details of the source process. Our empirical Green's function study on the Northridge mainshock showed that regional seismograms are good at resolving the important parameters, *i.e.*, the fault dimension and the rupture direction, of a finite fault. For this purpose, empirical Green's functions are highly useful. To obtain more detailed information about a complex source, the eGf approach encounters difficulties in handling differences in source locations and in source mechanisms. The ray-shifting technique described in the previous chapter, combined with the pGf technique introduced in this chapter, is capable of transferring an empirical Green's function to a pseudo Green's function, which is more flexible. This thesis has focused on the development of the techniques with only a few examples showing their usefulness. However, many of the applications discussed in the last section can be readily carried out and they are indeed part of our ongoing effort. In this respect, this thesis is a prelude of future studies.

Acknowledgements

We thank Dr. Hong Kie Thio for reviewing the manuscript. Lupei Zhu provided us data for the Tibetan profile. This research was supported by the Department of Defense and was monitored by the Air Force, Office of Scientific Research, under the contract #64598. It is also supported by SCEC under contract #64527, as funded by NSF #89-20136 and USGS #1434-93-G-2322. Contribution No. 5812, Division of Geological and Planetary Sciences, California Institute of Technology, Pasadena, California.

Bibliography

Aki, K., and P. G. Richards, *Quantitative seismology, theory and methods*, chap. Chapter 2, W. H. Freeman and Company, 1980.

Ammon, C. J., and J. E. Vidale, Tomography without rays, *Bull. Seism. Soc. Am.*, *83*(2), 509–528, 1993.

Bouchon, M., A simple method to calculate Green's functions for elastic layered media, *Bull. Seism. Soc. Am.*, *71*, 959–971, 1981.

Cohn, S. N., T.-L. Hong, and D. V. Helmberger, The oroville earthquakes: a study of source characteristics and site effects, *Bull. Seism. Soc. Am.*, *87*, 4585–4594, 1982.

Dreger, D., Modeling earthquakes with local and regional broadband data, Ph.D. thesis, California Institute of Technology, Pasadena, California, 1992.

Dreger, D., Empirical Green's function study of the January 17, 1994 Northridge, California earthquake, *Geophys. Res. Lett.*, *21*(24), 2633–2636, 1994.

Dreger, D., and D. V. Helmberger, Source parameters of the Sierra Madre earthquake from regional and local body waves, *Geophys. Res. Lett.*, *18*(11), 2015–2018, 1991a.

Dreger, D., and D. V. Helmberger, Complex faulting deduced from broadband modeling of the 28 February, 1990 Upland earthquake ($m_l = 5.2$), *Bull. Seism. Soc. Am.*, *81*, 1129–1144, 1991b.

Dreger, D., and D. V. Helmberger, Determination of source parameters at regional distances with three-component sparse network data, *J. Geophys. Res.*, *98*, 8107–8125, 1993.

Fuchs, K., and G. Müller, Computation of synthetic seismograms with reflectivity method and comparison with observations, *Geophys. J. R. Astron. Soc.*, *23*, 417–433, 1971.

Hanks, T. C., and H. Kanamori, A moment magnitude scale, *J. Geophys. Res.*, *84*, 2348–2350, 1979.

Hardebeck, J., and E. Hauksson, Patterns of stress drop in the 1994 Northridge aftershock sequence, *Bull. Seism. Soc. Am.*, *in press*, 1997.

Hartzell, S. H., Earthquake aftershocks as Green's functions, *Geophys. Res. Lett.*, *5*, 1–4, 1978.

Hartzell, S. H., and T. H. Heaton, Inversion of strong ground motion and teleseismic waveform data for the fault rupture history of the 1979 Imperial Valley, California, earthquake, *Bull. Seism. Soc. Am.*, *73*(6), 1553–1583, 1983.

Haskell, N. A., Total energy and energy spectral density of elastic wave radiation from propagating faults, *Bull. Seism. Soc. Am.*, *54*(6), 1811–1841, 1964.

Hauksson, E., The 1991 Sierra Madre earthquake sequence in Southern California: seismological and tectonic analysis, *Bull. Seism. Soc. Am.*, *84*(4), 1058–1074, 1994.

Hauksson, E. L., L. M. Jones, and K. Hutton, The 1994 Northridge earthquake sequence in California: seismological and tectonic aspects, *J. Geophys. Res.*, *100*(B7), 12335–12355, 1995.

Helmberger, D., D. Dreger, R. Stead, and H. Kanamori, Impact of broadband seismology on the understanding of strong motions, *Bull. Seism. Soc. Am.*, *83*, 830–850, 1993.

Helmberger, D. V., Theory and application of synthetic seismograms, in *Earthquakes: Observation, Theory and Interpretation*, edited by H. Kanamori, pp. 173–222, Soc. Italiana di Fisica, Bologna, Italy, 1983.

Helmberger, D. V., and B. Woods, Regional source parameters, seismic energy, and discrimination, in *Monitoring a Comprehensive Test Ban Treaty*, edited by E. S. Husebye and A. M. Dainty, pp. 365–383, Kluwer Academic Publishers, Netherlands, 1996.

Helmberger, D. V., R. Stead, P. Ho-Liu, and D. Dreger, Broadband modeling of regional seismograms: Imperial Valley to Pasadena, *Geophys. J. Int.*, *110*, 42–54, 1992.

Helmberger, D. V., L.-S. Zhao, and E. Garnero, Construction of synthetics for 2-d structures; core phases, in *Seismic Modeling of Earth Structure*, edited by A. M. Enzo Boschi, Göran Ekström, pp. 183–222, Istituto Nazionale di Geofisica, Editrice Compositori, 1996.

Ho-Liu, P., and D. V. Helmberger, Modeling regional Love waves: Imperial Valley to Pasadena, *Bull. Seism. Soc. Am.*, *79*(4), 1194–1209, 1989.

Jones, L. E., Broadband modeling of aftershocks from the Joshua Tree, Landers, and Big Bear sequences, Southern California, Ph.D. thesis, California Institute of Technology, Pasadena, California, 1995.

Jones, L. E., and D. V. Helmberger, Seismicity and stress-drop in the eastern transverse ranges, Southern California, *Geophys. Res. Lett.*, *23*(3), 233–236, 1996.

Kanamori, H., H. Thio, D. Dreger, E. Hauksson, and T. Heaton, Initial investigation of the Landers, California, earthquake of 28 June 1992 using TERRAscope, *Geophys. Res. Lett.*, *19*(22), 2267–2270, 1992.

Langston, C. A., The February 9, 1971 San Fernando earthquake: a study of source finiteness in teleseismic body waves, *Bull. Seism. Soc. Am.*, *68*(1), 1–29, 1978.

Langston, C. A., and D. V. Helmberger, Interpretation of body and Rayleigh waves from NTS to Tucson, *Bull. Seism. Soc. Am.*, *64*, 1919–1929, 1974.

Mori, J., and D. V. Helmberger, Large amplitude Moho reflections (SmS) from Landers aftershocks, Southern California, *Bull. Seism. Soc. Am.*, *86*(6), 1845–1852, 1996.

Patton, H. J., and G. Zandt, Seismic moment tensors of western United States earthquakes and implications for the tectonic stress field, *J. Geophys. Res.*, *96*, 18245–18259, 1991.

Priestley, K., and J. Brune, Surface waves and the structure of the Great Basin of Nevada and western Utah, *J. Geophys. Res.*, *83*, 2265–2272, 1978.

Ritsema, J., and T. Lay, Rapid source mechanism determination of large ($m_w >= 5$) earthquakes in the western United States, *Geophys. Res. Lett.*, *20*, 1611–1614, 1993.

Ritsema, J., and T. Lay, Long-period regional wave moment tensor inversion for earthquakes in the western United States, *J. Geophys. Res.*, *100*(B7), 9853–9864, 1995.

Romanowicz, B. A., Moment tensor inversion of long period Rayleigh waves: A new approach, *J. Geophys. Res.*, *87*, 5395–5407, 1982.

Saikia, C. K., Modified frequency-wavenumber algorithm for regional seismograms using filon's quadrature-modeling of lg waves in North America, *Geophys. J. Int.*, *118*, 142–158, 1994a.

Saikia, C. K., Modified frequency-wavenumber algorithm for regional seismograms using filon-quadrature method – modeling of l_g waves in eastern North America, *Geophys. J. Int.*, *118*(1), 142–158, 1994b.

Saikia, C. K., and D. V. Helmberger, Approximation of rupture directivity in regional phases using up-going and down-going wavefields, *Bull. Seism. Soc. Am.*, *87*(4), 1997.

Scrivner, C. W., and D. V. Helmberger, Preliminary work on an early warning and

rapid response program for moderate earthquakes, *Bull. Seism. Soc. Am.*, *85*(4), 1257–1265, 1995.

Sen, M. K., and P. L. Stoffa, Nonlinear one-dimensional seismic waveform inversion using simulated annealing, *Geophysics*, *56*, 1624–1638, 1991.

Song, X. J., and D. V. Helmberger, Source estimation of finite faults from broadband regional networks, *Bull. Seism. Soc. Am.*, *86*(3), 797–804, 1996.

Song, X. J., and D. V. Helmberger, Northridge aftershocks, a source study with TERRAscope data, *Bull. Seism. Soc. Am.*, *in press*, 1997.

Song, X. J., L. E. Jones, and D. V. Helmberger, Source characteristics of the 17 January 1994 Northridge, California, earthquake from regional broadband modeling, *Bull. Seism. Soc. Am.*, *85*(6), 1591–1603, 1995a.

Song, X. J., C. W. Scrivner, and D. V. Helmberger, Source characteristics of Northridge aftershocks, with application to the effect of San Fernando Basin on the propagation of seismic energy, *Eos Trans. AGU*, *76*(46), F356, 1995b.

Song, X. J., L.-S. Zhao, and D. V. Helmberger, Broadband modeling of regional seismograms; the Basin and Range crustal structure, *Geophys. J. Int.*, *125*, 15–29, 1996.

Stead, R., Finite differences and a coupled analytic technique with applications to explosions and earthquakes, Ph.D. thesis, California Institute of Technology, Pasadena, California, 1990.

Thatcher, W., and T. C. Hanks, Source parameters of Southern California earthquakes, *J. Geophys. Res.*, *78*, 8457–8576, 1973.

Thio, H.-K., and H. Kanamori, Moment tensor inversion for local earthquakes using surface waves recorded at TERRAscope, *Bull. Seism. Soc. Am.*, *85*(4), 1021–1038, 1995.

Thio, H.-K., and H. Kanamori, Source complexity of the 1994 Northridge earthquake and its relation to aftershock mechanisms, *Bull. Seism. Soc. Am.*, *86*(1B), S84–S92, 1996.

Wald, D. J., Strong motion and broadband teleseismic analysis of the 1991 Sierra Madre, California, earthquake, *J. Geophys. Res.*, *97*, 11033–11046, 1992.

Wald, D. J., T. H. Heaton, and K. W. Hudnut, The slip history of the 1994 Northridge, California, earthquake determined from strong-motion, gps, and leveling-line data, *Bull. Seism. Soc. Am.*, *86*(1B), S49–S70, 1996.

Walter, W., Source parameters of the June 29, 1992 Little Skull Mountain earthquake from complete regional waveforms at a single station, *Geophys. Res. Lett.*, *20*, 403–406, 1993.

Zhao, D., and H. Kanamori, P-wave image of the crust and uppermost mantle in Southern California, *Geophys. Res. Lett.*, *19*, 2329–2332, 1992.

Zhao, L.-S., and C. Frohlich, Teleseismic body-waveforms and receiver structures beneath seismic stations, *Geophys. J. Int.*, *124*, 525–549, 1996.

Zhao, L.-S., and D. V. Helmberger, Source estimation from broadband regional seismograms, *Bull. Seism. Soc. Am.*, *84*(1), 91–104, 1994.

Zhao, L.-S., and D. V. Helmberger, Regional moments, energy levels, and a new discriminant, *Pure Appl. Geophys.*, *146*, 281–304, 1996.

Zhu, L., and D. V. Helmberger, Advancement in source estimation techniques using broadband regional seismograms, *Bull. Seism. Soc. Am.*, *86*(5), 1634–1641, 1996a.

Zhu, L., and D. V. Helmberger, Intermediate depth earthquakes beneath the India-Tibet collision zone, *Geophys. Res. Lett.*, *23*(5), 435–438, 1996b.

Zhu, L., R. Zeng, F. Wu, T. J. Owens, and G. E. Randall, Preliminary study of crust-upper mantle structure of the Tibet Plateau by using broadband teleseismic body waveforms, *Acta. Seism. Sinica.*, *6*, 305–316, 1993.

Zhu, L., T. J. Owens, and G. E. Randall, Lateral variation in crustal structure of the northern Tibetan plateau inferred from teleseismic receiver functions, *Bull. Seism. Soc. Am.*, *85*(6), 1531–1540, 1995.